# 3.4 Cooperative Phenomena in Complex Macroscopic Systems

# Low-rank approximations for tensor decomposition and their application to critical phenomena

Naoki KAWASHIMA

*Institute for Solid State Physics,*

*University of Tokyo, Kashiwa-no-ha, Kashiwa, Chiba 277-8581*

Many of classes of data are labeled with multiple indicators. In that sense, they can be considered as tensor-type data. Compression of tensor type data has a lot in common with information extraction, classification, and restoration. Therefore, it is a technology with extremely high social needs. In recent years, research on critical phenomena using tensor networks (TN) has been actively conducted in the field of computational statistical mechanics. In handling tensor type-data, the low-rank approximation is a technique of the crutial importance. In this project, we aim at developing a low-rank approximation method that approximates tensor-type data, with an eye toward application to general data processing, and we are applying this to critical phenomena in classical and quantum spin models.

The core ingredient in our method is the tensor ring decomposition using "nuclear norm regularization". This method is being actively discussed among data science researchers, and has been applied to image compression, image classification, etc. [1] Previously, this method is applied to the TN renormalization group (TNRG), and it evaluates critical phenomena more stably with a simpler procedure than conventional methods. In the nuclear norm regularization we introduce the kernel norm, which is the sum of singular values, as a penalty term. A similar method could be constructed by using the sum of squares of singular values or mutual information as a penalty term instead of the nuclear norm. However, the nuclear norm is a sum of first powers, similar to LASSO, which has been frequently used in regression analysis, etc. In LASSO, and in our method as well, the optimal solution is such that some parameters (in our case, singular values) are exactly zero. Therefore, it naturally converges to a low-rank solution in our case. In addition, because the shape of the cost function around the optimal solution is not flat, we can expect the calculation to converge quickly. In this project, we improve upon this method to study two types of systems; critical phenomena in 2D classical statistical mechanics models and one-dimensional quantum spin systems, and critical phenomena in 3D classical statistical mechanics models. In the school year 2023, we obtained the following results:

(A) Benchmark calculations of 2D Ising model by the new method shows a clear advantage over the any previously-known TNRG methods and also over similar methods with milder cost functions based on mutual information. (Reported partially in [2], but shall be fully discussed in its revised version.)

(B) Some pilot calculation was carried out on the 3D Ising model, which produced promising results on the accuracy and the stability in the scaling dimensions. (The result will be fully discussed elsewhere.)

(C) Some other application of TN methods were carried out for dynamical properties of 2D quantum systems and exploring the phase diagram of a system that shows order-by-disorder physics. Since this part have been already published formally, we will discuss these further below.

In [3], we proposed a method for obtaining elementary excitations from unknown ground states. For this purpose, so-called diagrammatic summation is necessary while the code that realizes such computation is usually rather messy demanding a large amount of human labor. To solve this problem, we extended the scheme that we previously proposed for taking the diagrammatic summation using the generating-function. With the ansatz of the form of a one-particle excitation, we show that the excited state can be computed efficiently in this formalism. The dynamical structure factor of the system can be also computed. We carried out benchmark calculation on the spin-1/2 transverse-field Ising model and Heisenberg model on the square lattice, which exhibits good agreement with known results with reasonable accuracy. We then studied the spin-1/2 J1-J2 model on the same lattice and investigated the dynamical properties of the putative gapless spin liquid phase.

In [4], we studied the simplest quantum lattice spin model for the two-dimensional (2D) cubic ferromagnet by means of mean-field analysis and tensor network calculation. While both methods give rise to similar results in detecting related phases, the 2D infinite projected entangled-pair state (iPEPS) calculation provides more accurate values of transition points. Near the phase boundary, moreover, our iPEPS results indicates the easy-axis softening, implying an emergence of continuous U(1) symmetry.

## References

[1] Q. Zhao, et al, arXiv:1606.05535.

[2] Kenji Homm and Naoki Kawashima, arXiv:2306.17479.

[3] Wei-Lin Tu, Laurens Vanderstraeten, Norbert Schuch, Hyun-Yong Lee, Naoki Kawashima, and Ji-Yao Chen, Physical Review X5, 010335 (2024)

[4] Wei-Lin Tu, Xinliang Lyu, S. R. Ghzanfari, Huan-Kuang Wu, Hyun-Yong Lee and Naoki Kawashima, Physical Review B 107, 224406 (1-14) (2023)

# Large-scale Molecular Simulation of Soft Materials using All- Atom and Coarse-Grained Models

Wataru SHINODA

*Research Institute for Interdisciplinary Science, Okayama University*
*3-1-1 Tsushima-naka, Kita-ku, Okayama 700-8530*

We have used molecular simulations to study several biomolecular self-assemblies and soft materials, including highly concentrated Li-salt electrolytes. Significant progress in developing the SPICA force field (FF) has been the improvement of the protein model[1]. Our new protein model (SPICA FF ver2) overcomes the shortcomings found in the previous force field, where intrinsically disordered proteins (IDPs) were simulated as too compact in the dimension in an aqueous solution, and protein binding on the lipid membrane surface was over-stabilized. These issues were commonly found in many FFs, including all-atom FF, so we introduced protein secondary structure-dependent nonbonded interaction parameters to the backbone segments and re-optimize almost all nonbonded parameters for amino acids. The improved FF effectively replicates the radius of gyration observed in multiple IDPs, the binding sensitivity of numerous peripheral membrane proteins, and the dimerization-free energies of various transmembrane helices. Additionally, the updated model demonstrates enhanced consistency with experimental findings regarding the free energy of peptide association in aqueous environments.

Coarse-grained molecular dynamics (CG-MD) simulations using non-polar water models cannot correctly describe electrostatic screening effects owing to the hydration of ionic segments and thus cannot appropriately describe molecular events involving water channels and pores through lipid membranes. To overcome this issue, we developed a protein model in the pSPICA FF, in which a polar CG water model showing the proper dielectric response was adopted.[2] The developed CG model significantly improved the transfer free energy profiles of charged side chain analogues across the lipid membrane. Application studies on melittin-induced membrane pores and mechanosensitive channels in lipid membranes demonstrated that CG-MDs using the pSPICA FF correctly reproduced the structure and stability of the pores and channels. Furthermore, the adsorption behavior of the highly charged nona-arginine peptides on lipid membranes changed with salt concentration, indicating the pSPICA FF is also useful for simulating protein adsorption on membrane surfaces.

The above-mentioned large-scale CG-MDs have been carried out using System B with highly parallelized software such as LAMMPS and GROMACS. We also have done a series of MD simulations at the atomistic level using our polarizable model to investigate the Li-ion dynamics in solvated Li-salts, mostly using System C, which produced several papers this year[3, 4, 5, 6].

# References

[1] T. Yamada, et al., J. Chem. Theory Comput. **19**, 8967 (2023).

[2] Y. Miyazaki and W. Shinoda, J. Chem. Inf. Model. **64**, 532 (2024).

[3] S. Ikeda, et al., J. Phys. Chem. C, **127**, 13837 (2023).

[4] S. Tsuzuki, et al., J. Phys. Chem. B, **127**, 6333 (2023).

[5] K. Shigenobu, et al., J. Phys. Chem. B, **127**, 10422 (2023).

[6] T. Sudo, et al., J. Phys. Chem. C, **127**, 12295 (2023).

# Molecular Dynamics Analysis on Ultrasonic Cavitation

Yuta ASANO

*Institute for Materials Research,*

*Tohoku University, Katahira, Aoba-ku, Sendai, Miyagi 980-8577*

When a liquid is subjected to powerful ultrasonic waves, numerous bubbles are repeatedly generated and collapsed. This phenomenon is called ultrasonic cavitation. A high-temperature and high-pressure field is generated locally associated with the bubble collapse. Since ultrasonic cavitation is a highly safe and environmentally friendly technology, its application exists in broad fields, including food, medicine, biotechnology, and chemistry. Therefore, it is crucial to unveil the underlying mechanisms of ultrasonic cavitation. However, ultrasonic cavitation is a highly intricate phenomenon that causes many bubbles to continuously form, grow, and collapse under highly nonequilibrium conditions, and its mechanism is not fully comprehended.

In FY2023, we focused on elucidating soundwave propagation in a bubbling liquid, because its characteristics constitute an essential part of ultrasonic cavitation. The large-scale molecular dynamics (MD) simulation is applied to the analysis of soundwave propagation [1]. The MD simulation is promising for directly analyzing the effects of the interaction between bubbles, thermal and mass transport through the gas-liquid interface and phase transition.

The fluid is modeled by the Lennard-Jones (LJ) system. The system is a rectangular parallelepiped with the dimension of $L_x \times L_y \times L_z = 5000 \times 250 \times 250$. The periodic boundary conditions are applied to $y$- and $z$-directions. Since the soundwave propagates $x$-direction, the oscillating and stationary walls are placed at both boundaries. The liquid density is 0.6 with the total number of particles is about 200 million in total. MD simulations are performed by LAMMPS (Large-scale Atomic/Molecular Massively Parallel Simulator).

The bubbly liquid is generated using the depressurized method [2]. A non-condensable gas is added to the liquid to control the bubble distribution. Since the non-condensable gas affects the cavitation process and suppresses the Ostwald ripening [3], its addition can control the bubble distribution. The liquid with non-condensable gas is modeled by the binary LJ fluid. The maximum volume fraction of the non-condensable gas is up to 10%.

Figure 1 shows the bubbly liquid obtained by the depressurization. Only low-density areas are depicted for visibility. Although the liquid

has no bubbles at the boiling point (Fig. 1(a)), After the depressurization, the bubbles appear in the liquid. When the small depressurization, large bubbles distribute sparsely (Fig. 1(b)). As for the large depressurization, various sizes of bubbles distribute densely (Fig. 1 (c)). The bubbly liquid with non-condensable gas is also generated (Fig. 2). The bubbles become finer with the concentration of non-condensable gas.

When sound waves are propagated in a bubbly liquid, scattering, and absorption by the bubbles impede the propagation of the sound waves. In the pure liquid, the large bubble strongly attenuates the soundwave. The attenuation increases with the number of bubbles. As for the liquid with non-condensable gas, since the bubble distribution gradually changes with the concentration of the non-condensable gas, the attenuation is gradually varied. Fig. 3 shows the waveform of liquid with non-condensable gas with and without bubbles. Note that the wavelength also decreases due to the bubble. Although the addition of impurity increases the attenuation due to the viscosity increase, we found that increasing the concentration causes a larger propagation length. Therefore, the bubble distribution, especially its average radius, plays the dominant role in the soundwave propagation. More detailed analyses can reveal the mechanism of a drastic decrease in sound speed and the origin of dispersion in bubbly liquids.
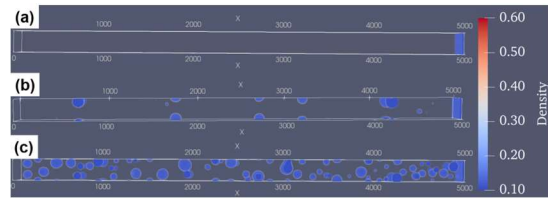


Fig. 1: (a) Pure liquid at boiling point, and (b, c) bubbly liquid.
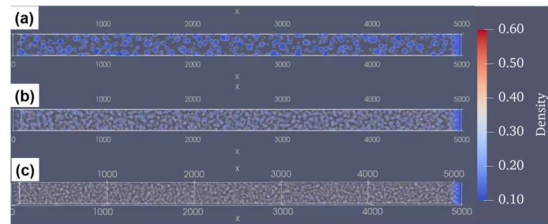


Fig. 2: Bubbly liquid with non-condensable gas with the concentration of (a) 1%, (b) 5%, and (c) 10%.
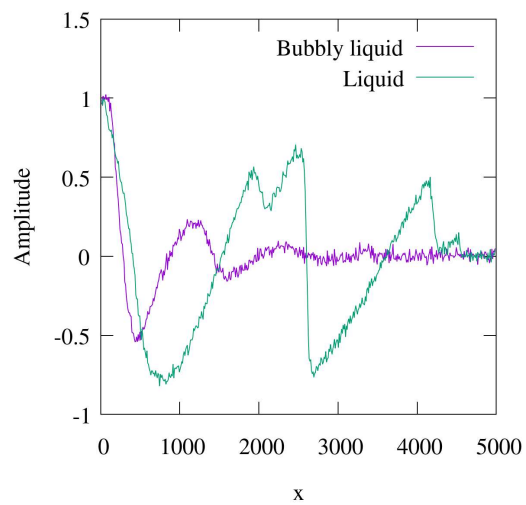


Fig. 3: The waveform of liquid and bubbly liquid with the non-condensable gas of 5%.

## References

[1] Y. Asano, H. Watanabe, and H. Noguchi, Phys. Rev. Fluids **7**, 064302 (2022).

[2] H. Watanabe, M. Suzuki, H. Inaoka, N. Ito, J. Chem. Phys. **141**, 234703 (2014).

[3] S. Tsuda, S. Takagi, Y. Matsumoto, Fluid Dyn. Res. **40**, 606 (2008)

# Energy spectrum analysis on a red blood cell model

Tetsuya YAMAMOTO and Hiroshi WATANABE

*Faculty of Science and Technology, Keio University*

*Yokohama, Kanagawa 223-8522, Japan*

We investigated the fluctuation behavior of the red blood cells (RBCs). RBCs are the main blood component, transporting oxygen and carbon dioxide. RBCs can deform so they can pass through capillaries with diameters less than half their radius, and elucidating their physical properties is essential for health. While RBCs have been studied theoretically and experimentally, recent developments in computational power allow us to perform direct blood flow simulations. With computer simulations, we can directly verify the behavior of fluids containing many plastic deformable objects, which is challenging to handle theoretically and elucidate microscopic properties that are difficult to observe experimentally. Modeling red blood cells is necessary to perform numerical simulations of them. Several types of red blood cell modeling exist, one of which is the particle-based method proposed by Fedosov et al. [1]. This model includes two-, three-, and four-body forces. The model parameters were determined to reproduce the mechanical properties determined by the experiment. Still, due to limitations in the accuracy of the experiments, the estimates of these parameters were ambiguous. To address this problem, we proposed a new method of determining the model parameters precisely from the fluctuations of the RBC membrane [2].

We adopted the dissipative particle dynamics (DPD) to achieve the isothermal environment. After thermalization with the DPD thermostat, we turned off the thermostat and continued the simulation under the isoenergetic environment. We observed the time evolutions of the potential energies and obtained their spectra with the temporal Fourier transform. Reflecting the microscopic nature of the model, multiple peaks appeared in the spectra. We performed the same simulation, with the model parameters changed from their original values, and observed the spectra to determine where each peak originated. If the peaks shifted, we can determine that they originated from the changed model parameters. We then found that some peaks originated from the two-body interaction, and others originated from the volume conservation laws. As an experimentally observable quantity, we also investigated the spectrum of the gyration radius of the RBC. The results show that a characteristic peak also appears in the spectra and that the peak position is sensitive to parameter changes. Compared to previous methods for studying the response of red blood cells to a static external field, our method using spectra is expected to allow more precise determination of model parameters because of the sharp parameter dependence of the peak positions of the spectra.

## References

[1] A. Fedosov, B. Caswell, and G. E. Karniadakis, Comput. Methods Appl. Mech. Eng. **199**, 1937–1948 (2010).

[2] T. Yamamoto and H. Watanabe, J. Chem. Phys. **159**, 234119 (2023).

# Tensor Netowkr Study on $S = 1$ Bilinear-Biquadratic Kitaev model

Tsuyoshi OKUBO

*Institute for Physics of Intelligence, University of Tokyo*
*7-3-1 Hongo, Bunkyo-ku, Tokyo 133-0033*

The $S = 1/2$ honeycomb lattice Kitaev model has been extensively studied as a model for investigating the properties of two-dimensional spin liquids [1, 2]. Similarly, Kitaev models with higher $S$ are also believed to have spin liquid ground states. However, unlike the $S = 1/2$ case, Kitaev models with higher $S$ are not exactly solvable, making numerical analysis crucial. In spin systems with higher $S$, in addition to conventional magnetic order, the nematic order, which is absent in $S = 1/2$ spin systems, can also be stabilized. Recently, the competition between Kitaev and other interactions have been analyzed using semiclassical approximations [3]. However, due to the limitations of these approximations, Kitaev spin liquid could not be precisely treated, and the phase structure near the spin liquid has not been sufficiently analyzed.

To elucidate the competition between the $S = 1$ Kitaev spin liquid and nematic order, we analyzed bilinear-biquadratic (BBQ) Kitaev model [3] this year. The Hamiltonian of the BBQ-Kitaev model is given as

$$\hat{H}_{\text{BBQ-K}} = \sum_{\gamma=x,y,z} \sum_{\langle i,j \rangle_\gamma} \hat{H}_{\langle i,j \rangle_\gamma}, \qquad (1)$$

$$\hat{H}_{\langle i,j \rangle_\gamma} = J_1 \hat{\boldsymbol{S}}_i \cdot \hat{\boldsymbol{S}}_j + J_2 \left( \hat{\boldsymbol{S}}_i \cdot \hat{\boldsymbol{S}}_j \right)^2 \qquad (2)$$
$$+ K \hat{S}_i^\gamma \hat{S}_j^\gamma.$$

Here, $\langle i,j \rangle_\gamma$ denotes the nearest neighbor pair on a $\gamma$ bond. $J_1$, $J_2$, and $K$ are the coupling coefficients for the Heisenberg, biquadratic, and Kitaev interactions, respectively. To analyze the phase structure of the BBQ-Kitaev model,
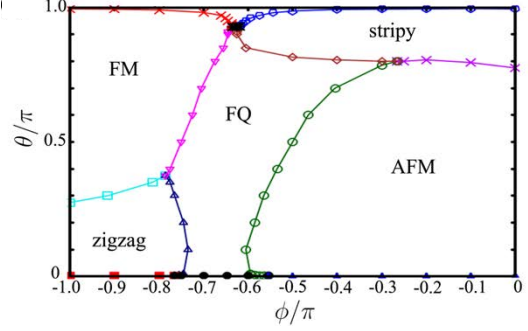


Figure 1: Phase diagram of the BBQ-K model in the region of $0.0 \leq \theta/\pi \leq 1.0$ and $-1.0 \leq \phi/\pi \leq 0.0$. FQ stands for the ferro-quadrupolar phase, and in the vicinity of $\phi/\pi = 0$ and 1, we observed an extended spin liquid phase. (Adapted from Ref. [5])

we employed the infinite projected entangled pair state (iPEPS) method, which can directly calculate the ground state of an infinitely large system. To optimize the tensors in iPEPS, we used imaginary time evolution combined with the truncation of the bond dimension by the simple update. The calculation of the physical quantities was performed by the corner transfer matrix renormalization group method. The entire calculation was done using TeNeS [4], which supports MPI and OpenMP hybrid parallelization.

In Fig. 1, we show the phase diagram of the BBQ-Kitaev model for $J_2 < 0$ [5]. We represented the interaction coefficients with two parameters $\theta$ and $\phi$ as $(J_1, J_2, K) \equiv (\sin\theta\cos\phi, \sin\theta\sin\phi, \cos\theta)$. We found that

the BBQ-Kitaev model has a rich phase structure, including both ferro and anti-ferro Kitaev spin liquids, the quadrupolar order, and several magnetic orders. Interestingly, there is a direct phase transition between the ferro-quadrupolar (FQ) ordered and the Kitaev spin liquid phases. Note that both phases are characterized by the absence of magnetic order. In this sense, we can consider that such direct transition is induced by quantum fluctuations, and there is no classical counterpart.

In addition to this point, in the case of ferro Kitaev spin liquid, we observed an extension of the spin liquid phase around $\phi = \arctan(2) \simeq -0.648\pi$, where the BBQ interaction is reduced into the pure quadrupolar interaction, without Heisenberg interaction. This result indicates that the ferro Kitaev spin liquid is robust against the quadrupolar interaction. This would be useful not only for the search for Kitaev spin liquids in real compounds but also for understanding the nature of general spin liquids.

# References

[1] A. Kitaev, Ann. Phys. **321** (2006) 2.

[2] Y. Motome and J .Nasu, J. Phys. Soc. Jpn. **89** (2020) 012002.

[3] R. Pohle, N. Shannon, and Y Motome, Phys. Rev. B **107** (2023) L140403 .

[4] Y. Motoyama, T. Okubo, K. Yoshimi, S. Morita, T. Kato and N. Kawashima, Comput. Phys. Commun. **279**, (2022) 108437.

[5] T. Mashiko and T. Okubo, arXiv:2403.11490.

# Numerical simulations of fluctuating hydrodynamics: renormalized correction of shear viscosity

Hiroyoshi NAKANO

*Institute for Solid State Physics, University of Tokyo*
*Kashiwa-no-ha, Kashiwa, Chiba 277-8581*

In the intermediate regime between microscopic and macroscopic scales, conventional deterministic hydrodynamics often fails to accurately capture certain phenomena since the influence of thermal noises becomes profoundly significant, as represented by the Brownian motion. Fluctuating hydrodynamics is an extension of conventional fluid mechanics to describe this intermediate regime. The fundamental equation of motion of $d$-dimensional fluids was proposed in 1959 as follows [1]:

$$\frac{\partial \rho}{\partial t} = -\nabla \cdot (\rho \boldsymbol{v}) \tag{1}$$

$$\rho \left[ \frac{\partial \boldsymbol{v}}{\partial t} + (\boldsymbol{v} \cdot \nabla)\boldsymbol{v} \right] = -\nabla p + \eta_0 \nabla^2 \boldsymbol{v}$$
$$+ \left[ \zeta_0 + \left( 1 - \frac{2}{d} \right) \eta_0 \right] \nabla(\nabla \cdot \boldsymbol{v}) - \nabla \cdot \boldsymbol{\Pi}^{\mathrm{ran}} \tag{2}$$

with

$$\langle \Pi_{ij}^{\mathrm{ran}}(\boldsymbol{r}, t) \Pi_{mn}^{\mathrm{ran}}(\boldsymbol{r}', t') \rangle =$$
$$2 k_B T \delta^d(\boldsymbol{r} - \boldsymbol{r}') \delta(t - t')$$
$$\left[ \eta_0 \left( \delta_{im}\delta_{jn} + \delta_{in}\delta_{jm} \right) + \left( \zeta_0 - \frac{2}{d}\eta_0 \right) \delta_{ij}\delta_{mn} \right] \tag{3}$$

where $\rho(\boldsymbol{r}, t)$ is density field, $\boldsymbol{v}(\boldsymbol{r}, t)$ is velocity field, $p(\boldsymbol{r}, t)$ is pressure field, and $\Pi_{ij}^{\mathrm{ran}}(\boldsymbol{r}, t)$ is random stress tensor field. $\eta_0$ and $\zeta_0$ are shear and bulk viscosity, respectively. This formulation is reasonable within the principles of nonequilibrium statistical mechanics, as pioneered by Onsager. Indeed, it has been applied to various fields. A prominent example is the transport phenomena in low-dimensional fluids, where fluctuating hydrodynamics leads to the renormalized correction of observed transport coefficients due to the nonlinear coupling of fluctuations [2]. However, so far, such nonlinear phenomena have been examined primarily through theoretical approaches such as renormalization group theory and mode-coupling theory. No studies have yet attempted to directly simulate fluctuating hydrodynamics Eqs. (1), (2), and (3). Therefore, the validity -particularly the quantitative validity- of these theoretical results remains unclear.

In this study, we performed the numerical simulation of Eqs. (1), (2), and (3) in two dimensions [3] under the nearly incompressible condition and examined the divergence of the observed viscosity.

We focus on the Couette flow setup (the left panel of Fig. 1), where the fluid is confined between two parallel walls moving in opposite directions at speeds of $\pm v_0/2$. Then, we observe the noise-averaged velocity profile $\langle v^x(\boldsymbol{x}) \rangle$ and shear stress profile $\langle \sigma^{xy}(\boldsymbol{x}) \rangle$ to study the observed viscosity $\eta$ defined by

$$\langle \sigma^{xy}(\boldsymbol{x}) \rangle = \eta \frac{\partial \langle v^x(\boldsymbol{x}) \rangle}{\partial y} \tag{4}$$

This observed viscosity $\eta$ differs from the theoretical viscosity $\eta_0$. In the right panel of Fig. 1, we present the variation of $\eta - \eta_0$ with respect to $\eta_0$, showing that $\eta - \eta_0$ is small for large $\eta_0$ and converges to the finite value as $\eta_0$ approaches 0. We further compare our simulation
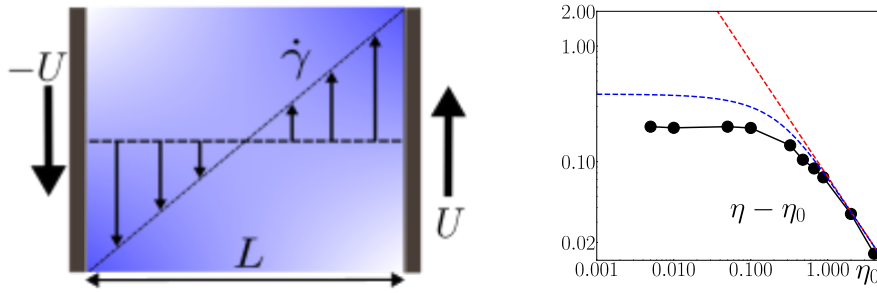
Figure 1: (Left) Couette flow setup. (Right) Variation of $\eta - \eta_0$ with respect to $\eta_0$. The black, red, and blue curves, respectively, represent the results of our simulation, the simple perturbation theory, and the theory of Forster, Nelson, and Stephen [2].

results against two previous theoretical results developed for Eqs. (1), (2), and (3), which are depicted as red and blue lines in the right panel of Fig. 1. We can see that for sufficiently large $\eta_0$, our simulation results are in good agreement with both the simple perturbation theory and Forster's theory [2]. However, as $\eta_0$ decreases, both theories deviate from the simulation results.

The previous theories rely on perturbation methods and have limitations in the treatment of nonlinear effects. Thus, our simulation results suggest that a more precise theory is necessary for small $\eta_0$ to enable quantitative analysis.

# References

[1] D. Landau and E. M. Lifshitz, Fluid Mechanics (Pergamon Press, Oxford, 1959).

[2] D. Forster, D. R. Nelson, and M. J. Stephen, Phys. Rev. A **16** 732 (1977)

[3] I. Srivastava *et al.* Phys. Rev. E **107**, 015305 (2023)

# Basic and applied studies on protein structure and function

Koji OOKA[1], Masataka YOSHIMURA[2], Nao SATO[2], Runjing LIU[2], Kaho KOTANI[2], Shinya INOUE[2], Sae KATO[2], Shun NAGAI[3], Shunji SUETAKA[2], and Munehito ARAI[1,2,3]

[1]College of Arts and Sciences, [2]Department of Life Sciences, Graduate School of Arts and Sciences, and [3]Department of Physics, Graduate School of Science, The University of Tokyo, Komaba, Meguro, Tokyo 153-8902

Proteins have recently been used in industry and medicine. These proteins perform biological functions such as binding and catalysis through dynamic motions after folding into specific globular structures. Therefore, it is important to elucidate the mechanisms of protein folding to facilitate their application. In addition, the theoretical design of proteins has recently received considerable attention. Thus, we have studied the folding mechanisms of proteins, the functional motions of proteins, and the theoretical design of novel useful proteins.

To theoretically predict protein folding mechanisms, we have developed a statistical mechanics theory that can accurately predict the free energy landscape of proteins, called the WSME-L model [1]. This theory represents a significant advance in the field because it can be applied to any protein, regardless of the presence or absence of disulfide bonds or the shape of the protein. The program is written in C++ and Python. In addition, we have used this theory to design mutants with altered protein folding pathways. Since the WSME-L model requires the three-dimensional structure of a protein to predict its free energy landscape, we predicted the structures of various mutants using localcolabfold, which can perform protein structure prediction using AlphaFold 2 in a local environment [2]. We are also trying to extend the WSME-L model to predict free energy landscapes for protein-protein interactions, protein-small molecule interactions, and enzymatic reactions.

Protein-ligand interactions are essential for the function of many proteins. To study the interaction between a cyanobacterial photoreceptor protein AnPixJg2_BV4 and biliverdin, we performed molecular dynamics simulations of the protein-ligand complex. The model structure was built using AmberTools22 with the ff14SB force field [3]. Simulations were performed using GROMACS 2022.4 [4] for 2 μs in triplicate (total of 6 μs). We found that amino acid substitutions in the protein altered its interaction with biliverdin, which in turn affected the stability of the complex [5].

Enzymes are widely used in the industrial production of useful substances. Therefore, it is necessary to develop efficient methods to

improve enzymes. Using the physics-based protein design software Rosetta (versions 3.8 and 3.13) [6], we are developing a universal method that can generally improve the activity of various enzymes. Our strategy is to reduce the height of the free energy barrier for the rate-limiting step in the enzyme reaction cycle. We have applied this method to enzymes such as dihydrofolate reductase (DHFR) and aldehyde deformylating oxygenase (ADO). Experimental verification showed that we succeeded in improving the turnover rate of DHFR by ~5-fold by a single amino acid substitution. Activity measurements of ADO mutants are in progress.

Protein-protein interactions have attracted attention as drug targets. However, the interaction surface is generally broad and shallow, making it difficult to inhibit with small molecules, and the development of inhibitors using peptides with a broad interaction surface is promising. We have previously designed two types of peptide inhibitors that bind to each of the two transcription factor binding sites on KIX, targeting the interaction between the KIX domain of CBP and transcription factors involved in various diseases such as leukemia [7,8]. By linking these two peptide inhibitors, we designed a bivalent chimeric peptide inhibitor that simultaneously inhibits both binding sites. We modeled the linker structure using Rosetta and then designed a linker

sequence that could improve the binding ability to the target using ProteinMPNN [9], a deep learning-based amino acid sequence design software. The structures of designed proteins were predicted using localcolabfold. Experiments showed that the designed chimeric peptide binds KIX with more than 2,000-fold higher affinity compared to the isolated peptide inhibitors. Thus, our methods may be useful in the design of inhibitors of protein-protein interactions.

# References

[1] K, Ooka, and M. Arai: Nat. Commun. **14**, 6338 (2023).

[2] M. Mirdita, K. Schütze, Y. Moriwaki, L. Heo, S. Ovchinnikov, and M. Steinegger: Nat. Methods, **19**, 679-682 (2022).

[3] D. A. Case, et al.: AMBER 2022. University of California, San Francisco (2022)

[4] S. Pall, C. J. Smith, B. Hess, E. Lindah: SoftwareX, **1–2**, 19-25 (2015).

[5] T. Suzuki, M. Yoshimura, M. Arai, and R. Narikawa: J. Mol. Biol. **436**, 168451 (2024).

[6] J. K. Leman, et al.: Nat. Methods, **17**, 665 (2020).

[7] S. Suetaka, Y. Oka, T. Kunihara, Y. Hayashi, and M. Arai: Sci. Rep. **12**, 816 (2022).

[8] N. Sato, S Suetaka, Y Hayashi, and M Arai: Sci. Rep. **13**, 6330 (2023).

[9] J. Dauparas, et al.: Science, **378**, 49-56 (2022).

# Spin Nematic Phase of 2D Ferromagnetic Dimer Systems

Tôru SAKAI[1,2], Hiroki NAKANO[1], Masaru Hashimoto[1], Tomoki Houda[1]Rito FURUCHI[1], and Tokuro SHIMOKAWA[3]

[1]*Graduate School of Science, University of Hyogo, Kouto, Kamigori, Hyogo 678-1297, Japan*
[2]*National Institute for Quantum Science and Technology, SPring-8, Kouto, Sayo, Hyogo 679-5148, Japan*
[3]*Theory of Quantum Matter Unit, Okinawa Institute of Science and Technology Graduate University, Onna-son, Okinawa 904-0495, Japan*

## 1 Field-Induced Spin Nematic Phase of Quantum Spin Systems

The spin nematic phase is one of interesting topics in the field of the condensed matter physics. Using the numerical exact diagonalization analysis the field induced spin nematic phase is investigated in several low-dimensional quantum spin systems.

### 1.1 $S = 1/2$ Delta Spin Chain

The magnetization process of the S = 1/2 delta chain with the anisotropic ferromagnetic interaction is investigated using the numerical diagonalization of finite-size clusters[?]. It is found that the spin nematic liquid phase appears in higher magnetization region, as well as the SDW liquid one in lower region.

### 1.2 $S = 1/2$ Bond-Alternating Chains

The S = 1/2 ferromagnetic-antiferromagnetic bond-alternating spin chain with the anisotropy on the ferromagnetic exchange interaction in magnetic field is investigated using the numerical diagonalization and the density matrix renormalization group analyses[?]. It is found that the nematic-spin-dominant Tomonaga-Luttinger liquid phase is induced by the external magnetic field for sufficiently large anisotropy. The phase diagram with respect to the anisotropy and the magnetization is presented.

### 1.3 $S = 1/2$ Distorted Diamond Chain

The magnetization process of the S = 1/2 distorted diamond quantum spin chain with the Ising-like anisotropic ferromagnetic interaction is investigated using the numerical diagonalization method[?]. Two kinds of wide magnetization plateaux are found at 1/3 of the saturation magnetization based on the Haldane-like mechanism and the N´ eel-like mechanism, respectively. Apart from the magnetization plateaux, there appear the conventional Tomonaga-Luttinger liquid (TLL) phase and the two-magnon TLL phase. The latter phase is composed of the nematic TLL phase and the SDW TLL phase. The phase diagram with respect to the ferromagnetic interaction anisotropy parameter versus the magnetization is presented.

## 1.4 2D Ferromagnetic Dimer System

The $S = 1/2$ two-dimensional Shastry-Sutherland system with the ferromagnetic dimers is investigated using the numerical diagonalization[?]. It is found that the field induced spin nematic phase would appear, as well as the magnetization jump due to the spin flop transition.

## References

[1] T. Sakai, R. Furuchi, H. Nakano and K. Okamoto, SciPost Physics Proceedings **11**, 011 (2023)

[2] R. Nakanishi, T. Yamada, R. Furuchi, H. Nakano, H. Kaneyasu, K. Okamoto, T. Tonegawa and T. Sakai, JPS Conf. Proc. **38**, 011156 (2023).

[3] M. Hashimoto, T. Houda, R. Furuchi, H. Nakano, K. Okamoto and T. Sakai, New Physics: Sae Mulli. **73**, 1127 (2023)

[4] T. Sakai, in preparation.

# Novel Magnetization PLateau of the Spin Ladder System

Tôru SAKAI[1,2], Hiroki NAKANO[1], Masaru Hashimoto[1], Tomoki Houda[1] Rito FURUCHI[1], and Tokuro SHIMOKAWA[3]

[1] *Graduate School of Science, University of Hyogo,*
*Kouto, Kamigori, Hyogo 678-1297, Japan*
[2] *National Institute for Quantum Science and Technology,*
*SPring-8, Kouto, Sayo, Hyogo 679-5148, Japan*
[3] *Theory of Quantum Matter Unit,*
*Okinawa Institute of Science and Technology Graduate University,*
*Onna-son, Okinawa 904-0495, Japan*

## 1 Translational Symmetry Broken Magnetization Plateau of the One-Dimensional Quantum Spin Systems

We investigate the $S = 1$ antiferromagnetic quantum spin chain with the exchange and single-ion anisotropies in a magnetic field, using the numerical exact diagonalization of finite-size clusters, the level spectroscopy analysis, and the density matrix renormalization group (DMRG) methods[1]. It is found that a translational symmetry broken magnetization plateau possibly appears at the half of the saturation magnetization, when the anisotropies compete with each other. The level spectroscopy analysis gives the phase diagram at half the saturation magnetization. The DMRG calculation presents the magnetization curves for some typical parameters and clarifies the spin structure in the plateau phase.

## 2 Novel Magnetization Plateau of the $S=2$ Antiferromagnetic Chain with Anisotropies

The magnetization plateau of the S = 2 antiferromagnetic chain with interaction and single ion anisotropies is investigated using the numerical diagonalization of finite-size clusters and some size scaling analyses[2]. The previous level spectroscopy analysis indicated that two different magnetization plateau phases appear at half of the saturation magnetization. One is due to the large-D mechanism and the other is due to the Haldane one. In the present study the phase diagram is extended to wider region of the anisotropies. As a result we find another half magnetization plateau phase, where the translational symmetry is spontaneously broken.

## 3 Magntization Plateau due to Competing Anisotropies

The magnetization process of the $S = 1/2$ ferromagnetic and antiferromagnetic bond-alternating chain with competing anisotropies

is investigated using the numerical diagonalization of finite-size systems[3]. It is found that when the easy-plane and easy-axis anisotropies are introduced at the ferromagnetic and antiferromagnetic bonds, respectively, the system possibly exhibits the 1/2 magnetization plateau with the spontaneous translational symmetry breaking. The phase diagrams with respect to the two anisotropies are presented.

The magnetization plateau based on the same mechanism is revealed to occur in the $S = 1/2$ spin ladder system with the ferromagnetic rung interaction in the presence of the competing anisotropies[4].

# References

[1] T. Sakai, K. Okamoto, K. Okunishi, M. Hashimoto, T. Houda, R. Furuchi and H. Nakano, Phys. Rev. B **108**, 174435 (2023).

[2] T. Yamada, R. Nakanishi, R. Furuchi, H. Nakano, H. Kaneyasu, K. Okamoto, T. Tonegawa and T. Sakai, JPS Conf. Proc. **38**, 011163 (2023).

[3] T. Sakai, M. Hashimoto, T. Houda, R. Furuchi, H. Nakano, K. Okamoto and K. Okunishi, New Physics: Sae Mulli. **73**, 1131 (2023).

[4] T. Sakai, M. Hashimoto, T. Houda, R. Furuchi, H. Nakano, K. Okamoto and K. Okunichi, in preparation.

# Rotational diffusion of water molecules on phospholipid bilayers

Yuji HIGUCHI

*Research Institute for Information Technology, Kyushu University*
*Motooka Nishi-ku, Fukuoka 819-0395*

By molecular simulations, we have revealed the dynamics of water on semicrystalline polymers [1] and on phospholipid bilayers [2], changes in ion distribution on phospholipid bilayers [3], and transport dynamics of phase-separated domains on phospholipid bilayers induced by electric fields [4]. This year, we studied the water dynamics around osmolytes by density-functional tight-binding molecular dynamics (DFTB-MD) simulations using DFTB+ [5] on systems B and C.

The experiments suggested that the dynamics of water around osmolytes influence protein stability. However, the relationship between osmolytes and water dynamics remains unclear at the molecular level. We perform DFTB-MD simulations to reveal the different rotational dynamics of water molecules around 15 osmolytes. In Fig. 1, a positive correlation is found between the rotational relaxation time $\langle \tau \rangle$ and our proposed normalized parameter $N_{\mathrm{HB}}/N_{\mathrm{NN}}$, which is obtained by dividing the number of hydrogen bonds between water molecules by the number of nearest neighbor water molecules. The rotational dynamics of water molecules slow down when the value of the normalization parameter in the second layer from the osmolyte increases, indicating that the second hydration shell is important for the rotational dynamics of water molecules. We expect that our simulation results contribute to understanding the water dynamics around organic molecules and the long-range structure of water molecules.
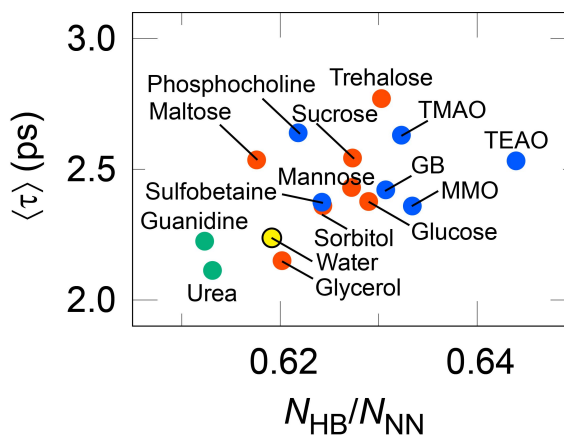


Figure 1: The average rotational relaxation time of water for 15 osmolyte solutions versus the normalized parameter.

# References

[1] T. Kokuzawa, S. Hirabayashi, Y. Ikemoto, J. Park, R. Ikura, Y. Takashima, Y. Higuchi, and G. Matsuba: Polymer **298**, 126922 (2024).

[2] M. K. Rahman, T. Yamada, N. L. Yamada, M. Hishida, Y. Higuchi, and H. Seto: Struct. Dyn. **10**, 044701 (2023).

[3] Y. Higuchi, K. Bohinc, J. Rečščič, N. Shimokawa, and H. Ito: Soft Matter **19**, 3640 (2023).

[4] H. Ito, N. Shimokawa, and Y. Higuchi: J. Phys. Chem. B **127**, 8860 (2023).

[5] B. Hourahine, et al.: J. Chem. Phys. **152**, 124101 (2020).

# Molecular dynamics simulations for engineering tensile properties of carbon nanotube yarns

Go Yamamoto and Redha A. Ramadhan

*Department of Aerospace Engineering, Tohoku University,*
*6-6-01 Aramaki-Aza-Aoba, Aoba-ku, Sendai 980-8579, Japan*

Carbon nanotubes (CNTs) are an innovative material with significant potential for a wide range of applications, including, but not limited to, the development of lightweight composite materials or superconductors. An individual CNT demonstrates an exceptional degree of tensile strength [1]. CNTs are commonly employed in yarn structures, where several CNT strands are arranged and aligned together. CNT yarns, on the other hand, have a lower tensile strength than individual CNTs due to the different parameters of the yarn [2]. This study aimed to investigate the effect of different structural parameters on the mechanical properties of CNT yarns.

The simulation was performed using LAMMPS. Results from tensile loading simulations with structure modifications were gathered from sixty MD simulations and used as the data for the parametric study. The models were generated using High-throughput MD (HTMD), a Python-based tool [3], which allowed for the control of CNT variables. Fig. 1 shows the blue outer regions on both ends of every MWCNT in the yarn, assigned as the fixed parts where the tensile load was applied, while the red part was assigned as the mobile parts where the atoms were unconstrained and used for stress calculation. The number of CNTs in the yarn varied between 1, 3, and 7, while the number of walls ranged from 2 to 5. Both armchair and zigzag types of CNT chirality were simulated. The twist angle was also investigated by varying the yarn twist

between $0° - 30°$ with 5° steps. Sixty CNT yarn models with different structures were simulated with the MD simulation. It was found that the parameters for the CNT yarn that yield a higher tensile strength are the armchair-type CNT with a small diameter, a large number of walls, crosslink density higher than approximately 1%, and a low twist angle.
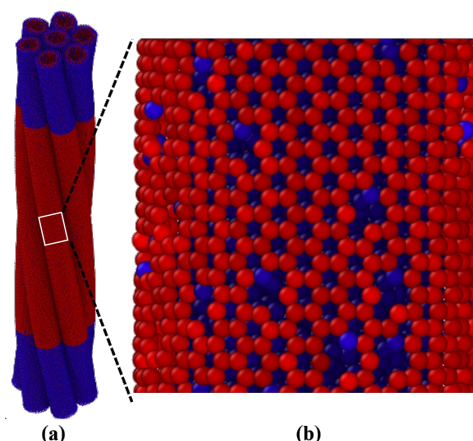


Fig. 1: View of a full 7-MWCNT yarn model with 10° twist angle, showing the blue fixed parts on both ends of the MWCNTs, and the red mobile parts on the middle of the MWCNTs.

## References

[1] B. Peng, M. Locascio, P. Zapol, S. Li, S.K. Mielke, G.C. Schatz, and H.D. Espinosa, H. D. Nat. Nanotechnol. **3**, 626 (2008).

[2] K. Koziol, J. Vilatela, A. Moisala, M. Motta, P. Cunniff, M. Sennett, and A. Windle, Science **318**, 1892 (2007).

[3] Y. Xiang, K. Shimoyama, K. Shirasu, and G. Yamamoto, Nanomaterials **10**, 2459 (2020).

# Quantum-classical hybrid simulations for sensor materials based on quantum state tomography

Wataru Mizukami

*Center for Quantum Information and Quantum Biology, Osaka University, Osaka 560-0043, Japan*

Quantum computers have made significant advancements in recent years, and the field of computational materials science is considered to be its promising application area. Nevertheless, a quantum computer alone is not capable of easily performing meaningful calculations. Quantum-classical hybrid algorithms, where quantum computers handle limited tasks and classical computers handle the rest, are crucial for applying quantum computers to real-world problems. Our research focuses on developing and applying such hybrid algorithms to simulate actual materials, particularly sensor materials.

This year, we applied a methodology based on quantum state tomography to calculate the properties of molecules and materials. The Variational Quantum Eigensolver (VQE), a representative quantum-classical hybrid algorithm for fermionic systems, has been extensively researched but faces issues such as low noise tolerance and high sampling costs. To address these issues, we developed several methods that reconstruct the quantum state on a classical computer through tomography. These methods allow us to combine accurate classical

algorithms like Coupled Cluster (CC) and Auxiliary Field Quantum Monte Carlo (AFQMC) with quantum computing. We validated the AFQMC with our tomography method on chemical reaction systems, achieving chemical accuracy within 1 kcal/mol compared to the state-of-the-art classical algorithm CBS-QB3. We also developed QC-CBT-TCC, which connects with CC, and verified its effectiveness.

Furthermore, we developed a method for applying quantum machine learning (QML) to cheminformatics. At this moment, owing to constraints on available qubits, compact descriptors are highly desirable for QML. We exploited universal neural network potentials (NNPs) to generate such descriptors. Using intermediate information from well-trained NNPs as descriptors enables the creation of compact yet highly accurate descriptors, comparable to the state-of-the-art FCHL descriptor in predicting NMR chemical shifts. We also created QML models using these descriptors, paving the way for constructing practical QML models for molecules/materials.

# Study on Johari-Goldstein relaxation mode in glass-forming liquids

Takeaki ARAKI[a] and Makina SAITO[b]

*aDepartment of Physics, Kyoto University, Sakyo-ku, Kyoto 606-8502*

*bDepartment of Physics, Tohoku University, Sendai Miyagi 980-8578*

Johari-Goldstein (JG) relaxation, also known as slow β relaxation, is a relaxation phenomenon observed in supercooled liquids and glasses [1-2]. It plays a significant role in impacting various properties, including but not limited to the impact strength of the materials, particularly below the glass transition temperature. However, despite its importance, the precise physical mechanism underlying JG relaxation remains elusive. This challenge arises primarily due to the inherent difficulties in both experimental observation and numerical simulation of this phenomenon.

In our study, we delved into the Johari-Goldstein mode in both ionic glass CKN and metallic glasses. We carried out molecular dynamics simulations of 2376 molecules up to 12msec for the ionic glass CKN, and 32000 atoms interacting through EAM potentials for metallic glass ZrCuAl, with LAMMPS.

Our simulations unveiled the intricate microscopic dynamics characterizing the JG mode. Specifically, we observed that a subset of particles undergoes thermally activated jump motions, a hallmark behavior of the JG mode. Remarkably, these jump motions triggered a collective local relaxation among neighboring particles that were conventionally assumed to be immobile. This collective relaxation, involving both jumping and non-jumping particles, played a pivotal role in the stress relaxation of the entire glass structure [3].

By bridging findings from gamma ray quasi-elastic scattering experiments with the computational insights, our work provides a deeper understanding of the underlying mechanisms governing the JG mode in diverse glassy materials, thereby advancing our knowledge of their structural dynamics.

## References

[1] G. P. Johary and M. Goldstein, J. Chem. Phys. **53**, 2327 (1970).

[2] K. L. Ngai, Relaxation and diffusion in complex systems, Springer, Berlin, 2011.

[3] M. Saito, T. Araki, Y. Onodera, K. Ohara, M. Seto, Y. Yoda and Y. Wakabaashi, submitted.

# Topological and mechanical properties of colloidal gels

Koichi HIRATA and Takeaki ARAKI

*Department of Physics,*

*Kyoto University, Kitashirakawa-oiwake cho, Sakyo-ku, Kyoto 606-8502*

We numerically investigated the aggregation dynamics and resulting network structures of colloidal gels using slippery diffusion-limited cluster aggregation (DLCA) model. In this model, bonds are irreversibly formed upon the particle contacts, but the angles among them are not fixed unlike the conventional DLCA. This allows clusters to be deformed in the process of aggregation. We carried out Brownian dynamics simulations of 10648 particles with a code we have developed. By characterizing the aggregation dynamics and using reduced network scheme, our simulation revealed two distinct branching structure formation routes depending on the particle volume fraction $\phi$. In lower volume fraction systems $\phi \leq 8\%$, the deformations of small-size clusters proceed prior to the percolation.

When the Maxwell criterion is satisfied and the clusters become mechanically stable, the formation of the branching structure is nearly completed. After forming the branching structures, they aggregate and form larger percolating network. Then, the aggregation proceeds through the elongation and straightening of the chain parts of the network.

In higher volume fraction systems ($\phi > 8\%$), on the other hand, the clusters percolate and fine and homogeneous branching structure is formed at the early stage of the aggregation. In aging stage, it collapses into denser and more heterogeneous structure, and becomes more stable. Our quantitative analyses on the branching structure will shed light on a new strategy for describing the network formation and elasticity of colloidal gels.
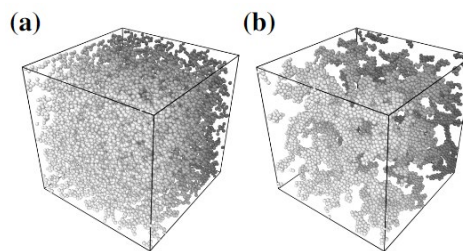


Fig. 1: Snapshots of the simulated gel structure at the final state of (a) DLCA and (b) the slippery DLCA.

# References

[1] S. Babu, *et al.*, Eur. Phys. J. E **27**, 297 (2008).

[2] M. Gimperlein *et al.*, arXiv:2312.11156 [cond-mat] (2023).

# Physical origin of forming ferroelectric nematic phase

Matheus DE MELLO and Takeaki ARAKI

*Department of Physics,*

*Kyoto University, Kitashirakawa-oiwake cho, Sakyo-ku, Kyoto 606-8502*

The nematic phase is a distinct state among liquid crystal phases, characterized by the alignment of rod-like molecules along a preferred direction. In the ordinary nematic phase, the preservation of head-tail symmetry prevents the manifestation of ferroelectricity, which has been not discovered for a long time. It was not until 2017 that the experimental realization of two distinct low molecular weight compounds exhibiting ferroelectricity marked a significant breakthrough. Despite extensive studies, the physical mechanism underlying the emergence of ferroelectricity in nematic liquid crystals remains elusive. This study aims to explore and understand the unique properties and underlying mechanisms of this phase.

Our investigation focuses on systems composed of DIO. Utilizing Gaussian16, we obtained the electric charge distribution to assign the partial charge on each atom. Subsequently, employing GROMACS, we conducted molecular dynamics simulations of 1000 DIO molecules. To elucidate the roles of electrostatic interaction, we also carried out simulations of 2048 DIO molecules without the electric charges.

Our simulations reveal spontaneous polarization in the charged DIO, albeit with the polarization degree smaller than the experimental observations. We attribute this weaker ferroelectricity to computational limitations, as molecular motions are quite slow within the simulation time. On the other hand, spontaneous polarization is not observed in the chargeless system, indicating the electrostatic interaction promotes polarization, in contrast to ordinary nematic phases.
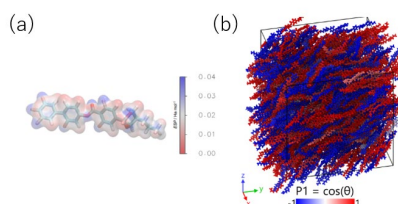


Fig. 1: (a) Electrostatic isopotential of DIO. (b) Snapshot of the DIO system at 330K.

# References

[1] H. Nishikawa, *et al*., Adv. Matter. **29**, 1702354 (2017).[2] R. J. Mandle, *et al*., Phys. Chem. Chem. Phys. **19**, 11429 (2017).

# Simulation of Quantum Many-Body Systems by Tensor Network and Sampling

Synge TODO

*Department of Physics, University of Tokyo, Tokyo, 113-0033*

We developed novel numerical methods by combining Monte Carlo, tensor network algorithms, and other optimization techniques. We investigated topological quantum phase transitions in strongly correlated many-body systems and optimization of quantum operations in quantum computing.

*Negative Sign Problem in Quantum Monte Carlo Methods*

The quantum Monte Carlo method for quantum many-body systems is a widely used computational technique. However, a negative sign problem arises in some quantum lattice models, and the statistical error increases exponentially at low temperatures. To address this problem, we redefine the negative sign problem as an optimization problem by integrating the basis transformation and the reweighting method. In particular, we found that assuming a frustration-free system simplifies the optimization function and effectively reduces the negative sign. Numerical simulations confirm that the proposed method performs well for spin systems for which analytical solutions exist and for frustration-free systems for which solutions are unknown.

*Effective Dimension in Long-Range Interacting Systems*

In quantum critical phenomena, long-range interactions are of interest in that the effective dimension of the system can be varied by controlling the anisotropy in space and time by the decay rate of the interaction. However, comprehensive and accurate numerical analysis remains challenging due to the exten-
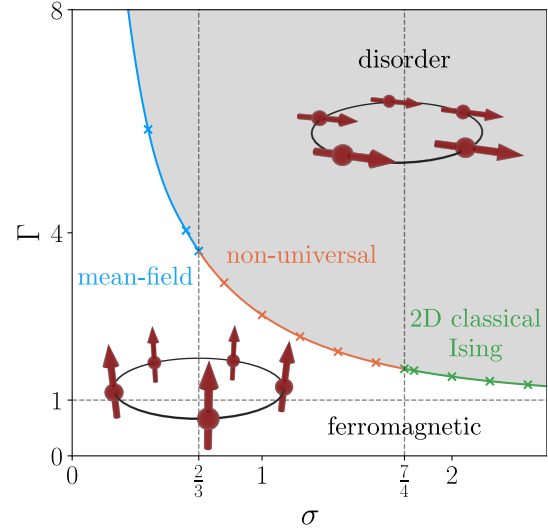


Figure 1: Ground-state phase diagram of long-range interacting transverse-field Ising chain.

sive search space with additional degrees of freedom governing the interaction and strong finite-size effects. We have shown that the problem can be significantly improved by automatically adjusting the parameters of the model under the guiding principle of "setting the correlation ratio in the spatial/temporal axes to the same and optimal value," and have also successfully determined the universality class boundary for the quantum phase transition of the one-dimensional transverse-field Ising model (Fig. 1).

*Quantum Monte Carlo in Continuous Space Systems*

For interacting bosons such as $He^4$, it is difficult to sample physical quantities related to quantum statistics, such as the superfluid

density and condensate fraction. Conventional Monte Carlo updates cannot change the path winding number. We incorporate the path-integral quantum Markov-chain Monte Carlo method for continuous-space many-body systems with exchange Monte Carlo and population annealing developed for simulations of spin glass systems. By slowly turning on the interaction in different imaginary-time slices and moving from a non-interacting system to a fully interacting one, we confirm that updates to the winding number can be achieved quickly.

*Application of the Grassmann tensor network to lattice fermion systems*

The tensor renormalization group approach has been applied to the simulation of lattice field theories at finite density for over a decade. We construct a Grassmann tensor network representing the partition function of 1+1-dimensional SU(2) Yang-Mills theory coupled with staggered fermion on a square lattice. The gauge group integration is discretized using a random sampling method, and the Grassmann integral of staggered fermion fields is written as the trace of a Grassmann tensor network by introducing auxiliary Grassmann fields. Since the theory has massive internal degrees of freedom, the bond dimension of the initial tensors is at least in the order of $10^2$. So, performing accurate TRG calculations with these initial tensors is difficult. We introduce an efficient initial tensor compression scheme. After that, the Grassmann bond-weighted tensor renormalization group algorithm is applied to contract the Grassmann tensor network composed of the compressed tensors. Physical quantities such as the number density and the fermion condensate in the thermodynamic limit can be computed by finite differences in the partition function.

*Noise Model Estimation Based on Syndrome Statistics of Surface Codes*

The surface code attracts attention as a practical error correction code in quantum computation. Although the decoding algo-
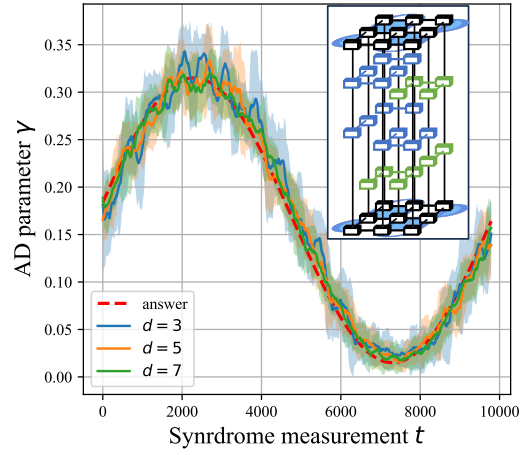


Figure 2: Estimation of time-varying noise models based on syndrome statistics.

rithm for surface codes can improve performance by using information from noise models, additional measurements are required because the noise model information must be prepared in advance by tomography. Estimating the noise model based on the results of syndrome measurements obtained during the decoding process can prevent performance degradation without additional quantum computation. We have developed a method combining a tensor network simulator for surface code with Monte Carlo techniques to estimate noise model parameters beyond the Pauli noise. We have successfully estimated various noise models, including a time-varying amplitude-decaying noise model, and have also confirmed that using the estimated results improves the performance of decoding algorithms (Fig. 2).

# Efficient sampling simulation of the soft modes significantly contribute to protein properties

Hiroshi Kono, Kazuhiro Takemura, Duy Tran, Wijaya Tegar, Hao Thai Nguyen, Ting-yi Chu, Shinji Ikizawa, Sari Hagimoto, Tatsuhiro Kimizono, Yusei Ito, Akio Kitao

*School of Life Science and Technology,*

*Tokyo Institute of Technology, Ookayama, Meguro-ku, Tokyo 152-8550*

Almost all organisms, including humans, require sugars such as glucose as an energy source. Therefore, many organisms possess the ability to uptake sugars into their bodies, and one of the proteins responsible for this function is SGLT. SGLT (Sodium Glucose Cotransporter) is a protein that transports glucose and sodium simultaneously. Through this mechanism, it performs secondary active transport by utilizing the potential generated by the sodium concentration gradient between the intracellular and extracellular spaces to uptake glucose from the extracellular to the intracellular space. In humans, six isoforms of SGLT have been discovered so far, each with strict sugar selectivity [1]. For example, while SGLT1 transports both glucose (Glc) and galactose (Gal), SGLT2 transports only Glc and not Gal. The recognition mechanism that can distinguish specifically between Glc and Gal, which structurally have minor differences, has been the subject of research. However, studies approaching the principles of selectivity by observing dynamics using molecular dynamics (MD) simulations have not been extensively

conducted. The objective of this study is to elucidate the dynamic mechanism at the atomic level by which SGLT recognizes monosaccharides such as Glc and Gal. Generally, substrate transport by transporters involves steps where the substrate approaches from one side of the cell membrane, binds to a binding site located inside the membrane, and then, through structural changes, a pathway opens to the opposite side for the substrate to move across. In the fiscal year 2023, as the first stage of the research, detailed investigation of interactions in the binding state located inside the membrane and simulations of dissociation from the binding state to the extracellular side were conducted.

We performed normal molecular dynamics (MD) simulations for 1 μs using the complex of Glc or Gal with SGLT1 as the initial structure（PDB: 7wmv）. The protein force field was AMBER19SB [2], the force field for Glc and Gal was GLYCAM06 [3], and the water model used was OPC [4]. After that, we next conducted dissociation simulations of the glycans from the bound state using the Parallel Cascade Selection Molecular Dynamics (PaCS-MD) simulation [5-

7]. In this study, we performed 60 MD parallel runs for 100 ps per PaCS-MD cycle. The ranking and selection of structures of each cycle was based on the inter-center of mass distance of the protein and the ligands. PaCS-MD stopped when center of mass distance reached 7.5 nm.

Prior to PaCS-MD, classical 1 μs MD simulations were conducted five times each for Glc and Gal. Analysis of hydrogen bonding between the protein and the ligand revealed significant differences in the number of hydrogen bonds between W291 and Glc or Gal. W291 formed more hydrogen bonds with Gal than Glc as shown in Figure 1. These differences in hydrogen bonding suggest that the difference in affinity between Glc and Gal in SGLT1 may be due to this.

Furthermore, dissociation simulations to the extracellular side were performed using PaCS-MD, with 20 trials each for Glc and Gal. Dissociation was observed 20 times for Glc and 16 times for Gal. Calculations of the binding free energy $\Delta G_O$ using Markov State Modelling yielded values of -11.1 kcal/mol for Glc and -9.6 kcal/mol for Gal in Figure 2. This difference corresponds to the difference in binding affinity $K_m$ for Glc/Gal in SGLT1 measured experimentally, suggesting that selectivity occurs at the binding step.
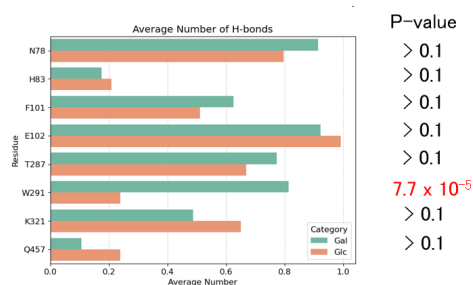


Figure 1. Comparison of the number of hydrogen bonds formed between each residue and Glc/Gal.



$$\Delta G^o = \Delta G_{PMF} + \Delta G_v$$

$\Delta G^o = -8.8 - 2.3 = -11.1\ [\text{kcal/mol}] \qquad \Delta G^o = -8.0 - 1.6 = -9.6\ [\text{kcal/mol}]$
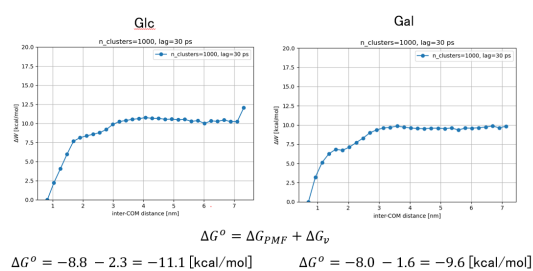
Figure 2. Free energy landscape along the center of mass distance and standard binding free energy.

# References

[1] L. Han et al., Nature 601, 274 (2022).

[2] C. Tian et al., J. Chem. Theory Comput. 16, 528 (2020).

[3] K. N. Kirschner et al., J. Comput. Chem. 29, 622 (2008).

[4] S. Izadi et al., J. Phys. Chem. Lett 5, 3863 (2014).

[5] D P Tran et al., J. Chem. Theory Comput. 14, 404 (2018).

[6] D. P. Tran, A. Kitao, J. Phys. Chem. B 123, 2469 (2019).

[7] S. Ikizawa et al., J. Phys. Chem. B 128, 3631 (2024).

# Improvement of analysis for relaxation of fluctuations by the use of Gaussian process regression

Y. Ozeki and Y. Osada

*Graduate School of Informatics and Engineering, The University of Electro-Communications*

We investigate an improvement for the numerical estimations of critical exponents due to non-equilibrium relaxation (NER) of fluctuations. [1] The numerical derivative which is necessary to estimate the asymptotic exponent of relaxation is improved as a smooth function by the use of the Gaussian process regression and kernel method. [2]

To estimate critical exponents in the NER method [?]ome relaxation functions are calculated at the transition temperature, which are numerically estimated usually; the order parameter $m(t)$ as well as the dimensionless susceptibility $f_{mm}(t) \equiv N\left(\frac{\langle m^2 \rangle_t}{\langle m \rangle_t^2} - 1\right)$, and another dimensionless correlation function, $f_{me}(t) \equiv N\left(\frac{\langle me \rangle_t}{\langle m \rangle_t \langle e \rangle_t} - 1\right)$, where $m$ and $e$ represent the order parameter and the energy per site, $N$ is the number of sites, and $\langle \cdots \rangle_t$ denotes a dynamical average at time $t$. At the critical point, these functions are expected to show algebraic behaviors asymptotically as

$$m(t) \sim t^{-\lambda_m}, \quad f_{mm}(t) \sim t^{\lambda_{mm}}, \quad f_{me}(t) \sim t^{\lambda_{me}}. \tag{1}$$

The dynamical exponents are related with the conventional critical exponents as

$$\lambda_m = \frac{\beta}{z\nu}, \quad \lambda_{mm} = \frac{d}{z}, \quad \lambda_{me} = \frac{1}{z\nu} \tag{2}$$

If the above dynamical functions are estimated numerical by Monte Carlo simulations, one can define the following logarithmic derivative

$$\lambda_m(t) \equiv -\frac{\partial \log m(t)}{\partial \log t}, \tag{3}$$

which would approaches $\lambda_m$ as $t \to \infty$. We call this function the local exponent of $\lambda_m$ Similarly, other local exponents

$$\lambda_{mm}(t) \equiv \frac{\partial \log f_{mm}(t)}{\partial \log t}, \quad \lambda_{me}(t) \equiv \frac{\partial \log f_{me}(t)}{\partial \log t}, \tag{4}$$

are defined, which would approach $\lambda_{mm}$ and $\lambda_{me}$, respectively.

Previously, to evaluate conventional critical exponents, we first calculate the functions $m(t)$,
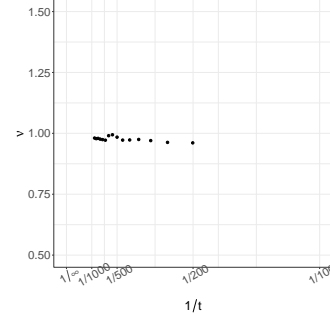


Figure 1: The local exponent $\nu(t)$ for the 2D Ising model plotted as a function of $1/t$ evaluated by the previous analysis using the numerical derivative.

$f_{mm}(t)$ and $f_{me}(t)$ numerically for a finite system up to a maximum observation time $t_{\max}$ due to Monte Carlo simulations. The system size $N$ is chosen so that the size dependence does not appear in the calculated functions up to $t = t_{\max}$. This provides the analysis corresponding to an infinite system. Then, the local exponents defined in Eqs. (3)-(4) are evaluated by numerical derivative for a finite interval of time, and are extrapolated to obtain the dynamical exponents (2) providing conventional critical exponents $\nu, \beta, z$.

The above method is efficient and reliable in the numerical evaluation of critical exponents. However, there has been a kind of difficulty in the extrapolation scheme of local exponents. Numerically evaluated local exponents are obtained in discrete time, and are sometimes not smooth functions because of the numerical derivative on simulated values. Thus, the extrapolation of them to $t \to \infty$ cannot be done systematically and yields unstable results. To overcome this difficulty, we applied Gaussian process regression and the kernel method as in the dynamical scaling analysis which has been used successfully. This improvement enables comparison of exponents at multiple critical points of various systems. This will greatly advance the discussion of universality.

As an example, we show a result for the ferromagnetic Ising model in two dimensions. The cal-
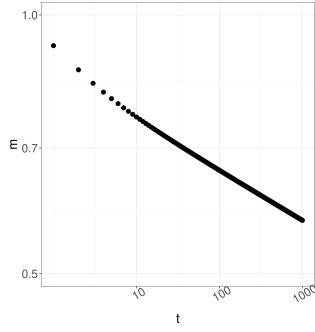
Figure 2: The relaxation of order parameter $m(t)$ for the 2D Ising model plotted in a double-logarithmic scale.



Figure 4: The local exponent $\lambda(t)$ evaluated by the differentiation of the curve shown in Fig.3.



Figure 3: The result of interpolation for $-\log m(t)$ as a function of $\log t$. The black points indicate the interval where the numerical data exist, and the red ones indicate out of that.
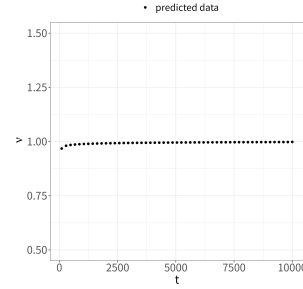


Figure 5: The extrapolation of local exponent $\nu(t)$ evaluated by the present method.

culation is carried out at the exact transition temperature $T = 2,2691853$ on $501 \times 500$ lattice; $10^7$ samples are used for averaging; the observation is made for $10^2 \leq t \leq 10^4$ MCS. The relaxation functions $m(t)$, $f_{mm}(t)$ and $f_{me}(t)$ are calculated. First, we show the result obtained by the previous analysis using the numerical derivative; in Fig.1, the resulting local exponent of $\nu$ defined by

$$\nu(t) \equiv \frac{\lambda_{mm}(t)}{d\,\lambda_{me}(t)} \qquad (5)$$

is plotted. As pointed out above, the data point is discrete and is not smooth.

In the present method, we interpolate the relaxation data using the Gaussian process regression and the kernel method. In Fig.2, the numerical data for $m(t)$ is plotted with a double-logarithmic scale. The result of interpolation for $-\log m(t)$ as a function of $\log t$ is shown in Fig.3, where we use the fact that the curve reaches the origin $(0,0)$. At least the interval where the numerical data exist, the obtained smooth curve is much precise and can be differentiate at any point. Then, we evaluate the

local exponent $\lambda(t)$ as a smooth curve in this interval (shown in Fig.4). and the extrapolation can be performed. The same procedure is made for other relaxation functions $f_{mm}(t)$ and $f_{me}(t)$. In Fig.5, the resulting extrapolation is performed for $\nu(t)$ by the use of the Shanks transformation. [3] We obtain $\beta = 0.1250(4)$ and $\nu = 1.000(2)$ in this demonstration, while $\beta = 1/8$ and $\nu = 1$ are known as exact values. It is shown that the present method works well.

# References

[1] Y. Ozeki and N. Ito, *J. Phys.: Math. Theor.* **40** R149 (2007).

[2] Y. Echinaka and Y. Ozeki, *Phys. Rev.* E**94** 043312 (2016).

[3] D. Shanks, *J. Math. and Phys.* **34** 1 (1955).

# The Anderson transitions in quasi-periodic systems

TOMI OHTSUKI[1]
TOHRU KAWARABAYASHI[2]
KEITH SLEVIN[3]

1) Dept. Phys., Sophia University, Chiyoda-ku, Tokyo 102-8554, Japan
2) Dept. Phys., Toho University, Miyama 2-2-1, Funabashi 274-8510, Japan
3) Dept. Phys., Osaka University, Toyonaka, Osaka 560-0043, Japan

Random quantum systems, lacking translational and rotational symmetries, display time reversal, chiral, and particle-hole symmetries, classifying them into ten symmetry classes. Significant research has focused on the Wigner-Dyson classes identified in the 1950s and 1960s. Recent advancements in experimental techniques have shifted focus to the quasi-periodic potentials. Random potentials cause wave function localization in one-dimensional systems, while quasi-periodic potentials result in both localization and delocalization. The impact of quasi-periodicity in higher-dimensional systems is an active research topic [1-3].

We study three-dimensional systems where the translational invariance is broken by quasi-periodic potentials. We analyzed system size dependence of conductance and used finite-size scaling to estimate critical points and exponents, covering orthogonal, unitary, and symplectic Wigner-Dyson classes. The results showed that critical exponents match those in random potential systems, indicating that the universality classes remain the same in the case of quasi-periodicity. We also note the shifts of the critical strength of potential ($V_c$) due to the violation of time reversal and spin rotation symmetries are consistent with the weak localization theory.

Furthermore, we employed a three-dimensional convolutional neural network (CNN) for wave function analysis (Figure 1). Initially trained on the Anderson localization model, the CNN was adapted to assess wave functions under quasi-periodic potentials, differentiating between localized and delocalized states.

**References**
1. S. Sakai, R. Arita, Tl Ohtsuk: Physical Review B **105**, 054202 (2022)
2. S. Sakai, R. Arita, Tl Ohtsuk: Physical Review Research **4**, 033241 (2022)
3. X. Luo, T. Ohtsuki, Physical Review B **106**, 104205 (2022).
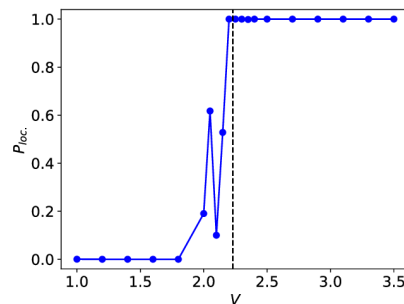
Figure 1: Probability of localization ($P_{loc}$) for wave functions in quasiperiodic systems as a function of quasiperiodic potential strength ($V$), as predicted by a convolutional neural network trained on the localized/delocalized wave functions from the disordered Anderson model. The critical point ($V_c$) is marked by the vertical dashed line. Each data point's probability is the average of 10 samples. The analysis focuses on a wave function near $E=0$ within a cubic system of linear size $L=42$. Taken from Ref. [3].

# Molecular dynamics simulation of protein aggregation

Hisashi Okumura

*Exploratory Research Center on Life and Living Systems,*

*Institute for Molecular Science, Okazaki, Aichi 444-8585*

When protein concentration increases due to aging or other reasons, they aggregate and cause various diseases. For example, Alzheimer's disease is considered to be caused by aggregates of amyloid-beta (Aβ) peptide, and polyglutamine disease by aggregates of polyglutamine. Aβ peptide usually consists of 40 or 42 amino acid residues. Aβ peptide with 40 residues is referred to as Aβ40, and that with 42 residues is referred to as A42. We have performed molecular dynamics (MD) simulations to understand the aggregation and disaggregation mechanisms of Aβ peptides. In this fiscal year, we performed large-scale MD simulations of Aβ peptide aggregation.

We performed all-atom MD simulations of 32 Aβ40 and Aβ42 peptides in explicit water solvent for 1.8 μs. All of the Aβ peptides were placed discretely in the initial conditions. MPI/OpenMP hybrid parallelization was used to execute the large jobs. We observed Aβ peptides aggregated with repeating aggregation and disaggregation. They finally formed large oligomers, as shown in Fig. 1. We revealed structural changes in the aggregation process, inparticular forcusing on the aspect ratio of the oligomers and secondary structure.



Typical structures of Aβ oligomers

dodecamer          heptamer
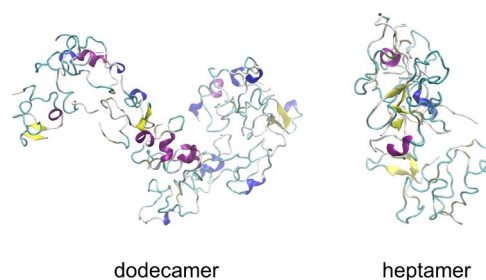
Fig. 1 Typical conformations of amyloid-β (Aβ) oligomers obtained by molecular dynamics simulations.

We found that the relatively large oligomers tend to have a long aspect ratio. It means that small oligomers are relatively spherical, but tend to extend in one way as they get larger. In addition, the oligomers of Aβ42 formed more β-hairpin and intermolecular β-sheet structures than those of Aβ40. We are now trying to reveal the reason for these structural features.

It isn't easy to clarify the growth process of Aβ oligomers at the molecular level by wet experiments. However, MD simulation can reproduce it as if it had been seen. We believe that elucidating the initial process of Aβ aggregation at the molecular level through this study will provide important knowledge for developing future therapies.

# Thermal effects on quantum frustrated magnetisms

Tokuro Shimokawa

*Theory of Quantum Matter Unit, Okinawa Institute of Science and Technology Graduate University, Onna 904-0495, Japan*

Investigating the effects of thermal fluctuations in quantum frustrated magnets is crucial for developing our understanding of quantum spin liquids. $Ca_{10}Cr_7O_{28}$ (CCO) [1] is a quantum spin liquid candidate that can be described by the S=1/2 bilayer breathing kagome (BBK) Heisenberg model. Here, we examine the importance of thermal fluctuations by focusing on the $J_1$-$J_2$ classical honeycomb-lattice Heisenberg model corresponding to the classical system of this S=1/2 BBK model.

To do this, we employ classical Monte Carlo simulations, utilizing a hybrid parallelization approach combining the heat-bath method, over-relaxation method, and replica exchange method. We investigate the ordering behavior of the honeycomb lattice model in a finite-temperature magnetic field with a focus on the several $J_2/J_1$ parameter values. Physical quantities, including specific heat, magnetic susceptibility, equal-time structure factor, and chirality, are examined to identify the presence of a Skyrmion lattice state with sublattice structure and other additional multiple-q states [2].

We also report on the investigation of the static and dynamic properties of the S=1/2 $J_A$-$J_B$-$J_C$ honeycomb-lattice Heisenberg model, which is believed to be important for understanding the quantum spin liquid behavior in different honeycomb-lattice material $Cu_2(pymca)_3(ClO_4)$ [3]. The investigations were carried out using quantum Monte Carlo simulations based on ALPS application [4] and exact diagonalization. Our results demonstrate the realization of a quantum paramagnetic state in this material, and suggest that focusing on dynamic properties is crucial for experimentally identifying this state [5].

## References

[1] C. Balz, *et al.* Nat. Phys. **12** 942 (2016).

[2] T. S., *et al*, in preparation

[3] Z. Honda, *et al*, J. Phys. Soc. Jpn. **84**, 034601 (2015).

[4] A. Albuquerque, *et al*, J. Magn. Magn. Mater. **310**, 1187 (2007).

[5] T. S., Ken'ichi Takano, Zentaro Honda, Akira Okutani, and Masayuki Hagiwara, Phys. Rev. B **106**, 134410 (2022).

# Numerical study on low-energy states of quantum spin systems

Hiroki NAKANO

*Graduate School of Science, University of Hyogo*
*Kouto, Kamigori, Hyogo 678-1297, Japan*

The difficulty in accurately estimating physical quantities is due to the many-body problems researchers encounter in condensed matter physics. The quantum spin system is a typical problem. In studying a quantum spin system, numerical approaches have been widely and effectively used. Computational studies have provided us with valuable information about the target systems.

Three methods have been successfully employed in the field of quantum spin systems. The traditional one is the numerical-diagonalization method. The quantum Monte Carlo (QMC) simulation is the second method. The third method is the density matrix renormalization group (DMRG) method. Although each of these methods has benefits, they also have drawbacks. QMC simulations are capable of handling systems that are significantly larger, regardless of their spatial dimensions. On the other hand, the negative sign problem with this approach prevents us from accurately evaluating physical quantities in frustrated systems. When the spatial dimension of a target system is one, however, the DMRG method is very useful, regardless of whether or not the target system includes frustration. Regrettably, this method is still in progress for cases where the spatial dimension is larger than one. Regardless of the presence of frustrations or the spatial dimension, the numerical diagonalization method can be applied to various systems. However, the method is limited to treating systems with very small sizes.

In order to overcome this drawback of the numerical diagonalization method, we developed a hybrid-type parallelized code of Lanczos diagonalization[1]. This code enables us to treat various large systems that have not been treated yet using this method. As a primary approach in this project, we utilize this method to examine various quantum spin systems.

In 2023, this project reported our achievement concerning the Shastry-Sutherland model, namely, the $S = 1/2$ Heisenberg antiferromagnet on the orthogonal dimer lattice [2]. In this study, we successfully carried out Lanczos diagonalizations of this system up to 48 sites. Within Lanczos-diagonalization studies, this size was treated for the first time to the best of our knowledge. Note here that the largest treated matrix dimension is 32,247,603,683,100. The properties of this model are determined by the ratio of two interaction amplitudes denoted by $r = J_2/J_1$, where $J_1$ denotes the amplitude of the Heisenberg interaction at the orthogonal dimer and $J_2$ denotes the amplitude of interaction forming the square lattice. Our result concerning the edge of the exact-dimer phase for the 48-site system is $r = 0.67542$. From the comparison between the 44- and 48-site systems, our conclusion for the edge of the exact-dimer phase is

$$r = 0.6754(2). \tag{1}$$

This result was compared with the result obtained in electron spin resonance measurements under high pressure and high field[3]

and discussed the difference between the experimental and theoretical results from the viewpoint of Dzyaloshinski-Moriya interactions that are not taken into account in the theoretical model. Our studies contribute much to our deeper understandings of the quantum magnetism. Further investigations would clarify nontrivial quantum effects in these systems.

# References

[1] H. Nakano and A. Terai: J. Phys. Soc. Jpn. **78**, 014003 (2009).

[2] H. Nakano and T. Sakai: JPS Conf. Proc. **38**, 011166 (2023).

[3] T. Sakurai, Y. Hirao, K. Hijii, S. Okubo, H. Ohta, Y. Uwatoko, K. Kudo, and Y. Koike: J. Phys. Soc. Jpn. **87**, 033701 (2018).

# Multiscale simulations for complex flows

Yohei MORII and Toshihiro KAWAKATSU

*Department of Physics,*

*Tohoku University, Sendai, Miyagi 980-8578*

We have developed a platform for multiscale simulations on complex flows named MSSP (Multi-Scale Simulation Platform for complex flows), where a macroscopic flow simulator based on smoothed particle hydrodynamics (SPH) and microscopic molecular dynamics simulators embedded in each of SPH particles are coupled [1]. In the present project, we studied the Marangoni effect of surfactant adsorbed on an oil/water interface. For this purpose, we implemented an evaluation method of surface tension and a diffusion process of microscopic molecules between adjacent SPH particles. We prepared an oil droplet in a water matrix and injected a micellar solution of surfactant (Fig.1), where the micelles are regarded as deformable objects and show viscoelastic response to external flow field.

In Figs.2 and 3, we show the simulation results using 10,000,000 micelles on MSSP for the system shown in Fig.1 [2]. We can successfully observe the deformation of oil droplet caused by the Marangoni effect.

## Acknowledgement
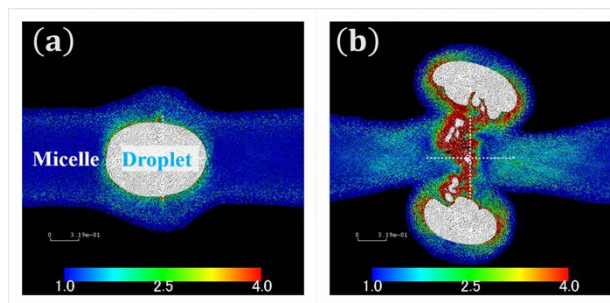
Fig.2 Configurations of micelles around the droplet for (a) low and (b) high affinity of surfactant to the interface.
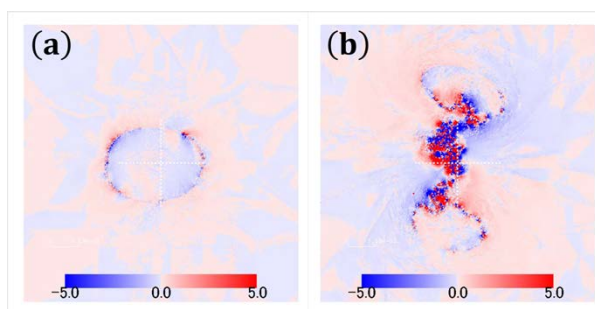


Fig.3 Distribution of vorticity.

## References

[1] Y.Morii and T.Kawakatsu, Phys. Fluids, **33**, 093106 (2021).

[2] Y.Morii and T.Kawakatsu, *in preparation*.

Fig. 1: Setting of the simulation system.

# Search for magnetic skyrmion by machine learning

Satoru Hayami

*Graduate School of Science, Hokkaido University, Sapporo 060-0810, Japan*

A topological spin texture, which shows distinct physical phenomena from conventional ferromagnetic and antiferromagnetic spin textures, has been extensively studied in both theory and experiment. Among them, a magnetic skyrmion characterized by a topologically-nontrivial swirling spin texture has been a central subject in topological magnetism since its discovery in 2009. Although a skyrmion crystal phase consisting of a periodic array of the magnetic skyrmion in a crystal has been observed in various materials, its stabilization conditions in terms of the lattice structure and magnetic interactions have not been fully elucidated. In the project with number 2023-Ca-0002, we have numerically investigated the stabilization mechanism of magnetic skyrmion crystal phases by considering various situations. We have presented the main results this year below.

*(i) Anisotropic spin model and multiple-Q states in cubic systems:* We have constructed an effective spin model with magnetic anisotropic interactions in cubic systems [1]. By considering the symmetry conditions to possess the Dzyaloshinskii-Moriya interaction and symmetric anisotropic interaction in momentum space, we have classified the nonzero anisotropic interactions at high-symmetry wave vectors in both centrosymmetric and noncentrosymmetric cubic space groups. We have also demonstrated that the obtained anisotropic spin model exhibits the instability toward a variety of multiple-Q states including the hedgehog-antihedgehog crystal.

*(ii) Skyrmion crystals in noncentrosymmetric cubic magnet: Cases of O, T, and $T_{\mathrm{d}}$:* We have investigated the low-temperature magnetic phase diagrams of the spin model in three noncentrosymmetric cubic point groups, $O$, $T$, and $T_{\mathrm{d}}$ [2]. By performing the simulated annealing, we discussed the similarity and difference of the phase diagrams in each point group. We have found that the instability toward the skyrmion crystal is different for the point groups $(O, T)$ and $T_{\mathrm{d}}$ according to the different nature of the Dzyaloshinskii-Moriya interaction; the skyrmion crystal is stabilized only for the point groups $(O, T)$, while that is not for $T_{\mathrm{d}}$. Meanwhile, we have clarified that the skyrmion crystal phase can appear in the case of the point group $T_{\mathrm{d}}$ once the effect of the uniaxial strain lowering the symmetry to $D_{2\mathrm{d}}$ is introduced.

*(iii) Antiferro skyrmion crystal phases in a synthetic bilayer antiferromagnet under an in-plane magnetic field:* We have investigated the possibility of stabilizing the antiferro skyrmion crystal without the uniform scalar chirality in synthetic layered antiferromagnets [3]. By considering the centrosymmetric bilayer structure with the staggered Dzyaloshinskii-Moriya interaction, we have found that the antiferro skyrmion crystal is induced in an external magnetic field. We summarized four conditions to stabilize the antiferro skyrmion crystal in the ground state: (1) the staggered DM interaction, (2) the easy-plane single-ion anisotropy, (3) the interlayer exchange interaction, and (4) the in-plane magnetic field. Additionally, we have shown that the ferri-type skyrmion crystal is stabilized next to the antiferro skyrmion crystal.

*(iv) Magnetic bubble crystal in tetragonal magnets:* We have investigated the stabilization mechanisms of a magnetic bubble crystal, which consists of a superposition of double-$Q$ sinusoidal waves, in centrosymmetric tetragonal magnets [4]. We constructed the magnetic-field-temperature phase diagrams while changing the easy-axis magnetic anisotropic two-spin interaction by the efficient steepest descent method. We found that there are two key ingredients in addition to the easy-axis two-spin magnetic anisotropy to realize the bubble crystal: the high-harmonic wave-vector interaction and the biquadratic interaction. We showed that the bubble crystal phase tends to appear in the high-temperature region of the skyrmion crystal phase for a moderate easy-axis anisotropic two-spin interaction; they are transformed into each other by changing the temperature. In addition, we showed that the bubble crystal remains stable in the zero-temperature limit for the large high-harmonic wave-vector interaction or biquadratic interaction in addition to the large easy-axis anisotropic two-spin interaction.

*(v) Multiple-$Q$ dipole–quadrupole instability in spin-1 triangular-lattice systems:* We have investigated the multiple-$Q$ instability in the classical $S = 1$ model with magnetic dipole and electric quadrupole degrees of freedom on a triangular lattice [5]. By systematically performing the simulated annealing for the effective models with various multipole–multipole interactions, we have found that four out of the fifteen models show the triple-$Q$ ground states. These triple-$Q$ states are stabilized as a consequence of the interplay between the dipole and quadrupole interactions, which requires neither single-ion magnetic anisotropy nor higher-order mode–mode couplings. We have also discussed the effect of the hexagonal crystalline electric field and the appearance of charge disproportionation.

*(vi) Hybrid skyrmion and antiskyrmion phases in polar $C_{4\mathrm{v}}$ systems:* We have ex-amined the role of the Dzyaloshinskii-Moriya interaction at low-symmetric wave vectors in noncentrosymmetric magnets [6]. We have analyzed the effective spin model on the polar square lattice, which is derived from the Kondo lattice model in the weak-coupling regime, by performing the simulated annealing. We have found that the direction of the Dzyaloshinskii-Moriya vector affects the formation of the skyrmion crystals as well as the helicity of the spiral wave. We have shown that the rhombic skyrmion crystal is realized when the Dzyaloshinskii-Moriya vector lies in the $\langle 100 \rangle$ direction, while the square skyrmion crystal is realized for other cases. Furthermore, we have shown that the anti-type skyrmion crystal is also realized depending on the direction of the Dzyaloshinskii-Moriya vector, which provides another root to realize the anti-type skyrmion crystal even under polar symmetry.

# References

[1] R. Yambe and S. Hayami, Phys. Rev. B **107**, 174408 (2023).

[2] S. Hayami and R. Yambe, Phys. Rev. B **107**, 174435 (2023).

[3] S. Hayami, J. Phys. Soc. Jpn. **92**, 084702 (2023).

[4] S. Hayami and Y. Kato, Phys. Rev. B **108**, 024426 (2023).

[5] S. Hayami and K. Hattori, J. Phys. Soc. Jpn. **92**, 124709 (2023).

[6] S. Hayami, Phys. Rev. B **109**, 054422 (2024).

# Dzyaloshinskii transition in a classical Heisenberg model of a chiral magnet

Yoshihiko NISHIKAWA

*Department of Physics, Kitasato University*
*Sagamihara, Kanagawa, Japan, 252-0373*

We have studied a classical Heisenberg model of a chiral magnet on a three-dimensional cubic lattice [1] with a clock perturbation. The Hamiltonian of the system is

$$H(\{\boldsymbol{S}_i\}) = - J_\parallel \sum_{\langle i,j \rangle_\parallel} \boldsymbol{S}_i \cdot \boldsymbol{S}_j - J \sum_{\langle i,j \rangle_\perp} \boldsymbol{S}_i \cdot \boldsymbol{S}_j$$
$$- \boldsymbol{D} \cdot \sum_{\langle i,j \rangle_\parallel} \boldsymbol{S}_i \times \boldsymbol{S}_j$$
$$- \delta \sum_i \cos\left(N_\delta \arctan\left(\frac{S_{i,z}}{S_{i,x}}\right)\right), \tag{1}$$

where $\boldsymbol{S}_i$ is a classical Heisenberg spin, $\boldsymbol{D} = D\boldsymbol{e}_y$ with $D > 0$, $\delta > 0$, and $N_\delta = 3$. The first and second summations run over pairs of neighboring spins with $\boldsymbol{r}_{ij} = \boldsymbol{r}_j - \boldsymbol{r}_i \parallel \boldsymbol{D}$ and $\boldsymbol{r}_{ij} = \boldsymbol{r}_j - \boldsymbol{r}_i \perp \boldsymbol{D}$, respectively. We fix $J_\parallel^2 + D^2 = 2J$. The Dzyaloshinskii–Moriya interaction, the third term in the Hamiltonian, induces a helical structure into the system at low temperature with its axis parallel to $\boldsymbol{D}$. If we set the boundary condition in the $y$ direction to be periodic, the system is forced to have a commensurate helical structure in the $y$ direction even when it does not naturally favor that winding number. This could make finite-size corrections significantly large. The boundary condition in the $y$ direction is thus set open, while those in the $x$ and $z$ directions are periodic in our simulation. The last term, although it looks unfamiliar, stands for a $N_\delta$-state clock perturbation: When $\arctan(S_{i,z}/S_{i,x}) = 2\pi n/N_\delta$ $(n \in \mathbb{Z})$, it gains an energy. Thus our system is a model of
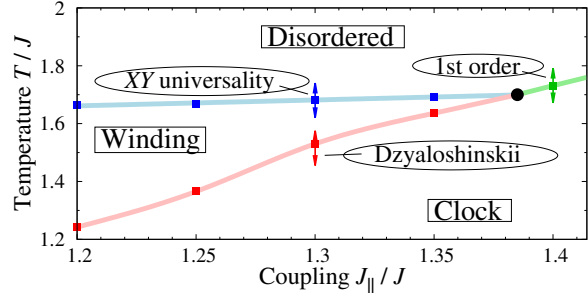


Figure 1: Phase diagram of the system. Depending on $J_\parallel/J$, the system has three qualitatively different phase transition: $XY$-type continuous transition, first-order transition, and Dzyaloshinskii transition.

chiral magnet with a clock perturbation. The linear length of the lattice is $L$ for the $x$ and $z$ directions and $L_y = 8L$ for the $y$ direction.

This model can be seen as an effective classical model of the J-Q model [2], a quantum spin model for studying the deconfined quantum criticality (DQC), with a chiral perturbation. A recent work [3] has argued that a field breaking the chiral symmetry of the system is a relevant perturbation for the putative DQC point, and has shown that it indeed induces a qualitatively different phase transition between the *helical valence-bond* (HVB) and the valence-bond solid (VBS) phases. Motivated by their work, we study the phase transitions in the effective classical model and discuss its detailed characterization.

We show the phase diagram of the model in Fig. 1. When $J_\parallel/J < 1.38$, the system has two phase transition when decreasing temper-

ature. The one at lower temperature, dubbed as *Dzyaloshinskii transition* [4], separates the winding phase, in which the system has a clear helical structure, and the clock phase with a homogeneous magnetization. This corresponds to the HVB-VBS transition found in the JQ model, and we focus on it in the following.

We define the winding number per spin

$$w = \frac{1}{L_y} \sum_k \theta_{k+1} - \theta_k, \qquad (2)$$

where $\theta_k = \arctan(\boldsymbol{m}_{k,z}/\boldsymbol{m}_{k,x})$ with

$$\boldsymbol{m}_k = \frac{1}{L}^2 \sum_i \delta_{i_y,k} \boldsymbol{S}_i. \qquad (3)$$

Here, $i_y$ indicates the $y$ component of the position of spin $i$ and $\delta$ is the Kronecker delta. We then calculate the free energy of the system as a function $w$

$$f(w) = -\frac{\beta^{-1}}{8L^3} \log \int d\boldsymbol{S}\delta(w(\boldsymbol{S}) - w) \exp(-\beta H) \qquad (4)$$

using the replica-exchange Wang-Landau [5] and multicanonical simulations [6] at a fixed temperature. Our results clearly show that, in the vicinity of the transition, the free energy has many minima while at high temperature it is convex and simple, see Fig. 2. Each minimum corresponds to a helical structure with a certain number of winding, and transition between them needs a subextensive but $O(L^2)$ free energy. The number of minima grows as $L_y$, suggesting, at $L \to \infty$ and $L_y \to \infty$, the system has an infinite number of free-energy minima. This clearly characterizes the peculiar nature of the phase transition: Despite its continuous nature, the system has an infinite number of locally stable states at the transition, realizing an interesting counterexample to the Ginzburg-Landau-Wilson picture for conventional critical points. We will further discuss the dynamical properties of the Dzyaloshinskii transition in future work.

This work was done in collaboration with Jun Takahashi.
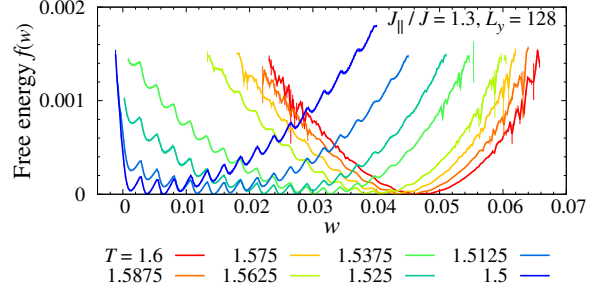


Figure 2: Free energy of the system as a function of the winding number $w$. See main text for its definition.

# References

[1] Y. Nishikawa and K. Hukushima, Physical Review B **94**, 064428 (2016)

[2] A. W. Sandvik, Physical Review Letters **98**, 227202 (2007).

[3] B. Zhao, J. Takahashi, and A. W. Sandvik, Physical Review Letters **125**, 257204 (2020).

[4] I. E. Dzyaloshinskii, JETP **19**, 960 (1964).

[5] F. Wang and D. P. Landau, Physical Review Letters, **86**, 2050 (2001); T. Vogel *et al.*, Physical Review Letters, **110** 210603 (2013).

[6] B. A. Berg, T. Neuhaus, Physical Review Letters, **68**, 9 (1992).

# Dynamics in Active Cyclic Potts Model

Hiroshi NOGUCHI

*Institute for Solid State Physics, University of Tokyo*

Various spatiotemporal patterns have been observed in nonequilibrium active systems. Many phenomena are well-captured by a description in terms of nonlinear but deterministic partial differential equations. However, noise effects are not understood so far. We focused on the effects of thermal fluctuations, since they are significant on a molecular scale.

We simulated the nonequilibrium dynamics of a Potts model with three cyclic states ($s = 0$, 1, and 2) [1]. The neighboring sites of the same states have an attraction to induce a phase separation between different states, and they have a cyclic state-energy-difference in the rock–paper–scissors manner. It is a model system for chemical reactions on a catalytic surface or molecular transport through a membrane. For the reaction case, the three states are reactant, product, and unoccupied sites. For the transport case, the molecule can bind to both surfaces and flip between these two states. In a cyclically symmetric condition, we found two dynamic modes: homogeneous cyclic mode and spiral wave mode. At a low cycling energy $h$ between two states, the homogeneous dominant states cyclically change as $s = 0 \rightarrow 1 \rightarrow 2 \rightarrow 0$ via nucleation and growth, as shown in Fig. 1(a). In contrast, spiral waves are formed at high energy $h$, as shown in Fig. 1(b). The waves are generated from the contacts of three states and rotate around them.

For large systems, a discontinuous transition occurs from these cyclic homogeneous phases to spiral waves, while the opposite transition is absent. Conversely, these two modes can temporally coexist for small systems, and the ratio of the two modes continuously changes with increasing $h$. The transition from the homogeneous cyclic to spiral wave modes occurs by the nucleation of the third state during the do-
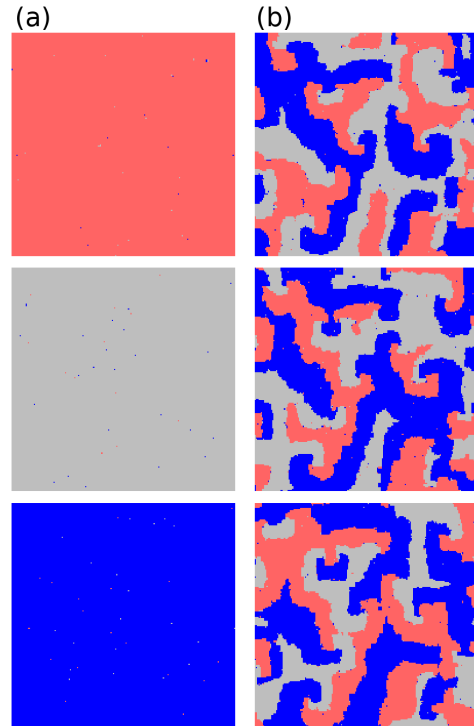


Figure 1: Sequential snapshots of active cyclic Potts model. (a) Homogeneous cyclic mode at $h = 0.8$. (b) Spiral wave mode at $h = 1.1$. The states, $s = 0$, 1 and 2, are displayed in gray, blue, and red colors, respectively.

main growth, while the transition to the homogeneous cyclic mode occurs through the disappearance of three-state contacts. With increasing system size, the former rate increases but the latter rate exponentially decreases. The transition character is changed by these size dependencies.

## References

[1] H. Noguchi, F. van Wijland, and J.-B. Fournier, J. Chem. Phys. 161, 025101 (2024).

# All-Atom Molecular Dynamics Simulation Study of Polymer Dynamics in Nanoporous Materials

Nobuhiko HOSONO

*Department of Applied Chemistry, Graduate School of Engineering,*

*The University of Tokyo, 7-3-1 Hongo, Bunkyo-ku, Tokyo 113-8656*

Metal–organic frameworks (MOFs) are crystalline compounds with numerous nano-sized pores capable of encapsulating molecules ranging from small gas molecules to extremely long polymers, as demonstrated by previous research [1]. Specifically, experiments and MD simulations have elucidated that polymer chains with elongated structures thread into the pores of MOFs from their termini, gradually uncoiling their entangled conformations [2]. Recently, we experimentally discovered that the polymer infiltration rate and diffusion pathways within the pores significantly vary depending on the chemical structure of the polymer chains [3]. In this study, we conducted all-atom MD simulations of this polymer diffusion process to gain molecular-level insights into the mechanism behind the polymer structure's influence on diffusivity in MOF nanopores.

We utilized the LAMMPS package for the all-atom MD simulation and selected a typical pillared-layer type MOF, $[Zn_2(1,4\text{-}ndc)_2(ted)]_n$ (ndc = naphthalenedicarboxylate, ted = triethylenediamine). To examine the effect of substitution groups on the PEG chain, we also designed and used a PEG with a phenyl group at the middle of the chain. Initial structures were constructed by placing guest PEG molecules in contact with the (001) surface of the MOF. The MD simulations were conducted at 393 K for 100 ns with MPI process (Figure 1). The infiltration process of the PEG chains within the MOF nanopores was tracked, and diffusion kinetics and pathways were investigated. Results clearly indicate differences in diffusion pathways as well as diffusion rates between unsubstituted PEG and phenyl-substituted PEG. We observed that even minor structural alterations on the polymer chain significantly influence the diffusion process and infiltration behavior of polymers within the MOF nanopores. This phenomenon holds promise for new polymer separation applications.
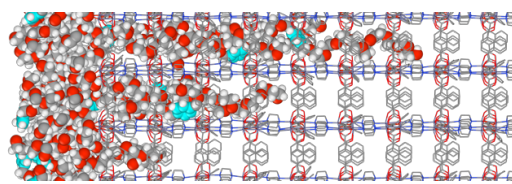


**Figure 1.** A snapshot of the MD

**References**

[1] N. Oe, N. Hosono, and T. Uemura, Chem. Sci. **12**, 12576 (2021).

[2] T. Uemura *et al.*, J. Phys. Chem. C **119**, 21504 (2015).

[3] N. Mizutani *et al.*, J. Am. Chem. Soc. **142**, 3701 (2020).

# Dynamic friction of macroscopic objects

Michio OTSUKI

*Graduate School of Engineering Science,*

*Osaka University, Machikaneyama, Toyonaka, Osaka 560-8531*

Amontons-Coulomb law of friction states that the friction coefficient does not depend on the shape of objects or the relative velocity between two objects in contact. However, the phenomenological explanation of the law is based on the adhesion of microscopic asperities at friction interface and implicitly assumes the uniformity of the stress field. A recent study has revealed that the static friction coefficient depends on the shape of the 3D rectangle block, which indicates the breakdown of the law, due to the nonuniform stress field [1].

In this study, we conducted simulations on static friction of grooved objects and hysteresis friction of viscoelastic objects using finite element method with parallel computing. The computational size is 500,000 nodes and billions of time steps, which takes 50 hours using our in-house code compiled with the Intel Fortran compiler and 1,700 MPI processes on the CPU servers.

First, we investigated the friction of a 3D grooved block on substrate using finite element simulation [2], as shown in Fig. 1. The results show that the static friction coefficient decreases with increasing groove width and depth. A theoretical analysis based on a simplified model reveals that the static friction coefficient is related to the critical area of the slow precursor slip. The decrease in the effective viscosity leads to the decrease in the friction coefficient.

We also investigated the hysteresis friction of viscoelastic objects, as shown in Fig. 2. The results show that the friction coefficient depends on the relative velocity between objects and takes different peaks at certain velocities depending on the viscosity. We also find that the type of deformation changes in high velocity region depending on the viscosity.
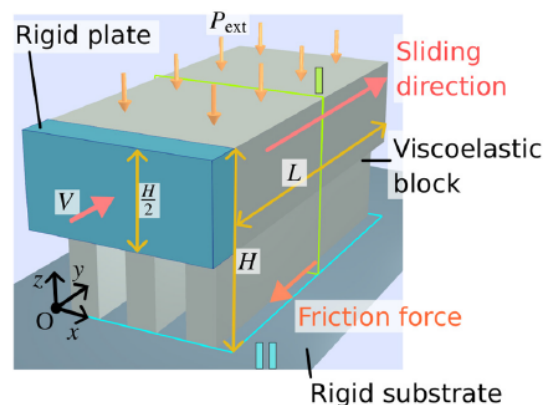


Fig. 1: Schematic of the grooved block [2].
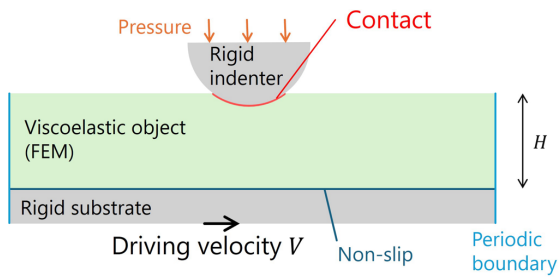
Fig. 2: Schematic of the grooved block.

## References

[1] W. Iwashita, H. Matsukawa, and M. Otsuki, Sci. Rep. **13**, 2511 (2023).

[2] W. Iwashita, H. Matsukawa, and M. Otsuki, Tribol. Lett. **72**, 25 (2024).

# Development of calculation methods for time correlation functions requiring long time computations

Takahiro MURASHIMA

*Department of Physics, Tohoku University*

*Aramaki-aza-Aoba, Aoba-ku, Sendai, Miyagi 980-8578*

Melts composed of polymers have long relaxation times, and various physical properties are correlated for long periods of time. To efficiently perform the calculation of the correlation function requiring long computation time in molecular dynamics (MD) simulations, it is necessary to develop an efficient method for calculating the correlation function and to accelerate the speed of MD simulations. For an efficient method of computing correlation functions, we have the multiple-tau method [1] developed by Ramirez et al. I extended the algorithm to calculate various physical quantities and improved it to run the correlation functions for each molecule in parallel. The developed program is packaged in a form that can be run on LAMMPS [2]. For speeding up MD simulations, GPUs are utilized. Specifically, I developed a hybrid simulation method in which MD simulations are performed by HOOMD-blue [3] and correlation function calculations are performed by LAMMPS. These improvements enable the computation of long-time time-correlation functions to be performed

more efficiently than before. Figure 1 shows the mean-square displacement of the middle particle in a polymer chain with length $N$. The appearance of a region of $t^{1/4}$ [4], characteristic of entangled polymer chains with $N \geq 100$, indicates that our method computed correctly. This result is in preparation for submission to a journal.
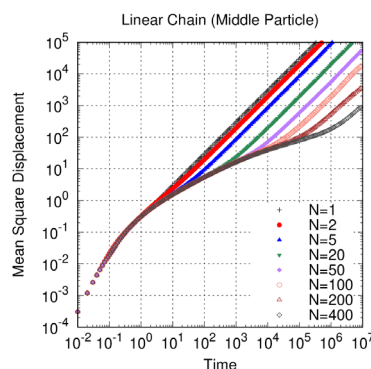


Fig. 1: Mean square displacement of the middle particle in a linear chain composed of $N$ particles.

# References

[1] J. Ramirez et al., *J. Chem. Phys.* **133**, 154103 (2010).

[2] S. Plimpton, *J. Comput. Phys.* **117**, 1 (1995).

[3] J. Anderson et al., Comput. Mater. Sci. **173**, 109363 (2020).

[4] M. Doi, S. F. Edwards, The Theory of Polymer Dynamics, Oxford (1986)

# Supersolid in Bose-Hubbard model with titled dipole interactions

Takafumi SUZUKI

*Graduate School of Engineering,*

*University of Hyogo, Shosha, Himeji, Hyogo 670-2280*

We have used ISSP supercomputer resources for the following two topics: (1) supersolid states in two-dimensional hard-core bosonic Hubbard model with dipole interactions and (2) dynamical properties of the extended honeycomb-lattice Kitaev-Γ model.

## (1) Superolid in Bose-Hubbard model with titled dipole interactions

For realizing supersolid [1,2], many efforts have been made so far. Experimentally ultracold atomic gases trapped in optical lattices are promising stages for realizing the supersolid. Theoretically frustrated interactions are significant to stabilize the supersolid states in lattice Bose-Hubbard models. The authors in ref. [3] have investigated the ground-state phase diagram of the two-dimensional bosonic Hubbard model with the dipole-dipole interactions by the mean-field (MF) approach and infinite entangled-pair-state (iPEPS) calculations. When the dipole axis is tilted on the two-dimensional lattice plain and the cut-off distance for the dipole-dipole interactions is restricted, the MF approach and iPEPS calculations predicted that several supersolid phases appear in between solid phases with different commensurate fillings.

In this project, we investigated the ground-state phase diagram of this model by quantum Monte Carlo (QMC) calculations. To characterize the nature of each phase appeared, we applied not only conventional finite-size-scaling approaches but also a machine-learning assisted approach. In the machine-learning assisted approach, we prepare the multi-convolutional neural network (mCNN) that was trained by magnetization snapshots obtained from classical Monte Carlo simulations or the several Ising models. The snapshots include several ordered phases, such as ferromagnetic, Neel, stripe, and up-up-down (down-up-up) ordering, which are possible ordered phase in the target quantum model. We checked the accuracy of the mCNN for the hard-core Bose Hubbard model on the triangular lattice, where the supersolid state arises in a low temperature. We confirmed that the mCNN network quantitatively predicts the phase transition temperature for the emerging the 1/3 (2/3) solid order and is not affected by the emergence of the superfluidity.

By utilizing the mCCN, we classified phases of the Bose-Hubbard model with tilted dipole interactions. We find that the QMC results reproduce the phase diagram obtained by the MF approach and iPEPS calculations [3]. By changing the cut-off distance for the long-range dipole interactions, we further investigate the phase diagram.

## (2) Dynamical properties of the extended S=1 honeycomb-lattice Kitaev-Γ model

In this project, we have investigated ground states and dynamical properties of the extended S=1 Kitaev-Γ model on a honeycomb lattice by the numerical exact diagonalization and density-matrix-renormalization-group approaches. In the previous study, we focused on the S=1/2 case and investigated the effect of anisotropy of the interaction; we connect the spin chain model and the isotropically interacting model on the honeycomb lattice by tuning the interactions [4]. We clarified that the Tomonaga-Luttinger liquid (TLL) appearing in the spin chain limit [5] persists for the finite interchain interactions and it becomes a proximate Tomonaga-Luttinger liquid (pTTL), which is analogous to sliding TLL [6]. In addition, the phase diagram near the isotropically interacting limit includes characteristic natures; (1) when K is ferromagnetic and Γ is antiferromagnetic, the three-fold degenerated phase whose phase boundary is characterized by the first order transition appears in $1/6 < K/|\Gamma| < 1$ and otherwise, the model is located at the phase boundary between the pTLL-like (almost one-dimensional) state and dimerized phase. In this

project, we have investigated the S=1 case. We found that the three-fold degenerated phase is also confirmed in the S=1 case.

## References

[1] G. V. Chester, Phys. Rev. A **2**, 256 (1970).

[2] A. J. Leggett, Phys. Rev. Lett. **25**, 1543 (1970).

[3] H. -K. Wu and W. -L. Tu, Phys. Rev. A **102**, 053306 (2020).

[4] M. Gohlke, J. C. Pelayo, and T. Suzuki, arXiv:2212.11000.

[5] W. Yang, et al., Phys. Rev. Lett. 124, 147205 (2020) and W. Yang, A. Nocera, and I. Affleck, Phys. Rev. Research 2, 033268 (2020).

[6] R. Mukhopadhyay, C. L. Kane, and T. C. Lubensky, Phys. Rev. B **64**. 045120 (2001).

# Analyses on the Potential-dependent Dynamics of Ionic Liquid Electrolytes Forming Electric Double Layers Facing the Electrodes

Ken-ichi FUKUI

*Department of Materials Engineering Science, Graduate School of Engineering Science,*

*Osaka University, Machikaneyama, Toyonaka, Osaka 560-8531*

Electric double layer-organic field effect transistor (EDL-OFET) using an ionic liquid (IL) as a gate dielectric has attracted much attention, because EDL formed at IL/semiconductor interface reduces the operating voltage for accumulation of carriers at the interface [1]. Thus, the response of interfacial IL to the potential change of the gate voltage is important for device performance. However, details of solvation structure and dynamics of ionic liquids at the interfaces are still not clear. In this study, we performed classical molecular dynamics (MD) simulation to investigate the local structure of interfacial IL and its response to the potential change of $C_n$-DNBDT-NW crystalline single-layer (semiconductor) film, whose interfaces were recently analyzed by interfacial spectroscopy [1].

All MD simulations were conducted by classical MD package of GROMACS-5.0.7. A simulation cell ($7.3 \times 7.9$ nm$^2$ in-plane) contains 800 ion pairs of EMIM-FSI as IL and a single $C_n$-DNBDT-NW layer. To reproduce the potential dependent behavior of the IL at the interface, hole charges were uniformly distributed on the atoms constituting the HOMO of $C_n$-DNBDT-NW and corresponding ions were removed to maintain the cells neutral. Local structures of the IL at the interface depending on the interfacial potential were evaluated from 20 ns MD trajectories at 400 K after 4.0 ns equilibration run.

At the potential of zero charge (PZC) without any apparent change at the $C_9$-DNBDT crystalline film, the anions and cations showed a checkerboard-like local structure in the region of 3 Å from the film surface. (Fig. 1a). At -1.0 V, the anions were more strongly localized on the crystal film surface, while keeping the character of the

checkerboard structure (Fig. 1c). In the region from 3 Å to 6 Å from the $C_9$-DNBDT film surface, the cations were dominant at both of PZC and -1.0 V (Fig. 1c and d). These characteristics were common when the alkyl chain length ($C_n$) was changed from 1 to 8. Angle distribution analyses at the interfaces showed an interesting feature that the interfacial EMIM cation was aligned its imidazolium ring more perpendicular to the surface of hole injected films with even chain numbers ($C_n$).
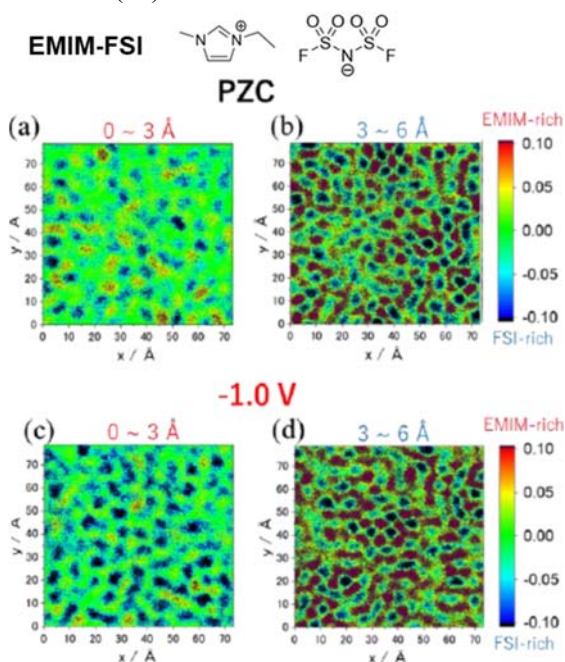


Fig. 1 2D distribution of cations (red) and anions (blue) at the IL / $C_9$-DNBDT-NW interface.

## Reference

[1] T. Okamoto, et al. *J. Am. Chem. Soc.* **142**, 9083 (2020).
[2] Tanabe, K. Fukui, and coworkers, *Commun. Chem.* **4**, 88 (2021).

# Molecular dynamics simulation for chemical reactions in multicomponent systems of thermosetting resins

Yutaka Oya

*Department of Materials Science and Technology,*

*Tokyo University of Science, Niijuku, Katsushika-ku, Tokyo 125-8585*

We quantitatively evaluated the damage of thermosetting resins using molecular dynamics (MD) simulations. To achieve this goal, we needed to address two challenges related to the "changes in polymer topology," which are typically difficult to simulate using conventional classical molecular dynamics methods. The first challenge is reproducing the chemical reactions of thermosetting resins. The second is to mimic the dissociation of covalent bonds induced by mechanical loading. Thermosetting resins form dense crosslinked structures through chemical reactions between the base resin and curing agent. In the previous year, we focused on creating these crosslinked structures and developed MD methods to reproduce the mechanical properties of multicomponent epoxy systems. In this year, we have developed an algorithm in MD for bond dissociation and quantitatively evaluated the stress-strain curves of epoxy resins and entropy as a measure of damage. Below, we describe the overview of our approach.

In this study, DGEBA was used as the base resin and 44-DDS as the curing agent for epoxy resin. The base resin has two epoxy groups at both ends, while the curing agent has two primary amine groups at both ends as well. The primary amine groups react with the epoxy groups to form secondary amines, and further reaction of the secondary amines with epoxy groups results in tertiary amines. Branching formed by such sequential reactions spreads throughout the system, leading to the formation of a crosslinked structure. By reproducing such chemical reactions, a crosslinked structure shown in Figure 1 was obtained. This crosslinked structure has a curing degree of 0.83, showing good agreement with previous research results [1].
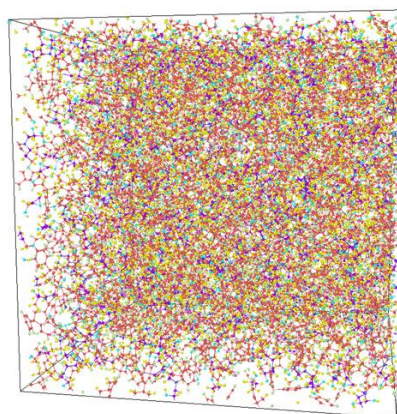


Figure 1. Crosslinked structure formed by chemical reaction.

A uniaxial tensile test was conducted on the obtained crosslinked structure for the stress-strain relationship. The strain rate was set to $5.0 \times 10^9$, and a pressure of 1 atm was applied in perpendicular to the tensile direction. The system temperature was set to T = 300K. During the uniaxial tensile test, internal covalent bonds were broken. In this study, a distance-based covalent bond dissociation algorithm was introduced to evaluate internal damage. Specifically, each covalent bond was eliminated when its length exceeded 1.1 times the natural length. Furthermore, a very short NVT relaxation (10fs) was introduced after covalent bond dissociation to alleviate sudden forces acting on the atoms.

Figure 2 depicts the stress-strain curve, entropy generation, and bond dissociation obtained from the uniaxial tensile simulation. Incorporating covalent bond dissociation, the maximum strength is reached at around 6 percent strain, and fracture occurs at 15 percent strain. In contrast, in conventional MD simulations without considering covalent bond dissociation, the system continues to deform without a decrease in stress. From the stress-strain curve, the resulting entropy generation is evaluated as shown in Figure 2 (b), indicating an increase in Fig. 1: Supercomputer System B at SCC-ISSP.
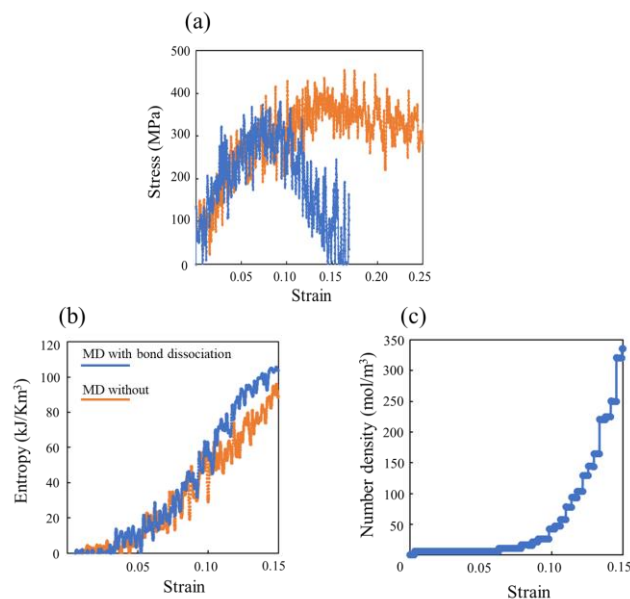


Figure 2. (a) Stress-strain curves with and without bond dissociations, (b) Entropy generation, and (c) Number density of dissociated covalent bonds.

entropy due to covalent bond dissociation. The results of the number of bond dissociation, as depicted in Figure 2 (c), show a strong positive correlation with the increase in entropy. In summary, these findings underscore the importance of covalent bond dissociation in reproducing the mechanical properties of thermosetting resins.

## References

[1] Carla E. Estridge, *Polymer* 141 (2018), 12-20.

# New Monte Carlo approach: Kondo vs Kitaev

Masahiko G. YAMADA

*Department of Physics, School of Science, University of Tokyo*
*Hongo, Bunkyo-ku, Tokyo 113-0033*

We developed a new Monte Carlo method called an infinite product expansion (iPE) method [1]. This iPE method is applicable to both Kondo lattice models and Kitaev models for classical/quantum spin systems as an "order N" method for the finite-temperature calculation of quantumness.

For example in the case of the weight of Monte Carlo becomes $W \propto \det \cosh \frac{\beta(H-\mu)}{2}$ for a Hamiltonian $H$ with a chemical potential $\mu$. We can expand this as $\det \cosh \frac{\beta(H-\mu)}{2} = \det \prod_{n=1}^{\infty} \left\{ 1 + \left[ \frac{\beta(H-\mu)}{\pi(2n-1)} \right]^2 \right\}$. In this way, we can use the sparsity of the Hamiltonian ($H$ matrix) to accelerate the Monte Carlo drastically, down to orders $O(N^2)$ or even $O(N)$.

We apply this new massive-scale Monte Carlo approach (iPE) to reveal two topological phenomena. First to reveal a new topological excitation of the Kondo lattice model, and second to reveal a new topological phase of the Kitaev model Larger $N$ calculations enabled by the massive parallelization will give us a further insight into the physics of topology in both a spin liquid and a localized spin picture.

For Kitaev models, many new topological phase transitions, even inside exactly solvable regions can be expected in its phase diagram. Specifically, a larger $N$ simulation may discover a new Berezinskii-Kosterlitz-Thouless transition inside the Kitaev model, which is always difficult to prove because of the logarithmic correction.

For Kondo cases, there are many more. Topological excitations like skyrmions, hedge-hogs, Hopfions are expected, and we are now exploring such possibilities in large (real-space) systems of Kondo lattice models. Rich variety of phase diagrams can newly be investigated by our new approach (iPE).

# References

[1] M. G. Yamada, Y. Akagi, and M. Udagawa: to appear.

# Kinetics of phase transition and polyamorphism

Kazuhiro FUCHIZAKI

*Department of Physics, Ehime University, Matsuyama 790-8577*

Nowadays, it is generally known that a kind of intermediate-length scale order is developed in a metastable amorphous state compared to the corresponding stable liquid phase. In FY2023, as sufficient structural data were stored, we examined the structural similarities and differences between the liquid phases of $SnI_4$ and their amorphous states.

The ambient-pressure crystalline phase CP-I of $SnI_4$ was found to undergo pressure-induced amorphization at around 15 GPa on compression [1], and the amorphous state was named Am-I, which transforms with a discontinuous density decrease to another amorphous state Am-II on the return way to CP-I. Recently, we recognized that Am-I could be further classified into two structures depending on pressure: the high-density state Am-IH, composed of dissociated tin and iodine atoms, and the relatively low-density state Am-IL [2]. The transition between these states occurs continuously from 14 to 18 GPa [2].

Meanwhile, Liq-II, the stable liquid phase for CP-I and Am-II, undergoes a liquid–liquid transition (LLT) to Liq-I at 1.5 GPa and 970 K [3]. This LLT is associated with a subtle change (0.3-0.4 g/cc) in density [4]. No molecular dissociation has been confirmed in Liq-I up to 3.4 GPa, the highest pressure attained thus far. Therefore, the structural comparison here is restricted to Liq-II/Am-II and Liq-I/Am-IL.

Liq-II and Am-II have similar structures; they consist of randomly oriented molecules with perfect tetrahedral symmetry $T_d$. Similar structural factors characterize them; their snapshot aspects can only be distinguished by the degree of crowding, i.e., the density of molecules.

As far as the length scale of the order of a molecule is concerned, the situation in Liq-I and Am-IL is again said to be similar. The symmetry of molecules is locally broken; the symmetry is lowered from $T_d$ to $C_{3v}$ or $C_{2v}$ [2, 5]. (The author speculates that the symmetry lowering is not a result but the trigger of the transition [5]. Introducing the two different length scales by symmetry lowering can facilitate the induction of compressional (dilatational) density waves.) However, a difference between Liq-I and Am-IL has been recognized for the structure beyond the intermediate length scale. Am-IL's structure factor does have a bump at 4.4 $\text{Å}^{-1}$, which is missing in Liq-I's. The origin of this intermediate length-scale order remained unanswered except that it is ascribable to the spatial correlation between iodine atoms [2].

To answer this problem, reverse Monte Carlo (RMC) simulations [6] were conducted again, but with an increased system size of 8000 $SnI_4$ units, compared to the previous one with 2744 units [2], to gain better statistics. Although the densities were available, the initial configurations of units used as input to the RMC simulations were prepared using molecular dynamics simulations.

In order to interpret the output configurations from the RMC simulations, the formation of a metallic $I_2$ bond was assumed if an intermolecular distance between iodine atoms of adjacent $SnI_4$ units fulfills the following two criteria simultaneously: i) the distance is less than 3.1 Å [7] and ii) the units

on both sides are deformed. This latter condition ii) was introduced because the molecular deformation, as examined below, could be regarded as a precursor to forming a chemical bond. Here, we call a segment satisfying the criteria a 'bond.' Such 'bonds' were found to be percolated throughout the system in Am-IL, whereas the size of clusters consisting of 'bonds' remained finite in Liq-I. Furthermore, the spatial distribution of iodine atoms belonging to a percolation cluster in Am-IL was confirmed to be responsible for the formation of the bump in the structure factor. Nonparticipating iodine atoms in a percolation cluster did not contribute to the bump. The bump thus does not emerge in the structure factor of Liq-I without a percolation cluster. A detailed report will be published in due course [8].

Finally, the relationship between molecular deformation and the possibility of 'bond' formation was examined based on quantum chemical considerations [9]. The related computations were not performed using ISSP supercomputers, and the results are kept concise. Two $SnI_4$ molecules could have a chance to form a physical 'bond' with a lifetime of the order of 0.1 ps when they approach closely within 10 Å. Interestingly, the 'bond' formation was induced by the deformation of molecules to $C_{3v}$ or $C_{2v}$ structures depending on their mutual orientations. However, the formation of a chemical bond has not yet been confirmed within available computation times.

## References

[1] Y. Fujii, M. Kowaka, and A. Onodera: J. Phys. C **18**, 789 (1985).

[2] K. Fuchizaki *et al.*: J. Phys.: Condens. Matter **33**, 365401 (2021).

[3] K. Fuchizaki *et al.*: J. Chem. Phys. **135**, 091101 (2011).

[4] K. Fuchizaki, N. Hamaya, and Y. Katayama: J. Phys. Soc. Jpn. **82**, 033003 (2013).

[5] K. Fuchizaki, T. Sakagami, and H. Iwayama: J. Chem. Phys. **150**, 114501 (2019).

[6] O. Gereben and L. Pusztai: J. Comput. Chem. **33**, 2285 (2012).

[7] K. Takemura *et al.*: Z. Kristallogr. Cryst. Mater. **219**, 749 (2004).

[8] K. Fuchizaki: to be presented in 61st EHPRG, 1–6 September 2024, Thessaloniki, Greece; to be published.

[9] M. J. Frisch *et al,*: GAUSSIAN 09 Revision E.01, Gaussian, Inc., Wallingford, CT, 2009.

# Physical properties of crosslinked polymer networks through network topology analysis

Katsumi HAGITA,[1] and Takahiro MURASHIMA[2]

[1]*Department of Applied Physics, National Defense Academy, Yokosuka 239-8686*
[2]*Department of Physics, Tohoku University, Sendai 980-8578*

To elucidate the topological effect on the physical/mechanical properties of the tetra-arm end-link gel/rubber, it is desirable to establish model approaches using coarse-grained MD (CGMD) simulations of the Kremer-Grest model and/or realistic approaches using all-atom MD (AAMD) simulations. There is a large gap in computational cost between CGMD and AAMD, and effective connections between them are also desired.

To develop a statistical approach to evaluate macroscopic properties of hydrogels from AAMD simulations, we studied poly(ethylene glycol) (PEG) hydrogels that show "negative energetic elasticity" [1]. In the analysis for experimental data, we estimated the linear relation $G = A (T - T_{E})$ between shear modules ($G$) and temperature ($T$) where $G$ was estimated from the relation $G = \sigma_{XY}/\gamma$ between shear stress ($\sigma_{XY}$) for each shear strain ($\gamma$). Here, $T_{E}$ is an indicator of a negative energetic elasticity. In AAMD simulations, because statistical errors in $\sigma_{XY}$ are significant, errors in $G$ are also significant and make difficult to confirm the relation $G = A (T - T_{E})$. We proposed a statistical approach [1] considering numerous datasets ($\sigma_{XY}$, $\gamma$, $T$) based on the multivariate regression of the equation $\sigma_{XY} = A\gamma (T - T_{E})$ in a narrow temperature range using fitting parameters $A$ and $T_{E}$. We confirmed the feasibility of the obtained $T_{E}$ values via a statistical error analysis [1].

To investigate diamond lattice structures with artificial irresolvable entanglements, we developed a method to obtain initial configurations of AAMD simulations by converting configurations obtained by CGMD simulations. In the CGMD simulations, the diamond lattice structures with the artificial irresolvable entanglements were generated in four steps as follows. (i) The box size of the periodic boundary condition (PBC) with the number density $\rho = 0.85$ of the melt without solvent is set to $L_{pbc,\rho=0.85}$, and the system is expanded by $a = 1.0, 1.2, 1,4, 1,6, 1,8$, and 2.0 times $L_{pbc,\rho=0.85}$. (ii) Equilibrium relaxation calculations were performed in which the chains were treated as a phantom chain by setting the excluded volume to 0 with the cos-type non-bonding interactions. (iii) A push-off operation restored the excluded volume and returned the phantom chain to the KG chain.

(iv) The PBC box size was decreased to $L_{\mathrm{pbc},\rho=0.85}$ for $a > 1.0$ and was rest for $a = 1.0$. The networks of KG model were converted to the networks of AA model by mapping from a KG bead to a carbon (or oxygen) atom. Then, water molecules were introduced in the gaps of the PEG network to achieve a target PEG concentrations c [g/L].

Figure 1 (a) summarized the stresses at strain of 5.0 and clarified the anisotropy of network. These behaviors were consistent with the primitive path analysis of the backbone of the PEG network. Figure 1 (b,c) shows stress–strain curves of various entangled networks of KG model (without solvent) under the elongation rate of 0.0001 and shear strain rate of 0.0001. We found that the expansion coefficient $a$ characterizes the elastic behavior. For $a = 1.0$, rapid increases of stresses were observed due to highly entangled structure. On the other hand, the stress–strain curves at $a = 1.8$ and 2.0 were close to a diamond lattice structure which has no entanglement. A future challenge will be to utilize this knowledge in the evaluation of actual material systems.

# References

[1] K. Hagita, S. Nagahara, T. Murashima, T. Sakai, N. Sakumichi, Macromolecules **56**, 8095-8105 (2023).
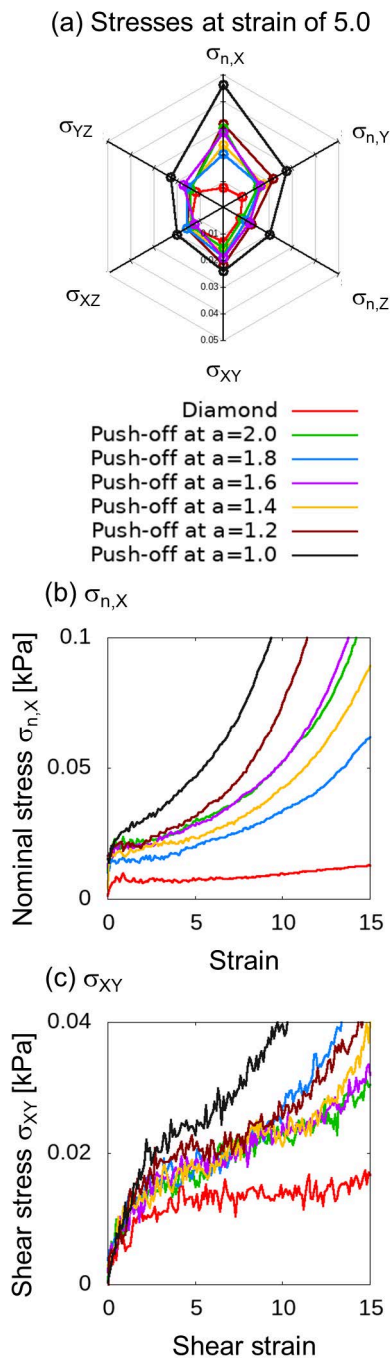


Fig. 1: Stresses of randomly entangled networks generated from a diamond lattice using a push-off procedure under different expansion coefficient $a$.

# Frustration and randomness in the honeycomb-lattice spin systems

Chitoshi YASUDA

*Department of Physics and Earth Sciences, Faculty of Science,*
*University of the Ryukyus, Okinawa 903-0213, Japan*

Honeycomb-lattice magnets have gotten a lot of attention recently. These include the honeycomb-lattice Kitaev model, in which the ground state is a quantum spin liquid, and the combination of metal complexes and ferdadylradicals, in which several types of randomly coexisting interactions exist. A new quantum spin liquid was found from experiments on a solid helium thin film. The low density of the film predicts that the helium atoms form a honeycomb lattice. In this project, we conducted two studies on the honeycomb lattice, (1) the site-dilution effects on the antiferromagnetic Heisenberg model, and (2) the multiple-spin exchange model describing well the magnetism of solid helium.

The ground-state phase diagram of the spin $S = 1/2$ and $S = 1$ antiferromagnetic (AF) Heisenberg model on a honeycomb lattice, which is composed of bond-alternating chains and interchain interactions, is investigated by the quantum Monte Carlo simulation with the continuous-imaginary-time loop algorithm [1]. The phase diagram is parametrized by the intrachain alternating coupling constant $\alpha$ and the interchain coupling constant $J'$. The ground state becomes the dimerized spin-gapped state or the AF long-range ordered state depending on the parameters $\alpha$ and $J'$. In the dimerized state realized for small $\alpha$ and $J'$, the finite correlation lengths are found to become relatively smaller than those of the square lattice [2]. The difference would be related to the difference in coordination number. The site-dilution-induced AF long-range order (LRO) has been also investigated in the honeycomb-lattice systems. As in the square-lattice systems [3], the results suggest that the LRO is induced at infinitesimal concentrations of dilution. However, its evaluation was more difficult than for the square-lattice systems. Specifically, the temperature that can be regarded as absolute zero has been lowered. We expect that the result could be due to the shortness of the correlation length of the pure system.

The multiple-spin exchange model is difficult to analyze due to its complexity. In this project, thermodynamic properties of ferromagnetic and AF states are investigated by using the molecular-field (MF) theory and the Green's function method. Within the MF approximation, we investigated the temperature dependences of magnetization and susceptibility, and obtained results suggesting that ferromagnetic and AF correlations are suppressed by the six-body exchange. In the Green's function method, which incorporates spin correlations rather than the MF approximation, we could have a formulation in which temperature fluctuations suppress magnetic orders.

# References

[1] S. Todo and K. Kato, Phys. Rev. Lett. **87**, 047203 (2001).

[2] M. Matsumoto, C. Yasuda, S. Todo, and H. Takayama, Phys. Rev. B **65**, 014407 (2001).

[3] C. Yasuda, S. Todo, M. Matsumoto, and H. Takayama, Phys. Rev. B **64**, 092405 (2001).

# Application of tensor networks in tensor data analysis

Kenji Harada

*Graduate School of Informatics, Kyoto University*
*Kyoto 606-8501, Japan*

In the fields of condensed matter and statistical physics, tensor networks have gained attention as a representation format for various many-body problems. These include ground states of quantum systems and nonequilibrium stationary distributions in time-evolving systems.

Various applications have proposed data science as a representation method for tensor data. For instance, an innovative approach to efficiently represent high-dimensional data distributions is a generative model that uses tensor networks[1, 2]. In this research project, we aim to further explore the application of tensor networks in the generative modeling.

Here, we consider a generative model based on a quantum state [1, 2]. Following the Born rule, we define $p(\mathbf{x})$ as the square of the amplitude of a wave function: $p(\mathbf{x}) = \frac{|\psi(\mathbf{x})|^2}{Z}$, where $\psi(\mathbf{x})$ is a wave function and $Z$ is the normalization factor.

Two different approaches, MPSs [1] and balance TTNs [2], have been proposed for defining the wave function in generative modeling. The number of indexes of a tensor in the balance TTN is equal to that in the MPS. However, the difference lies in the topology of the network. In the TTN, all physical indexes $x_i$ are connected, and there is no loop structure. Therefore, an MPS is a specialized type of TTN. It has been shown in [2] that the performance depends heavily on the network topology of TTNs.

We propose a new algorithm to optimize the network structure of a TTN for generative modeling. Various strategies can be employed to select a better local network structure [3]. Our network optimization technique enhances the performance of generative modeling with TTNs.

We applied our method to diverse data, including randomly generated data, stock price volatilities of companies embedded in stock indices, handwritten text images, and artificial data with stochastic dependencies. We aimed to examine the characteristics of these datasets. For example, through optimization, we discovered a network with topological coupling corresponding to the original dependencies of many data with stochastic dependencies, such as Bayesian networks.

## References

[1] Zhao-Yu Han, Jun Wang, Heng Fan, Lei Wang, and Pan Zhang. Unsupervised Generative Modeling Using Matrix Product States. *Phys. Rev. X*, 8(3):031012, 2018.

[2] Song Cheng, Lei Wang, T. Xiang, and Pan Zhang. Tree tensor networks for generative modeling. *Phys. Rev. B*, 99(15):155131, 2019.

[3] Kenji Harada, Tsuyoshi Okubo, and Naoki Kawashima. Network optimization of tree generative models. in preparation.

# The Study on Superionic Conduction and Phase Transition by Disordering of Complex Hydride

Ryuhei Sato

*Advanced Institute for Materials Research,*

*Tohoku University, 2-1-1 Katahira, Aoba-ku, Sendai 980-8577, Japan*

To improve ionic conductivity, it is important to understand the mechanism of many-body problems such as "concerted motion of ions" and "the coupling of transport ions with lattice vibrations and counterion rotation". So far, we have worked on physical properties related to ion conductivity, such as the mechanism elucidation of concerted transport mechanisms [1] and the role of neutral molecules in the bulk [2] and so on [3]. This year, the relationship between anion rotation and ion migration was analyzed by the trajectory of molecular dynamics simulations for $LiCB_9H_{10}$ having rotational complex anions ($CB_9H_{10}^-$).

Figure 1(a) shows an Arrhenius plot of Li diffusion coefficient obtained during machine learning potential molecular dynamics (MLP-MD) simulations. To improve the accuracy, MLP was reconstructed from the one used in the previous year. As a result, we succeeded in reproducing not only high-temperature (HT) phase but also the unknown low-temperature (LT) phase, although we slightly overestimated phase transition temperature. The diffusion coefficient increases by nearly two orders of magnitude before and after the phase transformation, confirming the large effect of anion rotation. The structure of the LT phase is shown in the fig. 1(b).
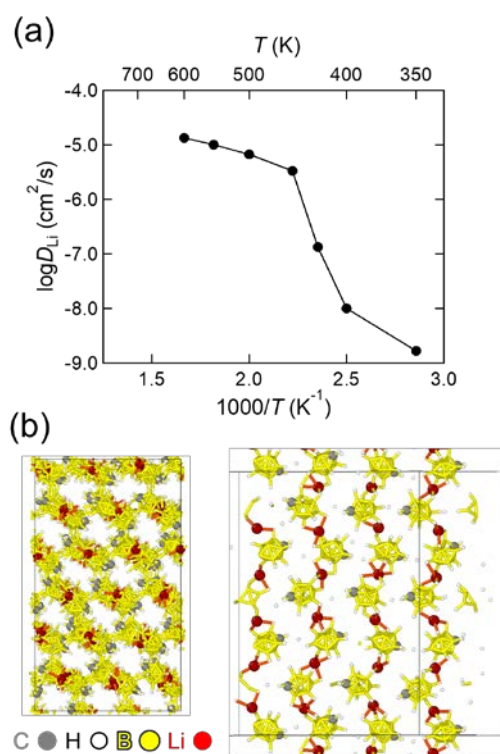


Fig. 1(a) Li diffusivity Arrhenius plot during MLP-MD simulation (b) Low T phase of $LiCB_9H_{10}$ obtained from MLP-MD simulation

It consists of a one-dimensional chain-like

structure of $CB_9H_{10}$ and Li ions. Li connects only in the opposite direction to the C atom of $CB_9H_{10}^-$ due to the positive charge of C atom in this cluster. This strong site selectivity of Li for $CB_9H_{10}^-$ prevents Li ions from migration within LT phase since complex anion hardly rotates at low temperatures. Whereas, once complex anions are thermally activated and rotates, Li ion migrates along with the rotation of these anions. In fact, the site selectivity is maintained even in HT phase, and Li is transported by the paddle-wheel mechanism.

Figure 2 shows a plot of the connectivity of Li ions during MLP-MD simulations for $LiCB_9H_{10}$ obtained from graph theory. The vertical axis represents the number of Li atoms in the bond chain, while the horizontal axis shows the cut-off radius value at which two Li atoms are regarded to be bonded. The probability density in each state is as shown in the color scale. As confirmed by the results for T = 300 K in the grey scale color map, short Li-Li bonds with a cut-off radius below 4.5 Å was not observed during MLP-MD simulation for LT phase at 300K. On the other hand, dimers or trimers with Li-Li distances below 4.5Å are identified in HT phase. This shows the stronger interaction between Li ions during Li migration, suggesting concerted motion of Li ions occur via these dimers or trimers with the help of anion rotation.
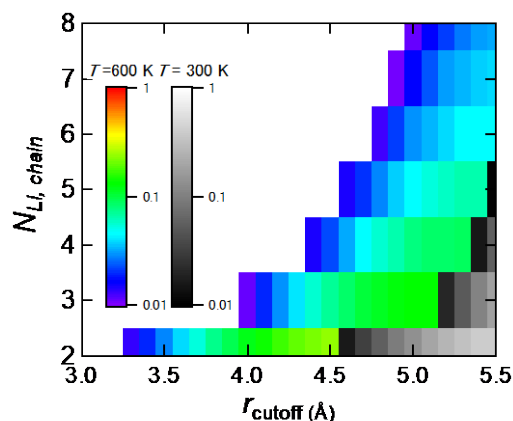


Fig. 2 Time-averaged probability density distribution of the number of Li ions in bonded chain determined from graph theory. The horizontal axis is the cut-off radius within which Li ions are regarded as bonded. The distribution for each cut-off radius is normalized so that the sum of the distributions for each cut-off radius is 1.

## References

[1] R. Sato et. al. *J. Chem. Phys.*, 158 (2023) 144116.

[2] E. Santos, R. Sato, et. al., *Chem. Mater.*, 35 (2023) 5996.

[3] F. Yang, E. Santos, X. Jia, R. Sato, K. Kisu, Y. Hashimoto, S. Orimo. H. Li, *Nano Mater. Sci.*, in press.

# Study of ground states and excitations in frustrated quantum magnets using MPS-based simulations

Matthias GOHLKE

*Theory of Quantum Matter Unit, Okinawa Institute of Science and Technology*
*1919-1 Tancha, Onna-son, Okinawa 904-0495*

Competing interactions—or frustration—between the constituents of a many-body system have proven to be an origin of exotic phases of matter. A famous example in this context are quantum spin liquids (QSL), that do not exhibit conventional magnetic order of spin-dipolar moments, but rather are defined by emergent gauge fields, fractionalized excitations, and topological order. A topical example in this context are Kitaev-like frustrated magnets, that exhibit a bond-dependent spin-exchange resulting in exchange frustration and, for certain choices of parameters, can result in a QSL ground state. Part of the computational resources provided by ISSP has been used to study the related anisotropic Kitaev-$\Gamma$ model [see (I)].

On the other hand, ordering of higher moments like spin-quadrupoles may occur as well. Unlike spin-dipolar order, spin-quadrupolar order is defined by a director—an arrow without a head—in close analogy to the rods of nematic order and liquid crystals. Thus, spin-quadrupolar order is also named quantum spin nematic (QSN). Part of the resources have been used to study the QSN phase stabilizing in a frustrated ferromagnet with external magnetic field [see (II)].

**(I) Extended QSL in an Anisotropic Kitaev-$\Gamma$ Model.** The characterization of quantum spin liquid phases in Kitaev materials has been a subject of intensive studies over the recent years. Most theoretical studies have focused on isotropic coupling strength in an attempt to simplify the problem. We, instead, have focused on an extended spin-1/2 Kitaev-$\Gamma$ model on a honeycomb lattice with an additional tuning parameter that controls the coupling strength on one of the bonds [1], allowing us to connect the limit of isolated Kitaev-$\Gamma$ chains, which is known to exhibit an emergent $SU(2)_1$ Tomonaga-Luttinger liquid (TLL) [2], to the two-dimensional model. We find that the critical properties of the TLL persist for finite inter-chain coupling, and a quantum paramagnetic phase which we call the proximate TLL stabilizes in analogy to *sliding Luttinger liquids*. This proximate TLL differs from the Kitaev spin liquid [1] in that $Z_2$ fluxes are not conserved.

Moreover, we have investigated the region of parameter space near the antiferromagnetic Kitaev coupling, were we find several long-range magnetically ordered phases [3], see Fig. 1.

**(II) QSN in a Spin-$\frac{1}{2}$ Frustrated Ferromagnet.** Here, we focus on a quantum magnet with spin-$\frac{1}{2}$ degrees of freedom. Such magnets can only exhibit a QSN states if two spin-$\frac{1}{2}$ are combined into an effective spin-1 [4].

Experimentally, the nature of such a ground state is intrinsically difficult to verify, due to the lack of probes that couple directly to the spin-quadrupole moments. Instead, it is necessary to examine the dynamics of a QSN: A continuous symmetry for the director of a spin-quadrupole remains, that give rise to a gapless Goldstone mode [6].

(a) $\phi/\pi = 0.92$, 90° NC

(b) $\phi/\pi = 0.94$, cLRO$_1$, 2- & 6-site

(c) $\phi/\pi = 0.96$, cLRO$_2$, 4- & 12-site
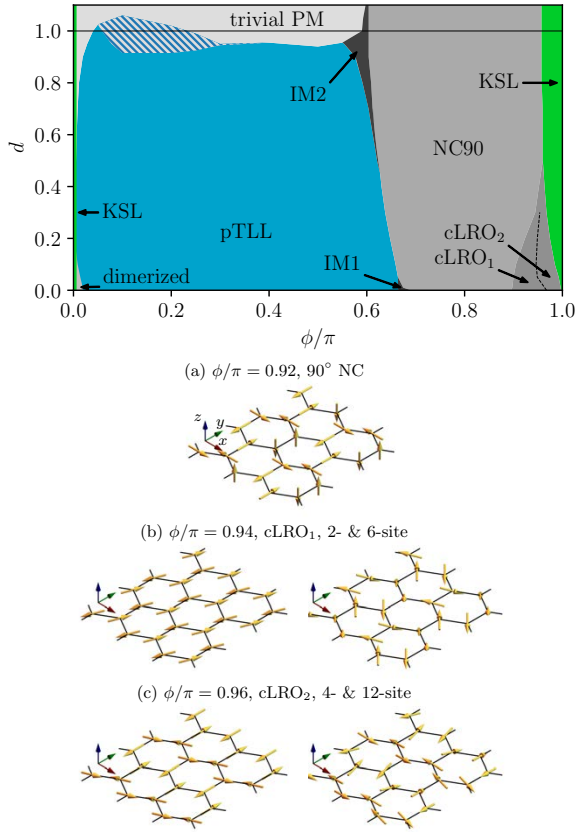
Figure 1: Extended phase diagram of the anisotropic KΓ model with illustrations of the long range magnetically ordered phases.

Here, we study the square-lattice frustrated $J_1$-$K$ model [4], with dominant ferromagnetic Heisenberg exchange $J_1$ between nearest neighbor spins, cyclic ring-exchange $K$ around squares, and $h_z$ the Zeeman coupling to a magnetic field along the $z$-axis. Using iDMRG and the matrix product states (MPS) framework as well as a recently developed exact diagonalization (ED) method near saturation [5], we confirm the existence of the QSN phase in an extended range of $K/|J_1|$. Overall we find a good agreement between high-field ED on symmetric clusters and iDMRG. The QSN phase is sandwiched between high-field polarized and 4-sublattice AF phase. Additional phases (Neél, vector-chiral) occur for large $K$.

As reported previously, we have identified a gapless mode at an incommensurate wave vector coinciding with a set of eigenvalues in the MPS transfer matrix (TM) spectrum. Consequently, we have been able to study its behaviour with respect to an external magnetic field, system size and geometry, without having to invoke costly time-evolution simulations. Momentum information is contained through the complex phase of the TM eigenvalues, and momentum along the circumference being a well defined quantum number as long as translation symmetry remains. In essence, we find linear dependence of the wave vector with the magnetization, but also a dependence on the cylinder circumference. The latter makes an extrapolation to the 2D thermodynamic limit difficult. Consequently, we are trying to elucidate its physical origin. A publication is currently in preparation [7].

All MPS-related simulations have been carried out using TenPy [8]. TenPy makes use of Cython and calls heavily optimized Lapack and Blas routines matrix operations, e.g. singular value decomposition.

# References

[1] M. Gohlke, J. C. Pelayo, T. Suzuki, arXiv:2212.11000 (2022). *To be published as a Letter in PRB. See also report by T. Suzuki.*

[2] Yang et al. Phys. Rev. Lett. **124**, 147205 (2020).

[3] M. Gohlke, J. C. Pelayo, T. Suzuki, *in preparation.*

[4] A. Andreev and I. Grishchuk, Sov. Phys. JETP **60** (1984) 267.

[5] H. Ueda, S. Yunoki, and T. Shimokawa, Comp. Phys. Comm. **277** (2022) 108369.

[6] R. Shindou, S. Yunoki, and T. Momoi, Phys. Rev. B **87**, (2013) 054429.

[7] M. Gohlke, T. Shimokawa, J. Sonnenschein, N. Shannon, *in preparation.*

[8] J. Hauschild, and F. Pollmann, SciPost Phys. Lect. Notes 5 (2018).

# Towards understanding ground-state properties of multilayered superconductors using the variational Monte Carlo method

Ryui KANEKO

*Research Institute for Science and Engineering, Waseda University*
*Shinjuku, Tokyo 169-8555, Japan*

It is indispensable to understand the trend of layered cuprate superconductors through studying their effective Hamiltonians derived by first-principles calculations [1]. In particular, single-layer models focusing on each $CuO_2$ layer have been obtained for $CaCuO_2$, $Bi_2Sr_2CuO_6$ (Bi2201), $Bi_2Sr_2CaCu2O_8$ (Bi2212), and $HgBa_2CuO_4$, and their superconducting correlations that depend on doping levels have been extensively calculated [2] using the many-variable variational Monte Carlo method [3]. We previously found that it is crucial to enhance the on-site Coulomb repulsion over the nearest-neighbor hopping substantially and to sufficiently reduce the long-range Coulomb repulsion compared to the on-site repulsion for the purpose of increasing the superconducting order parameter, which correlates with the superconducting transition temperature [2].

The number of layers should also contributes to the stability of the superconducting state. However, in the analysis regarding the number of layers, the effective Hamiltonians include many long-ranged parameters that hinder the ground-state search. Thus, the effects of layers still need to be thoroughly verified using highly accurate numerical methods. Typically, in quasi-2D systems with intense interlayer hopping and interactions, an increase in spatial dimensionality is known to enhance magnetic ordering in general. The effective model under such conditions differs from a simple single-layer model. Whether the superconducting state can prevail over this magnetic state in a global parameter space is a crucial question. For this purpose, it is essential to solve models with two or more layers with high accuracy. So far, it has only been confirmed that the superconducting order parameters are comparable between single-layer and two-layer effective Hamiltonians at specific doping concentrations for Bi2212 [2].

In this study, using the many-variable variational Monte Carlo method [3], we investigate the ab initio three-layer effective Hamiltonian derived in the first-principles calculations [4] corresponding to $HgBa_2Ca_2Cu_3O_{8+\delta}$ (Hg1223), which has the highest transition temperature at ambient pressure among any mercury-based cuprate superconductors currently available. We first estimate the difference in chemical potential between the inner and outer layers, which reproduces the orbital filling of the GW calculation, at 20% hole doping.

Calculations regarding whether the superconducting state can prevail over magnetic and charge ordered states with long-period structure [5] are under way.

## Acknowledgement

# References

[1] J.-B. Morée, M. Hirayama, M. T. Schmid, Y. Yamaji, and M. Imada, Phys. Rev. B **106**, 235150 (2022).

[2] M. T. Schmid, J.-B. Morée, R. Kaneko, Y. Yamaji, and M. Imada, Phys. Rev. X **13**, 041036 (2023).

[3] T. Misawa, S. Morita, K. Yoshimi, M. Kawamura, Y. Motoyama, K. Ido, T. Ohgoe, M. Imada, T. Kato, Comp. Phys. Commun., **235**, 447 (2019).

[4] J.-B. Morée, Y. Yamaji, and M. Imada, arXiv:2312.16402.

[5] K. Ido, T. Ohgoe, M. Imada, Phys. Rev. B **97**, 045138 (2018).

# Quantum entanglement dynamics in free boson systems by computing the matrix permanent

Ryui KANEKO

*Research Institute for Science and Engineering, Waseda University*
*Shinjuku, Tokyo 169-8555, Japan*

The time evolution of entanglement has been measured in experiments with ultracold atomic systems in optical lattices [1, 2], and it is crucial to verify how well numerical simulations on classical computers can reproduce it. However, numerical simulations of long-term evolution in soft-core bosonic systems are incredibly challenging, with conventional methods based on exact diagonalization or matrix product states being limited to dozens of sites for calculating entanglement dynamics [3]. Recently, we provided an analytical solution for the time evolution of Renyi entanglement entropy after quenching to a noninteracting bosonic system starting from an insulating state. Numerical evaluation of this entanglement entropy requires computing the permanent of matrices, which increases exponentially with the matrix size $2n$ or twice the number of particles $n$, namely, $O(2n \times 2^{2n})$ [4]. We numerically demonstrated that one could compute entanglement dynamics for systems of about 50 sites at half filling within realistic timeframes [4].

In this study, we focus on the unexplored area of spatial 2D systems, which would help us understand how the propagation of quantum information changes with dimensionality. As a simple example of a 2D system, we consider the Bose-Hubbard model on a square lattice. Starting from a charge-density-wave insulating product state at half filling, which is realized for sufficiently large interactions, we compute the time evolution of the Renyi entanglement $S_2(t)$ of the states at each time $t$
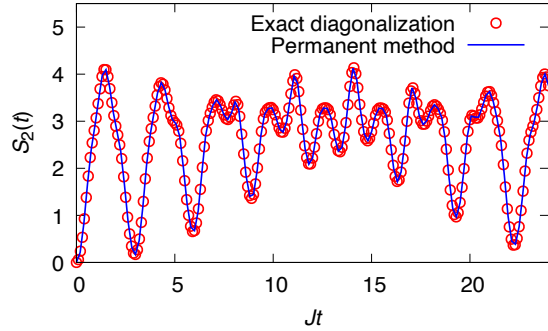


Figure 1: Time evolution of Renyi entanglement for $4 \times 3$ sites with open boundary conditions. The initial state is chosen as the staggered charge-density-wave state $(010101 \cdots$ type) at half filling. We calculate entanglement entropy when the system is divided into two regions of $2 \times 3$ sites.

after quenching the system to $U = 0$, where $U$ is the interaction parameter. The formulas

$$S_2(t) = -\ln \mathrm{perm} A(t), \qquad (1)$$

$$A(t) = \begin{pmatrix} Z(t) & I - Z(t) \\ I - Z(t) & Z(t) \end{pmatrix} \qquad (2)$$

give the Renyi entanglement [4], where $I$ is the identity matrix and $Z(t)$ is a matrix constructed from the time-dependent single-particle correlation function obtained from the noninteracting Hamiltonian and the initial insulating product state. While obtaining $Z(t)$ from the diagonalization of matrices written in quadratic form is easy, the computational cost of $\mathrm{perm} A(t)$ is exponentially high. Considering the price of computing the permanent from

previous studies [4–7], it is likely that calculations for about $7 \times 7$ sites are feasible.

$S_2(t)$ does not need to be sequentially computed as a function of time, and it can be calculated in parallel for any time $t$. One can also parallelize the computation of the permanent itself. As a benchmark, we computed $S_2(t)$ quenched from the staggered charge-density-wave state $(010101 \cdots$ type) at half filling for small systems $(4 \times 3$ sites) with time steps of $\Delta Jt = 3/16$ ($J$: hopping) and for $Jt \in [0, 24]$ (see Fig. 1), confirming good agreement with exact diagonalization results. Computing $S_2(t)$ for larger systems is a future task.

## References

[1] R. Islam et al., Nature **528**, 77 (2015).

[2] A. M. Kaufman et al., Science **353**, 794 (2016).

[3] S. Goto and I. Danshita, Phys. Rev. B **99**, 054307 (2019).

[4] D. Kagamihara et al., Phys. Rev. A **107**, 033305 (2023).

[5] A. Neville et al., Nat. Phys. **13**, 1153 (2017).

[6] J. Wu et al., Natl. Sci. Rev. **5**, 715 (2018).

[7] P.-H. Lundow and K. Markström, J. Comput. Phys. **455**, 110990 (2022).

# Cell Division Plane Prediction

Yuuki Matsushtia, Katsuyoshi Matsushita, Koichi Fujimoto
*Graduate School of Integrated Sciences for Life, Hiroshima University*
*Kagamiyama, Higashi-Hiroshima, Hiroshima 739-0046*

Cell division is one of the indispensable cellular properties in the developmental process. In particular, plant cells cannot move, and therefore, the direction of the cell division determines the plant shape. One of the simple determination principles for cell division is Errera's rule [1]. The rule states that the division plane forms likely a soap film. This rule indicates that the division plane takes the smallest-area curved plane in the given shape of a mother cell under a constraint of daughter cell volumes. Based on this rule, the physical model of phase boundary under volume constraints of two phases can simulate this rule. The simulation is analytically solvable in the case of simple mother-cell shapes[2, 3], but the analytical solution hardly applies to realistic mother-cell shapes. To solve this hardness of analysis, a numerical simulator has been recently developed based on the phase field model and applied to various predictions of plant developments [4].

The calculation cost of the phase field model is very high and, therefore, can only accept cases with a few cells. A simpler calculation model is necessary for the prediction of long-time plant development yielding a large number of cells. To overcome this issue, Moukhtar *et al.* [6] used the cellular Potts model [5]. Using the Monte Carlo method, the model relatively reduces calculation costs by optimizing energy. In this model, the failure of orientation determination has been reported because of the lattice anisotropy effect. As an improvement to avoid this failure, a modification using the Hamiltonian term of the Crofton formula of interface area was proposed instead of the Potts Hamiltonian. The calculation introduces a complicated evaluation in the area of the division plane. Therefore, the model is inefficient for extending the cases, including the cell polarity or cytoskeleton configuration dependence. For further development of the division plane prediction, we should consider a more straightforward way of this method.

To reduce the anisotropy effect of this model, we considered the second and third neighbor interactions of the cellular Potts model. The long-range interaction has been reported to reduce the effect [5]. We developed the simulator for these long-range interactions and sufficiently succeeded in determining the division planes in simple shapes. We further applied the simulator to predict the division plane of the embryo of the Arabidopsis. We collaborated with biological experimentalists and obtained realistic mother cell shapes. We confirmed the correctness of the prediction using the simulator and now attempt to apply this method to various experimental conditions.

## References

[1] L. Errera, Botanische Centralblatt **34**, 395, (1888).

[2] S. Besson J. Dumais, Proc. Natl. Acad. Sci. USA **108**, 6294 (2010).

[3] N. Kamamoto, T. Tano, K. Fujimoto, M. Shimamura, J. Plant Res. **134**, 457 (2021).

[4] C. Ishikawa, *et al.*, Proc. Natl. Acad. Sci. USA **120**, e2210632120 (2023).

[5] F. Graner and J. Glazier, Phys. Rev. Lett. **69**, 2013 (1992).

[6] J. Moukhtar, *et al.* PLoS Comput Biol **15**, e1006771 (2019).

# Calculation of ordered structures, dynamics and optical properties of soft materials

Hiroki MATSUKIYO  and Jun-ichi FUKUDA

*Department of Physics, Kyushu University, Motooka 744, Nishi-ku, Fukuoka 819-0395*

This year we have studied the dynamics of active matter systems, particularly focusing on the behavior of polar active fluids under geometrical confinements [1]. The behavior of polar active fluids can be described by a continuum equation, the Toner-Tu-Swift-Hohenberg (TTSH) equation. Several previous studies on the simulation based on the TTSH equation employed the non-slip boundary condition and did not describe the "edge current" (the unidirectional flow along the boundary), which had been observed in experiments. In ref. [1], we have proposed a new numerical method to calculate the TTSH equation under a slip boundary condition and successfully realized the edge current, see FIG.1. Furthermore, we have discovered the temporal oscillation of the edge current direction. To investigate the relation between the frequency of the oscillation and the parameters in the TTSH equation, we have performed simulations for many sets of parameter values, see FIG.2. The large number of threads of System B, Ohtaka, made it possible for us to perform the simulations in parallel for a large number of combinations of parameter values.

## References

[1] Hiroki Matsukiyo and Jun-ichi Fukuda, arXiv:2312.08788.  (to be published in Physical Review E)
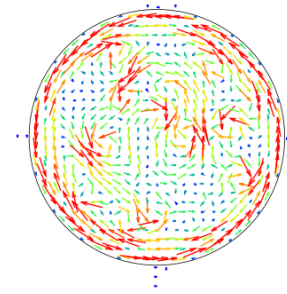
FIG.1: A typical snapshot of the velocity filed.
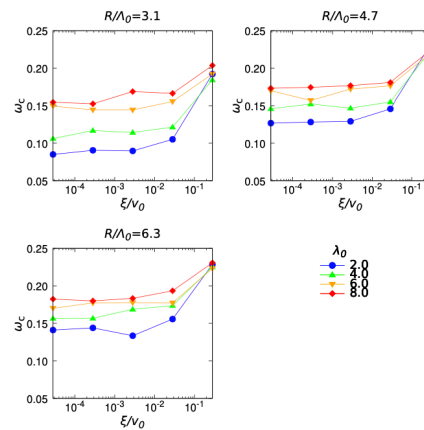


FIG.2: The relation between the characteristic frequency $\omega_c$ of the edge current oscillation and the parameters in the TTSH equation ($\xi$ is the drag coefficient, $\lambda_0$ is the advection strength and $R$ is the radius of the circular domain).

# Dynamics of monitored quantum systems with symmetry

Yohei FUJI

*Department of Applied Physics, University of Tokyo, Tokyo 113-8656*

Many-body quantum states subject to frequent measurements undergo a measurement-induced phase transition, at which various critical scaling properties described by conformal field theory emerge [1, 2]. Such phase transitions typically occur between a volume-law entangled state, dominated by unitary dynamics, and an area-law entangled state, dominated by measurements. When the dynamics preserves some symmetry, measurement-induced transitions can also occur between area-law entangled states, in closed analogy to equilibrium phase transitions between ordered and disordered phases. However, the role of symmetry for universal properties at measurement-induced phase transitions is still largely unexplored.

In this study, we consider measurement-induced phase transitions in (2+1)-dimensional quantum circuits consisting of competing projective measurements. Measured operators in the circuits constitute a (2+1)-dimensional quantum Ising model and its plaquette extensions, as shown in Fig. 1, and thus preserve a global or subsystem $\mathbb{Z}_2$ symmetry. Since these circuits are written solely in terms of the measurements of Pauli operators, an efficient numerical algorithm based on the stabilizer formalism is available to access systems with $O(10^3)$ spins. We found that a measurement-induced transition between area-law entangled states takes place when the measurements of bond ($XX$) or plaquette ($XXXX$) operators competes with those of single-site Pauli $Z$ operators. While
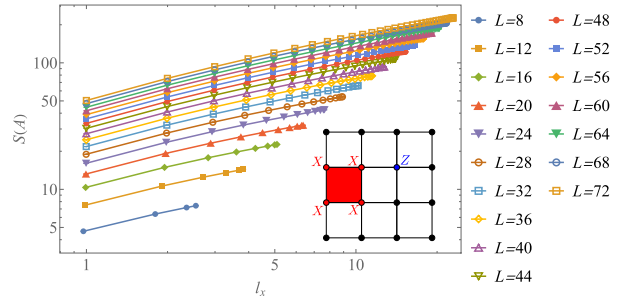


Figure 1: Entanglement entropy $S(A)$ at the measurement-induced transition in the plaquette Ising circuit. We consider an $L \times L$ system on a torus and its bipartition into $l_x \times L$ and $(L - l_x) \times L$ cylindrical subsystems.

the quantum Ising circuit exhibits critical properties expected for a three-dimensional percolation transition as previously reported, the plaquette Ising circuit shows somewhat unusual scaling properties as exemplified in algebraic growth of the entanglement entropy. We are currently trying to understand the role of the subsystem $\mathbb{Z}_2$ symmetry to those critical properties.

# References

[1] A. C. Potter and R. Vasseur, Entanglement Dynamics in Hybrid Quantum Circuits, arXiv:2111.08018.

[2] M. P. A. Fisher, V. Khemani, A. Nahum, and S. Vijay, Random Quantum Circuits, Annu. Rev. Condens. Matter Phys. **14**, 335 (2023).

# A Large-Scale Molecular Dynamics Simulation Study on the Shape of an Ice Crystal Grown from Water Including Air Molecules

Hiroki NADA

*Faculty of Engineering, Tottori University, 4-101 Koyama-Minami, Tottori 680-8552*

Elucidating the growth kinetics of ice from water in the presence of air molecules is of importance for understanding ice particle formation in nature. In this project, a molecular dynamics (MD) simulation was conducted to investigate the shape of an ice crystal grown from water in which air molecules were dissolved.

The simulation was performed using a system in which an ice crystal grew freely in all directions perpendicular to the crystal's *c*-axis [1]. The system used contained a cylindrical ice crystal at the center, and the remainder of the system corresponded to liquid water including air molecules. The numbers of $H_2O$ and air molecules in the system were 17540 and 100, respectively. In this study, we specially focused on the effects of $N_2$ and $CO_2$ molecules on the growth shape of an ice crystal. To elucidate those effects, for comparison, the simulation was also performed for a pure $H_2O$ system.

A modified version of six-site model of $H_2O$ [2] was used to estimate the intermolecular interaction between a pair of $H_2O$ molecules. Temperature and pressure were maintained at 265 K and 1 atm, respectively. TraPPE $N_2$ and $CO_2$ models were used to estimate the interaction acting on air molecules [3]. The MD simulation was carried out with DL_POLY 2.20, using System B of ISSP Supercomputer Center.

The effect of air molecules on the growth rate of the ice crystal was different between $N_2$ and $CO_2$ molecules. $N_2$ molecules bound to the interface between the growing ice crystal and water and lowered the growth rate of the ice crystal. However, $CO_2$ molecules did not stably bind to the interface and, hence, did not significantly change the growth rate. In addition, the growth shape of the ice crystal was also different between $N_2$ and $CO_2$ molecules.

# References

[1] H. Nada: Cryst. Growth. Des. **11** (2011) 3130.

[2] H. Nada: J. Chem. Phys. **145** (2016) 244706.

[3] J. J. Potoff and J. I. Siepmann: AIChE J. **47** (2001) 1676.

# A Large-Scale Metadynamics Simulation Study on the Binding Conformations of Ionic Polymers at a Geometrically Rough Surface of Calcium Carbonate Crystal

Hiroki NADA

*Faculty of Engineering, Tottori University, 4-101 Koyama-Minami, Tottori 680-8552*

The control of calcium carbonate crystal growth by additives is essential to biomineralization, scale inhibition, and materials technology. In this project, molecular dynamics (MD) simulations based on the metadynamics (MTD) method (hereafter, MTD simulation) were conducted to elucidate the stable binding conformations of a polymaleic acid (PMA$_n$, $\{(CO_2CHCHCO_2)^{2-}\}_n$, n=5–10) and a polyacrylic acid (PAA$_n$, $\{(CH_2CHCO_2)^-\}_n$, n=10–20) at a calcite (104) surface having a geometrically rough structure, which appears during calcite growth.

The simulation system was a rectangular parallelepiped in which a calcite slab was placed at its center such that its (104) planes, at which steps having kinks at their edges were formed, were perpendicular to the *z*-axis [1]. A liquid water phase containing the additive was placed at one of the two (104) planes. Following our previous studies [1, 2], the interactions within calcite were estimated with a model proposed by Raiteri et al., and the potential parameters for were determined using the general AMBER force field. The interaction between pairs of water molecules was estimated using the TIP3P model. The MTD simulation was carried out with DL_POLY 2.20, in which PLUMED 1.3 was implemented to permit combination with the MTD method, using System C of ISSP Supercomputer Center.

For all the additives examined, a free energy surface (FES) obtained using the x- and y-components of the distance between two C atoms at the sides of the additive's main chain as collective variables indicated several local minima, suggesting the existence of several different stable binding conformations. For all the stable binding conformations emerged, the main chain of the additive was distorted, and most of the carboxyl O atoms were exposed to the water phase. The binding stability was higher for PMA$_n$ than for PAA$_n$, when they had the same number of carboxyl groups.

# References

[1] H. Nada: J. Phys. Chem. C **118** (2014) 14335.

[2] H. Nada: Langmuir **14** (1996) 136.

# Structural formation of non-spherical colloidal particles

Takamichi TERAO

*Department of Electrical, Electronic and Computer Engineering,*

*Gifu University, Yanagido 1-1, Gifu, 501-1132*

In colloid science, theoretical studies have focused on patchy particles, exploring how their behavior is influenced by orientation-dependent attractions [1]. These studies characterize systems of charged patchy particles, which feature a heterogeneous surface charge distribution, by the interplay between electrostatic attraction and repulsion. However, systematic research on non-spherical charged patchy particles is lacking, and several unresolved issues persist.

In this study, a computer modeling is employed to treat non-spherical charged patchy particles in molecular dynamics simulations. The model arranges several small particles with both positive and negative charges on the surface of a rotating ellipsoid, treating the entire assembly as a single patchy particle. These small particles are categorized into three groups: those at both ends of the long axis are assigned a negative charge, while the remaining particles receive a positive charge. Although this method of modeling patchy particles as a set of small particles is computationally demanding, it allows for the accurate replication of a wide range of patchy particle properties.

Molecular dynamics simulations were performed on a system of non-spherical charged patchy particles confined between parallel planes. Figure 1 displays a typical snapshot of the system, with the areas representing the patchy particles highlighted in white. Under these conditions, the patchy particles were observed to aggregate randomly. It was also confirmed that various structures of non-spherical patchy particles appear in different conditions.
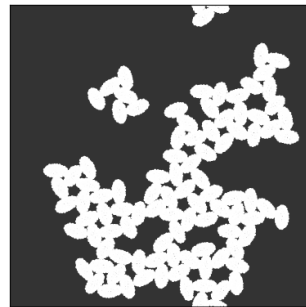


Fig. 1: Snapshot of non-spherical patchy particles

## References

[1] E. Bianchi, J. Largo, P. Tartaglia, E. Zaccarelli, and F. Sciortino, Phys. Rev. Lett. **97**, 168301 (2006).

# Comparison of superconducting properties in quasicrystals and approximant crystals

Nayuta TAKEMORI

*Department of Physics, Graduate School of Science, Osaka University*
*1-1 Machikaneyama,Toyonaka,Osaka 560-0043*

Quasicrystals are characterized by an unusual crystal structure that lacks translational symmetry and displays unconventional point group symmetry, such as 5-fold rotational symmetry. This has implications for superconductivity in materials with such structures, which has garnered significant attention recently. Specifically, non-BCS-type s-wave weak coupling superconductivity in quasicrystals, predicted in 2017, involves Cooper pairs with finite center-of-mass momentum, representing a novel form of exotic superconductivity [1]. In 2018, bulk superconductivity was experimentally confirmed in Al-Mg-Zn quasicrystals and their 1/1 approximants. The temperature dependence of the electronic specific heat in these materials was found to be consistent with the theoretical predictions, although the jump in specific heat is about 10-20% smaller than expected from BCS theory due to the absence of a Fermi surface and coherence peaks [2].

In this work, we investigate the results of a theoretical analysis of the attractive Hubbard model using Bogoliubov-de Gennes mean-field theory. The previous works [1, 2] suggests that quantitative differences in specific heat jumps may exist between quasicrystals and approximants with periodic approximation. However, it remained unknown to what extent the specific heat jump in approximants differs from that in quasicrystals. Motivated by this, we also investigate Penrose approximants and compare their superconducting properties with those of quasicrystals and regular periodic systems. We demonstrate that the peculiar superconducting properties of quasiperiodic systems do not appear in the case of approximants which exhibit locally similar structures to those of quasicrystals (Table 1).

# References

[1] Shiro Sakai, Nayuta Takemori, Akihisa Koga, and Ryotaro Arita. Superconductivity on a quasiperiodic lattice: Extended-to-localized crossover of cooper pairs. *Phys. Rev. B*, 95:024509, Jan 2017.

[2] Nayuta Takemori, Ryotaro Arita, and Shiro Sakai. Physical properties of weak-coupling quasiperiodic superconductors. *Phys. Rev. B*, 102:115108, Sep 2020.

[3] Michael Tinkham. *Introduction to superconductivity*. Courier Corporation, 1996.

| | Penrose (OBC) | | | | Socolar (OBC) | Square (PBC) | | Penrose approx (PBC) | | BCS |
|---|---|---|---|---|---|---|---|---|---|---|
| | 1591 | 4181 | 11006 | ext | 5289 | 2500 | 10000 | 1/1 | 4/3–3/2 | |
| $\frac{2E_g^0}{T_c}$ | 3.35 | 3.38 | 3.38 | 3.38 | 3.37 | 3.46 | 3.45 | 3.42 | 3.45 | 3.52 |
| $A_1$ | 1.61 | 1.63 | 1.69 | 1.70 | 1.66 | 1.70 | 1.70 | 1.68 | 1.67 | 1.74 |
| $\frac{\Delta C}{C_{\text{en}}}$ | 1.13 | 1.21 | 1.21 | 1.21 | 1.19 | 1.40 | 1.39 | 1.41 | 1.45 | 1.43 |

Table 1: The ratio of the superconducting gap at zero temperature to the critical temperature (top), a coefficient in the temperature dependence of the superconducting gap near the critical temperature (middle), and the jump of the specific heat (bottom) obtained in Penrose tiling of 1591, 4181 and 11006 sites, as well as its extrapolated value and those for square lattice of 2500 and 10000 sites. Universal values in the conventional continuum BCS theory [3] are added in the rightmost column.

# Numerical study of dynamical structure factors based on spinon operator representation of Heisenberg antiferromagnets

Yoshiyuki Fukumoto

*Department of Physics and Astronomy, Faculty of Science and Technology,*
*Tokyo University of Science, 2641 Yamazaki, Noda, Chiba 278-8510*

In recent years, a lot of interests have been focused on low-energy excitations of frustrated magnetically ordered systems [1]. The trigger was a high-resolution neutron scattering experiment on the $S = 1/2$ triangular-lattice system $Ba_3CoSb_2O_9$ [2], which clearly observes a continuous band that is thought to be a composite excitation of spinons in addition to magnon excitations. The magnon spectrum is significantly deformed from the calculation results of the linear spin-wave theory. It looks as if it is being pushed by the continuous band.

In order to understand this experimental observation, Zhang *et al.* performed theoretical calculations using the fermion representation of the spin operator, for which each site is constrained to have one fermion. They made a mean-field approximation corresponding to the equal-amplitude resonating valence bond (RVB) state, and construct a single-particle state using the mean-field Hamiltonian under a staggered magnetic field that stabilizes the magnetic 120-degree structure. A ground state and particle-hole excited states are created from these one-particle states. They argued that the structure of the spinon continuum is closely related to the roton minimum of the magnon spectrum, and also discovered an amplitude mode consisting of two bound spinons that cannot be captured by the spin wave approximation. However, the constraint condition for the fermion representation is treated within the RPA approximation. Thus, it is desired to perform calculations that accurately handle the constraint.

In this study, we strictly handle the constraint conditions and calculate the ground state and the dynamic structure factors, with taking into account the particle-hole excited states, by using the variational Monte Carlo (VMC) method, where we have introduced a method called reweighting to use a common sample to calculate all matrix elements [4].

The ground state calculations were performed for a system of up to 288 sites, and the energy at the thermodynamic limit was estimated by extrapolating the system size. Our result of ground state per site is $E/JN = -0.5407(2)$. Although our result is lower than previous VMC studies, $E/JN = -0.532(1)$ [5], and the spin-wave approximation, $E/JN = -0.538(2)$, but it is higher than the result of the series expansion method, $E/JN = -0.5502(4)$ [6], which shows that there is room for further improvement in variational functions. It is desirable to introduce longer valence bonds into the variational function. We also calculated the dynamic structure factors for the 36-site system and compared them with the experimental results for $Ba_3CoSb_2O_9$ and the calculation results by Zhang *et al*, and we will perform calculations on a larger system next year.

[1] B. D. Piazza *et al.*, Nat. Phys. 11, 62, 2015.
[2] S. Ito *et al.*, Nat. Commun. 8, 235, 2017.
[3] C. Zhang *et al.*, PRB 102, 075108, 2020.
[4] T. Li *et al.*, PRB 81, 214509, 2010.
[5] C. Weber *et al.*, PRB 73, 014519, 2006.
[6] W. Zheng *et al.*, PRB 74, 224420, 2006.

# Impact of direction of the Dzyaloshinskii-Moriya vector on the magnon dispersion of the q=0 state in kagome-lattice systems

Yoshiyuki Fukumoto

*Department of Physics and Astronomy, Faculty of Science and Technology,*
*Tokyo University of Science, 2641 Yamazaki, Noda, Chiba 278-8510*

A magnon is an elementary excitation from a magnetically ordered state. The linear spin wave (LSW) theory is a standard calculation method of magnon dispersion relations. However, through research using neutron scattering experiments of $S = 1/2$ Heisenberg antiferromagnets on triangular lattices and kagome lattices [1-3], it has been found that the LSW results require very large correction factors for $S = 1/2$ frustrated systems [4,5].

Kogure *et al.* used the series expansion method based on the linked-cluster algorithm [6] to study the magnon dispersion relation of the kagome system $Cs_2Cu_3SnF_{12}$ with $q = 0$ order [5]. Their model Hamiltonian consisted of the nearest-neighbor exchange and Dzalosinsky-Moriya (DM) interactions, where the direction of the DM vector was perpendicular to the kagome plane. As a result, it was revealed that the band width of the magnon spectrum in the series expansion is less than half of the LSW, and its shape is also significantly changed. It was also revealed that the correction for the LSW is larger for the kagome lattice than for the triangular lattice. As the magnitude of the DM vector is chosen as $0.12J$, where $J = 20.7$ meV is the exchange parameter, the magnon spectrum by the series expansion can be compared with the experimental result for $Cs_2Cu_3SnF_{12}$. However, there remain quantitative discrepancies: one of them is that the experimental value of the excitation gap at the M point is 8.3 meV, whereas the calculation gives a smaller value of 6.2 meV.

In this study, we consider the case where the direction of the DM vector is tilted from the kagome plane, and investigate how this affects the calculated results of the magnon spectrum. Then, the interaction matrix elements become to be complex numbers, so we need to rewrite the calculation program accordingly. In particular, the matrix $S$, in a transformation matrix $e^S$ used to construct the effective Hamiltonian, changes from a real antisymmetric matrix to a skew-Hermitian matrix. We confirmed that our program correctly satisfies the conditions for the order in which cluster weights are generated [6].

As a result of calculations up to seventh order, it was found that the DM vector component parallel to the kagome plane has almost no effect on the excitation energy around the M point. Another interaction that should be considered is the second-neighbor exchange interaction $J_2$, which was estimated to be $J_2 \simeq -0.1J$ in a previous study [2]. This ferromagnetic second-neighbor interaction has a frustrating effect on the $q = 0$ state. Next year, we plan to investigate the influence of ferromagnetic $J_2$ on magnon dispersion. Since the number of clusters increases significantly with the introduction of second-neighbor interactions, more computational resources are required.

[1] S. Ito *et al.*, Nat. Commun. 8, 235, 2017.
[2] T. Ono *et al.*, JPSJ 83, 043701, 2014.
[3] M. Saito *et al.*, PRB 105, 064424, 2022.
[4] W. Zheng *et al.*, PRB 74, 224420, 2006.
[5] S. Kogure *et al.*, JPSJ 92, 113703, 2023.
[6] M. P. Gelfand *et al.*, JSP 59, 1093, 1990.

# Ground-State Phase Diagram of an Anisotropic $S=3/2$ Chain: Triatic TLL and Nematic TLL Phases

Takashi Tonegawa

*Kobe Univ., Osaka Metropolitan Univ., and Univ. of Hyogo*

The purpose of this report is to explore the ground-state phase diagram of an anisotropic $S=3/2$ chain system by using mainly numerical methods. We express the Hamiltonian which describes this system as

$$\mathcal{H} = \sum_{j=1}^{N} \left\{ S_j^x S_{j+1}^x + S_j^y S_{j+1}^y + \Delta S_j^z S_{j+1}^z + D\left(S_j^z\right)^2 \right\},$$
(1)

where $S_j^\alpha$ ($\alpha = x,\,y,\,z$) is the $\alpha$-component of the $S=3/2$ operator at the $j$-th site; $\Delta$ and $D$ are, respectively, the $XXZ$-type anisotropy parameter of the nearest-neighbor interactions and the on-site anisotropy parameter; $N$, being assumed to be even, is the total number of spins in the system. Hereafter, we denote the $z$-component of the total spin by $M\left(=\sum_{j=1}^{N} S_j^z\right)$, where $M=0,\,\pm1,\,\pm2,\,\cdots,\,\pm2N/3$.

In this report we numerically determine the ground-state phase diagram as accurately as possible. Estimating the phase boundary lines, we analyze the energy eigenvalues of the Hamiltonian $\mathcal{H}$, which are calculated by the use of the exact-diagonalization (ED) method. The resultant phase diagram is shown in Fig. 1. In spite of the present simple system, this phase diagram is rather rich and consists of five kinds of phases; these are the triatic Tomonaga-Luttinger liquid (tTLL), nematic Tomonaga-Luttinger liquid (nTLL), $XY1$ (XY1), Néel (N), and ferromagnetic (F) phases.

Let us now discuss how to numerically determine the phase boundary lines shown in Fig. 1. We denote, respectively, by $E_0(N,M)$ and $E_1(N,M)$, the lowest and second-lowest energy eigenvalues of the Hamiltonian $\mathcal{H}$ under the periodic boundary condition ($S_{N+1}^\alpha \equiv S_1^\alpha$) within the subspace of $N$ and $M$. We have numerically calculated these energies for finite-size systems with up to $N=14$ spins by using the ED method. The ground-state energy of the finite-$N$ system is given by $E_0(N,3N/2)$ in the F region and by $E_0(N,0)$ in the other regions. We introduce here the following energy differences,

$$\Delta_{00}(N) = E_1(N,0) - E_0(N,0),$$
(2)
$$\Delta_{10}(N) = E_0(N,1) - E_0(N,0),$$
(3)
$$\Delta_{20}(N) = E_0(N,2) - E_0(N,0),$$
(4)

$$\Delta_{30}(N) = E_0(N,3) - E_0(N,0).$$
(5)

In the following way, we estimate the finite-size critical values of $\Delta$ (or $D$) for various values of $D$ (or $\Delta$) for each phase transition. Then, the phase boundary line for the transition is obtained by connecting the results for the $N\to\infty$ extrapolation of the finite-size critical values.

The tTLL state is the TLL state which accompanies the three-magnon bound state, while in the $XY1$ state no magnon bound state accompanies. These lead to the following fact. In the ground-state magnetization curve for a given finite-size system, the magnetization increases stepwise with increasing the magnitude of the external magnetic field applied along the $z$-axis; the first step occurs from the $M=0$ to the $M=3$ state in the tTLL phase, while it occurs from the $M=0$ to the $M=1$ state in the $XY1$ phase. From these arguments, it is easy to see that the finite-size critical values for the phase transition between the tTLL and $XY1$ phases are calculated by solving

$$\Delta_{30}(N)/3 = \Delta_{10}(N).$$
(6)

numerically. Similarly, the nTLL state accompanies the two-magnon bound state, and in this state the first step in the ground-state magnetization curve for a finite-size system occurs from the $M=0$ to the $M=2$ state. Therefore, the finite-size critical values for the phase transition between the nTLL and $XY1$ phases can be estimated from

$$\Delta_{20}(N)/2 = \Delta_{10}(N).$$
(7)

The above arguments imply that the equation from which the finite-size critical values for the phase transition between the tTLL and nTLL phases is given by

$$\Delta_{30}(N)/3 = \Delta_{20}(N)/2.$$
(8)

The tTLL‑Néel, nTLL‑Néel', and $XY1$‑Néel' phase transitions are of the Berezinskii-Kosterlitz-Thouless type [1] with accompanying the spontaneous translational-symmetry breaking. Therefore, the phase boundary lines can be accurately estimated by the level spectroscopy method developed by Okamoto and Nomura [2]. Considering
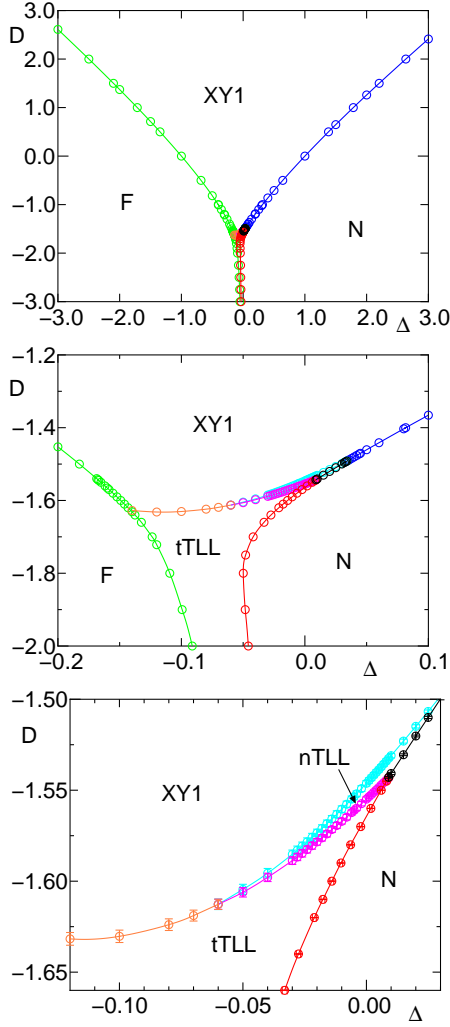
Figure 1: Ground-state phase diagram on the $\Delta$ versus $D$ plane obtained in the present work. The topmost figure is the whole view, and the middle and bottom figures are, respectively, the enlarged views near the tTLL and nTLL regions.



Figure 2: Dependence $E_{3\mathrm{mbe}}(N)$ ($N=6$, 8, 10, 12, 14) on $D$ for $\Delta=-0.1$.
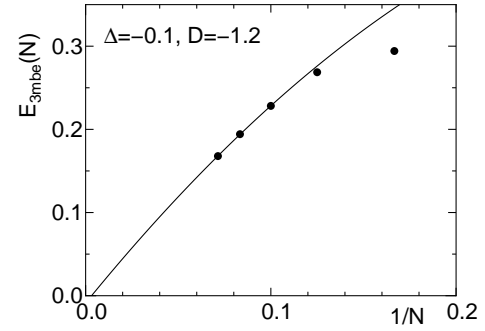


Figure 3: Dependence $E_{3\mathrm{mbe}}(N)$ on $1/N$ for $\Delta=-0.1$ and $D=-1.2$. The solid line represents the fitting to a quadratic function of $1/N$, where the data for $N=10$, 12, 14 are used.

the above discussions related to the magnon bound states, we can obtain the equations from which the finite-size critical values for these three phase transitions; they are, respectively,

$$\Delta_{30}(N)/3 = \Delta_{00}(N)\,, \qquad (9)$$
$$\Delta_{20}(N)/2 = \Delta_{00}(N)\,, \qquad (10)$$
$$\Delta_{10}(N) = \Delta_{00}(N)\,. \qquad (11)$$

It is apparent that the finite-size critical values for the phase transition between the F and $XY1$ phases and that between the F and tTLL phases, both of which are of the first order, are calculated from

$$E_0(N,3N/2) = E_0(N,0)\,. \qquad (12)$$

Finally we discuss the binding energy, $E_{3\mathrm{mbe}}(N)$,

of three magnons give by

$$E_{3\mathrm{mbe}}(N) = \Delta_{30}(N) - 3\Delta_{10}(N)\,. \qquad (13)$$

It should be noted that this equation is closely related to Eq. (6). Figure 2 shows the dependence of $E_{3\mathrm{mbe}}(N)$ on $D$ for $\Delta=-0.1$ in the region including the critical value of the tTLL-$XY1$ transition point, $D=D_{\mathrm{c}}=-1.630\pm0.003$. We see from this figure that in the tTLL region ($D<D_{\mathrm{c}}$), the values of $E_{3\mathrm{mbe}}(N)$ are negatively finite for finite $N$'s as well as for the $N\to\infty$ limit, while in the $XY1$ region ($D>D_{\mathrm{c}}$), they are positively finite for finite $N$'s and vanish for the $N\to\infty$ limit (see Fig. 3). These results are consistent with the well-known fact that the transverse two-spin correlation function $\langle S_1^+ S_{1+j}^-\rangle$ decays exponentially and algebraically in the tTLL and $XY1$ states, respectively.

[1] Z. L. Berezinskii, Sov. Phys. JETP **34**, 610 (1971); J. M. Kosterlitz and D. J. Thouless, J. Phys. C **6**, 1181 (1973).
[2] K. Okamoto and K. Nomura, Phys. Lett. A **169**, 433 (1992).

# Finite-size scaling analysis with bond-weighted tensor renormalization group

Satoshi MORITA

*Graduate School of Science and Technology, Keio University*
*Yokohama, Kanagawa 223-8522*

Tensor network (TN) methods are attracting much attention as powerful tools in various fields including quantum many-body physics, quantum computation, and machine learning. In the classical statistical physics, the state sum in the partition function can be represented in the form of TN. However, the contraction of a large TN still requires an exponentially large computational effort. One of solutions to this problem is the real-space renormalization group. The tensor renormalization group (TRG) method and its variants calculate a coarse-grained tensor by information compression using the singular value decomposition [1, 2]. Since one step of renormalization doubles the system size, these methods can calculate the partition function approximately in logarithmic time for the system size. Recently, Adachi, et al. have proposed the bond-weighted TRG (BWTRG) method, which improves the accuracy of TRG by introducing a bond weight and distributing it appropriately [3].

Recently, we have proposed an algorithm to calculate higher-order moments of physical quantities based on the higher-order TRG (HOTRG) [4]. We introduce an impurity tensor which represents a physical quantity. With the appropriate update rule, a coarse-grained impurity tensor containing multiple impurities can be generated to calculate the higher-order moments of the physical quantity. We have succeeded to estimate the critical exponents and the critical temperature based on the finite-size scaling analysis of the squared magnetization and distinguish the weakly first-order and continuous phase transitions in the Potts model.

In this study, we generalize this impurity method to BWTRG. Unlike HOTRG, BWTRG involves tensor decomposition, making it difficult to construct consistent update rules for the impurity tensor. Therefore, we propose to place an impurity at a bond rather than a site, and successfully derive the update rule for the impurity matrix on a bond. BWTRG can smoothly improve accuracy from TRG by tuning the hyperparameter, Our impurity method also holds this property. We investigate how the accuracy of the finite-size scaling analysis depends on this hyperparameter. We find that the accuracy of the critical point decays with the power of the bond dimension and its exponent smoothly changes with the hyperparameter. The error decays most quickly at the value of the hyperparameter expected to be optimal in BWTRG.

# References

[1] M. Levin and C. P. Nave, Phys. Rev. Lett. **99**, 120601 (2007).

[2] Z. Y. Xie, J. Chen, M. P. Qin, J. W. Zhu, L. P. Yang, and T. Xiang, Phys. Rev. B **86**, 1 (2012).

[3] D. Adachi, T. Okubo, and S. Todo, Phys. Rev. B **105**, L060402 (2022).

[4] S. Morita and N. Kawashima, Comput. Phys. Commun. **236**, 65 (2019).

# Structure analysis of Sb/Bi heterostructure on Si(111) by Total-Reflect High-Energy Positron Diffraction with 2DMAT

D. Iwasawa, H. Abe, T. Takeda, M. Shoji,

I. Mochizuki[A], K. Wada[A], T. Hyodo[A] and A. Takayama

*Department of Physics, Waseda University, Ohkubo, Shinjuku-ku, Tokyo 169-8555*

*[A]IMSS, KEK, Oho, Tsukuba, Ibaraki 305-0801*

## Introduction

Since the experimental demonstration of topological insulators, they have actively been investigated due to their intriguing fundamental properties and potential applications in spintronics devices and quantum computations. Recently a lot of studies focusing on topological phase transitions have been performed in various materials, and topological phase transitions by epitaxial strain at the interface are very useful from the viewpoint of applications because they do not require any external field environment and are compatible with surface sensitive experimental technique.

Group-V semimetal bismuth (Bi) and antimony (Sb) turn from being topologically trivial to nontrivial by slight lattice strain. For Bi, the phase transition to a topological semimetal induced by 0.4%–1% lattice strain has theoretically been predicted [1]. Various theoretical predictions have also been reported for ultrathin Sb films. For instance, freestanding Sb(111) films with less than 4 BL have been reported to be topologically trivial, however several calculations predicted that the topological phase transition can be induced by tuning structural parameters [2]. To observe and discuss the details of the topological phase transition in Sb ultrathin films experimentally, it is necessary to fabricate Sb thin films on substrates with a larger lattice constant and to analysis and determine the atomic structure.

In this work, we have performed structure analysis of ultrathin Sb films on Bi(111) using by total-reflect high-energy positron diffraction (TRHEPD). A structural analysis of Bi was carried out first, followed by a stacked Sb structure. The TRHEPD experiment consists of measuring a series of the diffraction patterns for a fixed incident azimuthal direction at various glancing angles $\theta$. Here, the rocking curve is defined as the diffraction intensity of the (00) spot plotted as a function of $\theta$. In the structural analysis, the experimental rocking curves are compared with those calculated for various structural models. For analysis, calculations of the rocking curves for TRHEPD were performed by the structure-analysis program 2DMAT [3].

## Results and discussion

Figure 1(a) shows the rocking curves of Bi(111) thin film for 10BL measured under the many-beam (MB) condition. In the MB condition, the beam is incident along a symmetric direction, thus the rocking curve in the MB condition essentially gives the information on the atomic positions in the in-plane and out-of-plane direction. Here, we considered a structural model with the Bi interlayer distance and the in-plane lattice constant as parameters. The results of the analysis showed that the structure shown in Fig. 1(b) reproduced the experimental results best; the in-plane lattice constant is 4.38 Å, and the
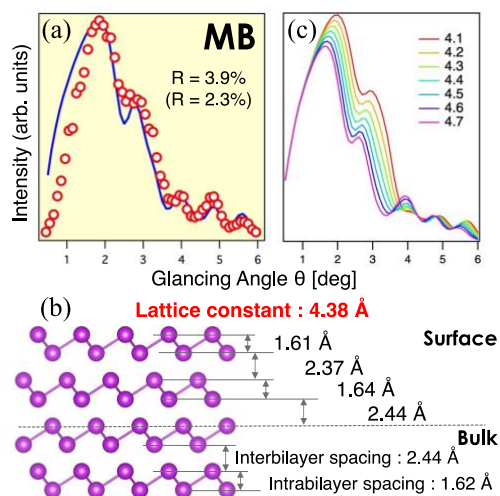
Fig. 1: Experimental measured rocking curves under MB condition for Bi thin films (10 BL) with calculated curves with the structure model in (b). (c) Dependence of the rocking curve on the in-plane lattice constant.



Fig. 2: (Left) Experimental measured rocking curves under OB condition and (right) determined structure model for Sb/Bi heterostructure.

layer distances correspond well with the results of previous studies. We also calculated rocking curves under the OB condition with several in-plane lattice constant [Fig. 1(c)]. One sees the shape of the rocking curve changed significantly in response to the value of the in-plane lattice constant, and we found the experimental results are not reproduced by the lattice constant of bulk Bi (4.54 Å). This result suggest that the Bi is a topologically non-trivial.

Next we have performed structure analysis of ultrathin Sb films (2 BL) on Bi(111). By electron diffraction, we have confirmed that Sb thin film grows on Bi with different lattice constant. However, no moiré pattern was observed in electron diffraction, so it is not possible to construct a structural model assuming a long-period structure. Therefore we have performed TRHEPD measurement under the one-beam (OB) condition. In the OB condition the beam

is incident along an off-symmetric direction. The Rocking curve in the OB condition essentially gives the information on the atomic positions in the out-of-plane direction and atomic density in layer. In this analysis, the lattice constant of Sb relative to Bi 1 BL was estimated by calculating the density of Sb. Figure 2 shows the rocking curves of Sb/Bi heterostructure measured by TRHEPD and determined structure model. As a result of the analysis, the in-plane lattice constant of Sb thin films on Bi was estimated to be 4.08 Å. This value corresponds with that estimated from electron diffraction. For more detailed structure determination, a heterostructure model will be constructed from this estimate in the future, and the structure will be analyzed in a giant lattice system.

## References

[1] T. Hirahara, *et al*., Phys. Rev. Lett. **109** (2012) 227401.

[2] Z.-Q. Huang, *et al*., New J. Phys. **16** (2014) 105018.

[3] Y. Motoyama, *et al*., Computer Physics Communications, **280** (2022) 108465.

# Theoretical proposals of novel superconducting phenomena in strongly correlated systems with multi-degrees of freedom

Shuntaro SUMITA

*Department of Basic Science, The University of Tokyo, Meguro, Tokyo 153-8902*

We have studied an interplay between incommensurate magnetism and superconductivity. The target material is CrAs, in which an incommensurate helimagnetic state is realized at ambient pressure, whereas the magnetic order is suppressed and superconducting phase transition occurs by applying pressure [1]. We performed the first-principles calculations for the paramagnetic state of CrAs by using the QUANTUM ESPRESSO [2, 3], and found that some of the Fermi surfaces are located near the $R$–$S$ line, which is the Brillouin zone boundary $(\pi, \pi, k_z)$ for the space group $Pnma$ of CrAs. Since an electronic state on this line behaves as an anomalous pseudospin that does not couple to a Zeeman field because of the nonsymmorphic symmetry [4], we expect that the property induces novel features for both magnetism and superconductivity.

We designed an effective tight-binding model reproducing the Fermi surfaces around the $R$–$S$ line, and introduced Hubbard and exchange interactions. We are now analyzing the Ginzburg–Landau theory construct from the microscopic model to understand the interplay between magnetism and superconductivity. The detailed results will be presented in the future [5].

As another project, furthermore, we have studied spin parity effects in an one-dimensional antiferromagnetic chain with an easy-plane anisotropy under a transverse magnetic field. To understand the ground-state property, we performed numerical exact diagonalization for $S = 1/2, 1, ..., 5/2$, using the QuSpin package [6]. Also, we obtained entanglement spectra of the ground state by the density matrix renormalization group analyses using `ITensors.jl` [7]. We discovered that spin parity effects clearly appear as finite-size effects in the magnetization curve when the anisotropy is sufficiently large [8].

# References

[1] W. Wu *et al.*, Nat. Commun. **5**, 5508 (2014).

[2] P. Giannozzi *et al.*, J. Phys. Condens. Matter **21**, 395502 (2009).

[3] P. Giannozzi *et al.*, J. Phys. Condens. Matter **29**, 465901 (2017).

[4] Y. Yu *et al.*, arXiv:2310.00838.

[5] S. Sumita and D. F. Agterberg, in preparation.

[6] P. Weinberg and M. Bukov, SciPost Phys. **2**, 003 (2017); *ibid.* **7**, 020 (2017).

[7] M. Fishman *et al.*, SciPost Phys. Codebases 4 (2022); *ibid.* 4-r0.3 (2022).

[8] S. Sumita, A. Tanaka, and Y. Kato, arXiv: 2402.19311.

# Tensor-network-based finite-size scaling of critical phenomena

Atsushi Ueda, Haruki Shimizu, and Masaki Oshikawa

*Institute for Solid State Physics,*

*The University of Tokyo, Kashiwa-no-ha, Kashiwa, Chiba 277-8581*

We have investigated critical phenomena in one-dimensional quantum and two-dimensional classical systems utilizing the tensor-network-based approaches. Extending our previous finite-size scaling studies of the energy spectrum under periodic boundary conditions, we have clarified the effects of the finite bond dimensions in the tensor-network renormalization calculations [1]. The finite bond dimensions induce a finite correlation length; finite-size scaling analyses using the systems smaller than the correlation length give extremely accurate results.

In order to extend our success to boundary critical phenomena, we have developed conformal perturbation theory of finite-size energy spectrum for open boundary conditions [2]. A systematic understanding for open boundary conditions has previously been missing, primarily due to the complexity introduced by both bulk and boundary perturbations. We observed that the optimal system size to be used for finite-size scaling is not always simply given by the number of lattice sites, because of the boundary perturbations. This subtlety has been largely ignored in prior studies, allowing us to provide new insights into accurate finite-size scaling analyses. Large-scale DMRG simulations, performed on the ISSP supercomputer, were indispensable for verifying our theory.

Furthermore, these simulations enabled us to propose an efficient method for computing universal properties on unorientable manifolds [3]. While extending this approach to higher dimensions is not straightforward—due to the increased computational costs associated with contracting higher-dimensional tensors—the use of the ISSP supercomputer has facilitated efficient parallelization of these processes. Consequently, we have been able to explore new physical phenomena in two-dimensional systems, such as anyonic chiral spin liquids [4] and three-dimensional criticality [5], which have previously posed significant challenges.

## References

[1] A. Ueda and M. Oshikawa, Phys. Rev. B **108**, 024413 (2023).

[2] Y. Liu, H. Shimizu, A. Ueda, and M. Oshikawa, e-print arXiv:2405.06891 (2024).

[3] H. Shimizu and A. Ueda, e-print arXiv:2402.15507 (2024).

[4] K. Ohmori, A. Ueda, and K. Inamura in preparation.

[5] A. Ueda and S. Akiyama in preparation.

# Second harmonic generation induced by dynamics of pinned superconducting vortex

Yusuke MASAKI

*Department of Applied Physics, Tohoku University*
*Sendai, Miyagi 980-8579*

Recently, Nakamura *et al.* reported the giant second harmonic generation (SHG) from thin film superconductors in which transport current was applied [1]. The mechanism of the SHG has been attributed to the pinned vortex dynamics driven by the THz irradiation.

This year, we focused on the numerical simulation of the time-dependent Ginzburg–Landau equation coupled with the Maxwell equations to study the photo-driven dynamics of the superconducting vortex. Our setup includes a single vortex pinned in the center of the system. The external electric field has the gaussian form with the central frequency (driving frequency) $\omega_{\mathrm{ext}}$.

Our main results are as follows. Figure 1(a) shows the Fourier spectra of the total current induced by the external field. The orange (blue) curve labeled "$B_j = 0.05$" ("$B_j = 0.0$") is the one in the presence (absence) of the transport current, while the black dashed curve is the Fourier spectrum of the input electric field. We confirmed that application of the transport current enhances not only the SH component but also the third harmonic component. Figure 1(b) shows the $\omega_{\mathrm{ext}}$-dependence of the SH intensity. This calculation requires many-core systems. The SH intensity has a noticeable peak at around $\omega_{\mathrm{ext}} = 0.1$. We have clarifid that this peak is realized when both of the pinned vortex and the transport current exist. Corresponding peak structures appear also in the Fourier spectra of time evolution of the center of mass coordinate for the vortex.

Therefore we attribute this resonant SH component to the dynamics of the pinned vortex under the transport current.
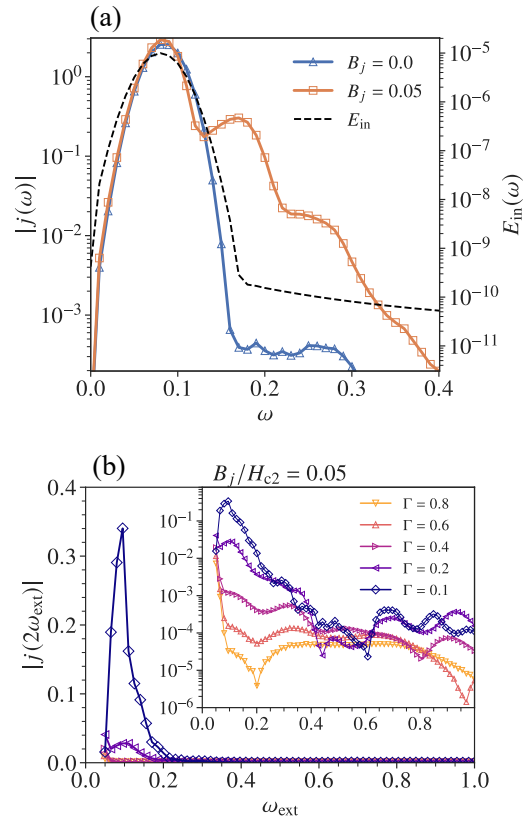


Figure 1: (a) Fourier spectra of the currents and the external field. (b) $\omega_{\mathrm{ext}}$-dependence of the SH component of the current.

# References

[1] S. Nakamura *et al.*: Phys. Rev. Lett. **125**, 097004 (2020).

# Equilibration and glass transition in self-propelled hard polygon systems

Masaharu ISOBE

*Nagoya Institute of Technology*

*Gokiso-cho, Showa-ku, Nagoya, 466-8555*

As the simplest models, the hard disk/sphere systems have been extensively investigated through molecular simulation for both equilibrium and non-equilibrium phenomena [1]. In this project, we focus on the equilibration and non-equilibrium phase transitions in the self-propelled hard polygon model system using modern algorithms, *i.e.*, Event-Chain Monte Carlo (ECMC) [2, 3], Newtonian Event-Chain Monte Carlo (NECMC) [4], and Event-Driven Molecular Dynamics (EDMD) [5].

*Simple and efficient methods for local structural analysis in polydisperse hard disk systems*

Quantifying the nearest (and higher-order) neighbors and local free volumes of particles in nonequilibrium statistical physics systems is crucial for elucidating the origins of macroscopic collective phenomena, such as glass/granular jamming transitions and various behaviors of active matter. However, conventional techniques, such as those based on a fixed-distance cutoff or the Voronoi construction, have primarily been applied to equilibrated, homogeneous, and monodisperse particle systems. In this study, we implement simple and efficient methods for local structure analysis in nonequilibrium, inhomogeneous, and polydisperse hard disk systems. We introduce an efficient and non-reciprocal method for detecting neighbors, namely, 2D SANNex, and a simple, efficient, and precise method for categorizing neighbors to enclose the local free area (NELF-A) in dense polydisperse hard disk systems [6]. We also demonstrate how these novel methods can overcome the difficulties encountered by conventional techniques and present some applications.

As an application of NELF-A, we propose an alternative method to obtain the inherent structure, which avoids the use of short-time averaged coarse-graining trajectories. The summary of the algorithm is as follows:

1. The displacement vectors from a particle position to the geometric center of the Free Volume (FV) estimated by NELF-A for each particle are drawn.

2. The positions in the entire system are updated with the displacement vectors multiplied by a scaling parameter less than unity.

3. Repeat step 2 until the positions converge toward an inherent structure.

In an equilibrium state, the positions eventually converge after the above procedure, and the isotropic shape of FV located on a triangular lattice can be observed, indicative of the inherent structure. Even in a typical non-equimolar binary mixture hard disk system, the probability density distribution obtained by the described procedure is fairly consistent with that obtained by the conventional method based on short-time averaged coarse-graining trajectories. We also confirmed the accuracy of this method by estimating pressure based on FV and comparing it with other conventional methods [7].

*Phase transition in dense hard triangle systems by Newtonian Event-Chain Monte Carlo*

In this study, we investigate the phase transition of hard triangle systems by increasing the packing fraction (density) through the application of two novel algorithms: (i) Newtonian Event-Chain Monte Carlo, recognized for its efficiency in translational diffusion in hard sphere systems, and (ii) XenoSweep [8], which is efficient for contact detection between rigid objects. These algorithms facilitate the equilibration of hard triangle particle systems, which have notably different shapes from hard disks. To characterize the phase transition, we focus on the diffusional characteristics and novel orientational order parameters for the hard triangle particle system, as proposed in our current study [9].

*Crystallization and Motility-Induced Phase Separation in the Flow of Active Brownian Particles Around an Obstacle*

In fluid dynamics, the flow around an obstacle is a classic area of study, where phenomena such as vortex formation and turbulence instability occur with the increase in the control parameter, namely, the Reynolds number. A well-known example of this is the Kármán vortex street. Previously, this phenomenon has been thoroughly investigated through numerical methods, including both direct numerical simulation (DNS) based on the macroscopic Navier-Stokes equations and molecular dynamics simulation using classical microscopic equations of motion. We focus on the phase changes of the flow composed of massive Active Brownian Particles (ABP) with the Weeks-Chandler-Andersen (WCA) repulsive force around a fixed obstacle, analyzed through large-scale molecular dynamics simulation (*HOOMD-blue v4*). We observed nontrivial flow instabilities leading to the formation of vortices, turbulence, and notably, crystallization, influenced by both the Reynolds number and the magnitude of self-propulsion velocity. Unlike the WCA system, the ABP system demonstrated crystallization through two distinct mechanisms: (i) collision-induced crystallization with the cylinder, leading to pressure-induced crystallization, and (ii) crystallization triggered by motility-induced phase separation (MIPS). In both cases, it was observed that the number density within the crystalline clusters exceeded the Alder transition point of equilibrium systems. These findings suggest that crystallization in the non-equilibrium ABP flow around a cylinder might occur through mechanisms akin to those in equilibrium systems. The roles of self-propulsion magnitude and rotational diffusion coefficient in the crystallization mechanism are summarized [10].

# References

[1] M. Isobe: Mol. Sim. **42** (2016) 1317.

[2] E. P. Bernard, W. Krauth, and D. B. Wilson: Phys. Rev. E **80** (2009) 056704.

[3] W. Krauth: Front. Phys. **9** (2021) 229.

[4] M. Klement and M. Engel: J. Chem. Phys. **150** (2019) 174108.

[5] M. Isobe: Int. J. Mod. Phys. C **10** (1999) 1281.

[6] D. Mugita, K. Souno, H. Koyama, T. Nakamura, and M. Isobe: J. Chem. Phys. (2024) *in press.*

[7] D. Mugita, K. Souno, and M. Isobe: *in preparation*

[8] M. Klement, S. Lee, J. A. Anderson and M. Engel: J. Chem. Theor. Comp. **17** (2021) 4686.

[9] T. Shirai, D. Mugita, and M. Isobe: Proceedings of the 29th Symposium on Traffic Flow and Self-driven Particles, **29** (2024) 49. (in Japanese)

[10] K. Iwase and M. Isobe: *in preparation.*

# Numerical Study of One Dimensional Frustrated Quantum Spin Systems

Kazuo HIDA

*Professor Emeritus, Division of Material Science,*
*Graduate School of Science and Engineering,*
*Saitama University, Saitama, Saitama 338-8570*

## 1 Model

We investigate the ground-state phases of mixed diamond chains described by the following Hamiltonian:[1]

$$\mathcal{H} = \sum_{l=1}^{L} \Big[ (1+\delta) \boldsymbol{S}_l (\boldsymbol{\tau}_l^{(1)} + \boldsymbol{\tau}_{l-1}^{(1)})$$
$$+ (1-\delta) \boldsymbol{S}_l (\boldsymbol{\tau}_l^{(2)} + \boldsymbol{\tau}_{l-1}^{(2)}) + \lambda \boldsymbol{\tau}_l^{(1)} \boldsymbol{\tau}_l^{(2)} \Big], \quad (1)$$

where $\boldsymbol{S}_l, \boldsymbol{\tau}_l^{(1)}$ and $\boldsymbol{\tau}_l^{(2)}$ are spin operators with magnitudes $S_l = \tau_l^{(1)} = 1/2$ and $\tau_l^{(2)} = 1$, respectively. The number of unit cells is denoted by $L$. The lattice structure is depicted in Fig. 1. We consider the region $\lambda \geq 0$ and $1 \geq \delta \geq -1$.
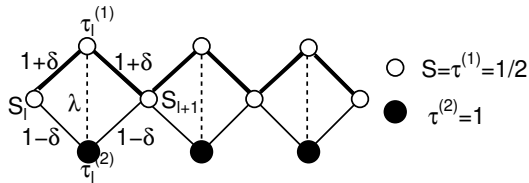


Figure 1: Structure of the diamond chain investigated in this work.

## 2 Numerical Results

We have carried out the numerical exact diagonalization (NED) calculation for $L = 4, 6$ and 8 and the DMRG calculation for $L = 48$. The spontaneous magnetization $m_{\mathrm{sp}}$ in each phase is calculated to obtain the ground-state phase diagram of Fig. 2.
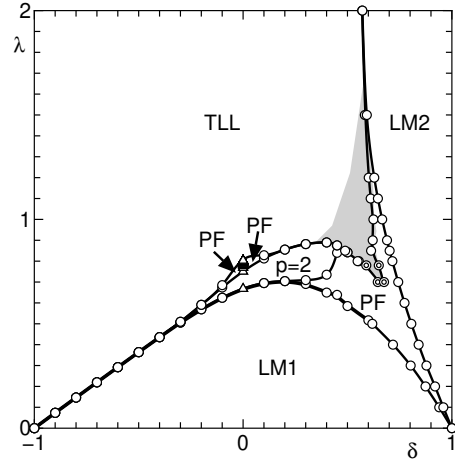


Figure 2: Ground-state phase diagram. The open circles are the phase boundaries estimated from the NED data extrapolated to the thermodynamic limit from $L = 4, 6$ and 8 by the Shanks transform. The double circles are the phase boundaries estimated from the DMRG data for $L = 48$. The triangles at $\delta = 0$ are the phase boundaries between the infinite series of QF phases determined in Ref. [5]. The deviation from the scaling relation $\Delta E \sim 1/L$ for $L = 18$ and 24 is significant in the shaded area. The curves are guides for the eye.

Two Lieb-Mattis-type quantized ferrimagnetic (QF) phases (LM1, LM2) with $m_{\mathrm{sp}} = 1$ are separated by the partial ferrimagnetic (PF) phase and nonmagnetic phase as shown in Fig. 3 for $\lambda = 0.6$.
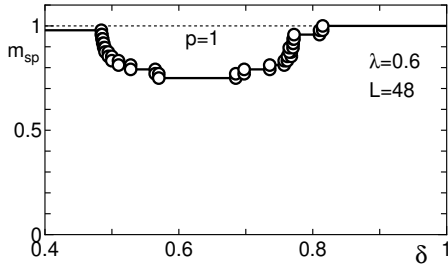
Figure 3: $\delta$-dependence of $m_{\mathrm{sp}}$ in the ground state for $\lambda = 0.6$ calculated by the DMRG method for open chains with $L = 48$.

As for the nonmagnetic phase, the conventional Lieb-Schultz-Mattis (LSM) theorem[2] does not exclude the unique gapped phase, since the sum of the spin magnitudes in a unit cell is an integer. However, our model satisfies the condition to exclude the unique gapped phase in the recent extension of the LSM theorem to the site-reflection invariant spin chains.[3] Taking the continuity to the TLL phase in the limit $\lambda \to \infty$ and $\delta = 0$ [4] into account, the whole nonmagnetic phase is considered to be the TLL phase.

It is checked that the singlet-triplet energy gap $\Delta E$ calculated by the NED method approximately scales with the system size $L$ as $\Delta E \sim 1/L$ as shown in Fig.4(a) for $\delta = -0.3$ and (b) for $0.3$. Similar analyses are also carried out for several other values of $\delta$. In the vicinity of the PF phase indicated by the shaded area of Fig. 2, however, the deviation from the scaling relation $\Delta E \sim 1/L$ is significant as shown in Fig. 4(c). Nevertheless, this area shrinks with the system size. Hence, it is likely that the whole nonmagnetic phase is a TLL phase.

The effect of $\delta$ on the infinite series of ferrimagnetic phases found for $\delta = 0$[5] is also investigated. It is shown that the bosonization argument supports the numerically found fragility of the ferrimagnetic phases with large spatial periodicities reported in [4].
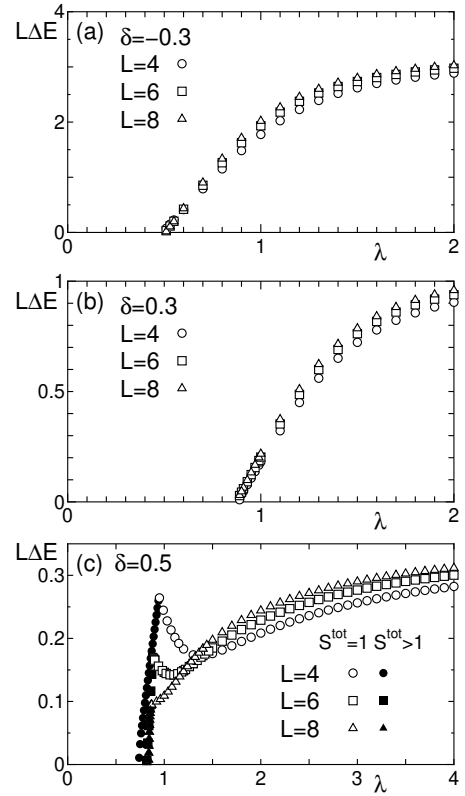


Figure 4: $\lambda$-dependence of the scaled gap $L\Delta E$ of the lowest excitations for (a) $\delta = -0.3$, (b) $0.3$ and (c) $0.5$ with $L = 4, 6$ and $8$. The open and filled symbols are the excitations with total spin $S^{\mathrm{tot}} = 1$ and $S^{\mathrm{tot}} > 1$, respectively.

# References

[1] K. Hida, J. Phys. Soc. Jpn. **93**, 044703 (2024).

[2] E. Lieb, T. Schultz, and D. Mattis, Ann. Phys. **16**, 407 (1961).

[3] Y. Ogata, Y. Tachikawa, and H. Tasaki, Commun. Math. Phys. **385**, 79 (2021).

[4] K. Hida, Activity Report 2022/Supercomputer Center, ISSP 341.

[5] K. Hida, J. Phys. Soc. Jpn. **90**, 054701 (2021).

# Proposal of a quantum active particle

Manami YAMAGISHI

*Department of Physics, The University of Tokyo*
*Kashiwa-no-ha, Kashiwa, Chiba 277-8581;*
*RIKEN, Hirosawa, Kashiwa, Saitama 351-0198*

Naomichi HATANO

*Institute of Industrial Science, The University of Tokyo*
*Kashiwa-no-ha, Kashiwa, Chiba 277-8581*

We present a minimal model of a quantum active particle [1] as a building block of quantum active matter. Active matter is a component that takes up energy from the environment, stores it inside, converts the internal energy into kinetic energy, and thereby moves, or a collection of such components. The introduction of the idea of classical active matter enabled us to unify a variety of studies outside conventional classes of dynamics, dynamics without energy or momentum conservation, that had been investigated separately before and to understand their commonalities and universalities. Some researchers very recently tried to introduce the concept of active matter into quantum systems. Starting with a paper by Adachi *et al.* [2], the research field of quantum active matter is expanding [1, 3, 4, 5].

We propose a quantum active particle using non-unitary quantum walks in one and two spatial dimensions (1D and 2D). As a building block of quantum active matter, we start with one-particle systems, setting real-time evolution in a fully quantum range. With our quantum active particle, we have observed similarities to a classical active Brownian particle [6] and distinct quantum features at the same time. As a similarity, we observed that dynamics of our quantum active walker becomes more active in a non-trivial way when a non-Hermiticity parameter $g$, which corresponds to the energy take-up in classical active Brownian particles, becomes larger. As quantum features, we observed ballistic propagation of peaks (1D), particle staying on the constant energy surface (2D) and resonant transition between two energy levels (1D and 2D).

We utilized the Supercomputer at ISSP to numerically diagonalize our time-evolution operator, whose maximum size was $(70 \times 70 \times 8)^2$. By allocating arrays dynamically, we allowed our system to reach the spatial size of $70 \times 70$ (one in the $x$ direction and the other in the $y$ direction).

# References

[1] M. Yamagishi, N. Hatano, and H. Obuse: arXiv:2305.15319 (2023).

[2] K. Adachi, K. Takasan, and K. Kawaguchi: Phys. Rev. Res. **4**, 013194 (2022).

[3] Y. Zheng and H. Löwen: arXiv:2305.16131 (2023).

[4] R. Khasseh, S. Wald, R. Moessner, C.A. Weber, and M. Heyl: arXiv:2308.01603 (2023).

[5] K. Takasan, K. Adachi, and K. Kawaguchi: arXiv:2308.04382 (2023).

[6] F. Schweitzer, W. Ebeling, and B. Tilch: Phys. Rev. Lett. **80**, 5044 (1998).

# Magnetic field effect on a topological chiral order in breathing kagome antiferromagnets

Kazushi AOYAMA

*Department of Earth and Space Science, Graduate School of Science, Osaka University*
*Machikaneyama-cho, Toyonaka-shi, Osaka 560-0043*

In magnetic materials, the scalar spin chirality $\chi_{ijk} = \mathbf{S}_i \cdot (\mathbf{S}_j \times \mathbf{S}_k)$ often plays an important role. When the total chirality summed over all the elementary triangles $\chi^T = \sum_{\triangle_{ijk}} \chi_{ijk}$ is nonzero, an anomalous Hall effect of chirality origin can appear in metallic systems. Since $\chi_{ijk}$ is related to a solid angle subtended by three spins $\mathbf{S}_i$, $\mathbf{S}_j$, and $\mathbf{S}_k$, it is also relevant to topological orders where the total solid angle subtended by all the spin in the magnetic unit cell $\Omega$ takes an integer value in units of $4\pi$. In a skyrmion crystal (SkX) state, both $\chi^T$ and $\Omega/4\pi$ take nonzero values. Previously, we theoretically demonstrated that a zero-field topological chiral order with $\chi^T \neq 0$ and $\Omega/4\pi = \pm 2$ can be realized in the following $J_1$-$J_3$ classical Heisenberg model on the breathing kagome lattice [1] :

$$
\begin{aligned}
\mathcal{H} &= J_1 \sum_{\langle i,j \rangle_S} \mathbf{S}_i \cdot \mathbf{S}_j + J_1' \sum_{\langle i,j \rangle_L} \mathbf{S}_i \cdot \mathbf{S}_j \\
&+ J_3 \sum_{\langle\langle i,j \rangle\rangle} \mathbf{S}_i \cdot \mathbf{S}_j,
\end{aligned} \tag{1}
$$

where the summation $\sum_{\langle\rangle_{S(L)}}$ runs over site pairs on small (large) triangles having the nearest neighbor (NN) interaction $J_1$ ($J_1'$), and $J_3 > 0$ is the third NN antiferromagnetic interaction along the bond direction. The zero-field topological chiral order can be viewed as a miniature version of the SkX. In the work, we examine the stability of this topological chiral order against an external magnetic field $H$.

By performing Monte Carlo (MC) simulations for system sizes upto $L = 288$, we investigate the ordering properties of the $J_1$-$J_3$ model in a magnetic field. Here, the total number of spins $N$ is related to $L$ via $N = 3L^3$. In our simulations, $2 \times 10^5$ MC sweeps are carried out under the periodic boundary condition and the first half is discarded for thermalization. Our 1 MC sweep consists of 1 heatbath sweep and successive 10 overrelaxation sweeps, and observations are done at every MC sweep. The statistical average is taken over 4 independent runs starting from different random initial configurations.

It is found that the topological chiral order is relatively robust against the external magnetic field $H$; for $J_1'/J_1 = 0.4$ and $J_3/J_1 = 1.2$, with increasing field at $T/J_1 = 0.08$, the topological number $\langle|\Omega|\rangle/4\pi = 2$ remains unchanged until it suddenly drops down to zero at $H/J_1 \sim 2$, where $\langle\rangle$ denotes the thermal average. Interestingly, the total chirality $\langle\chi^T\rangle$ remains nonzero even in the high-field non-topological phase at $2 < H/J_1$ where $\langle|\Omega|\rangle/4\pi = 0$. A system size dependence of $\langle\chi^T\rangle$ cannot be seen for $L = 72$, 144, and 288, so that the nonzero $\langle\chi^T\rangle$ would not be due to the finite-size effect. Further analysis is going on to clarify the origin of the nonzero total chirality outside the topological phase.

# References

[1] K. Aoyama and H. Kawamura, Phys. Rev. B **105**, (2022) L100407; J. Phys. Soc. Jpn. **92**, (2023) 033701.

# Study on algorithms for Ising machines

Shu Tanaka

*Department of Applied Physics and Physico-Informatics, Keio University*

*Hiyoshi, Yokohama, Kanagawa, 223-8522*

In recent years, Ising machines, which are specialized computers for metaheuristics such as quantum annealing, have been vigorously developed as a highly efficient solution method for combinatorial optimization problems. Since the announcement of commercial machines by several private companies, academic institutions in Japan and abroad have been proposing Ising machines based on new concepts and new internal algorithms, and conducting research and development of Ising machines for proof-of-concept.

In this research project, we developed a new algorithm based on the knowledge of statistical mechanics to maximize the hardware performance of the Ising machine. It is expected that this research will not only provide the basic technology for the development of software for existing Ising machines, but also lead to the research and development of new Ising machines based on new concepts and new internal algorithms.

## (I) Dynamical process of a bit-width reducing Ising model with simulated annealing [1]

The Ising machine has attracted attention as an efficient solver for combinatorial optimization problems, which are formulated as ground-state (minimum energy) search problems for the Ising model. Due to the limited bit width of the coefficients of the Ising machine, the Ising model must be converted to a bit width reduced (BWR) Ising model. Previous studies have shown that the bit-width reduction method, which adds auxiliary spins, theoretically makes the ground state of the BWR Ising model the same as the Ising model before bit-width reduction (the original Ising model). However, while the dynamical process is closely related to the accuracy of the solution, how the BWR Ising model progresses toward the ground state has not been elucidated. Therefore, we compared the dynamical processes of these models using Simulated Annealing (SA). The results show that there are significant differences in the dynamical processes between the models. The analysis from the viewpoint of statistical mechanics reveals that the BWR Ising model has two characteristic properties: effective temperature and slow relaxation. These properties change the temperature schedule and spin flip probability of the BWR Ising model and lead to differences in the

dynamical processes. Therefore, we have proposed SA parameters for the BWR Ising model. The proposed SA parameters are demonstrated on a square lattice Ising model. The results show that the dynamical processes of the BWR Ising model and the original Ising model are closer.

## (II) Hybrid Optimization Method Using Simulated-Annealing-Based Ising Machine and Quantum Annealer [2]

Ising machines have been developed as fast and accurate solvers for combinatorial optimization problems. In this study, we investigate the performance of a hybrid optimization method that exploits the advantages of both non-quantum Ising machines and quantum annealing machines. The non-quantum Ising machine is used to improve the performance of quantum annealing. In this method, the non-quantum annealing Ising machine first solves the original Ising model multiple times as a preprocessing step. Then, the reduced sub-Ising model generated by spin-fixation is solved by the quantum annealer. The method outperforms the preprocessing SA and the quantum annealer alone in the fully coupled random Ising model.

## References

[1] S. Kikuchi, N. Togawa, and S. Tanaka, IEEE Access **11**, 95493 (2023).

[2] S. Kikuchi, N. Togawa, and S. Tanaka, J. Phys. Soc. Jpn. **92**, 124002 (2023).

# Relaxation process in open quantum systems

Tatsuhiko Shirai

*Waseda Institute for Advanced Study, Waseda University*

*Nishi Waseda, Shinjuku-ku, Tokyo 169-0051*

Many-body Open quantum systems have attracted much attention due to the experimental progress. Markovian dynamics, which is described by the Lindblad equations, exhibit complicated relaxation dynamics towards the steady state. The spectral gap of the Lindblad operator called the Liouvillian gap gives the asymptotic decay, but does not necessarily give a correct estimate of the relaxation time. This is due to the long timescale of the transient regime. Therefore, it is important to clarify the relaxation dynamics in the transient regime.

Here we study the relaxation dynamics of the steady-state autocorrelation function in a bulk-dissipated quantum system. To investigate a transient regime, we introduce an instantaneous decay rate $\kappa_A(t)$ that gives a rigorous upper bound of the autocorrelation function $C_A(t)$ as

$$|C_A(t)| \leq \exp\left(-\int_0^t \kappa_A(\tau)d\tau\right)|C_A(0)|, \quad (1)$$

where $A$ is an operator. The instantaneous decay rate is defined by the symmetrized Liouvillian [1], which symmetrizes the Lindblad operator with respect to a steady-state inner product. We have used openMPI to calculate $C_A(t)$ and $\kappa_A(t)$. Figure 1 (Upper) shows the relaxation dynamics of the autocorrelation function. The decay rate in the transient regime is different from the Liouvillian gap. Figure 1 (Bottom) shows the dynamics of the instantaneous decay rate. The instantaneous decay rate in the transient regime is almost constant, which describes the decay rate of the autocorrelation function in the transient

regime. We interpret the decay rate in the transient regime from the operator spreading due to the unitary time evolution [2].
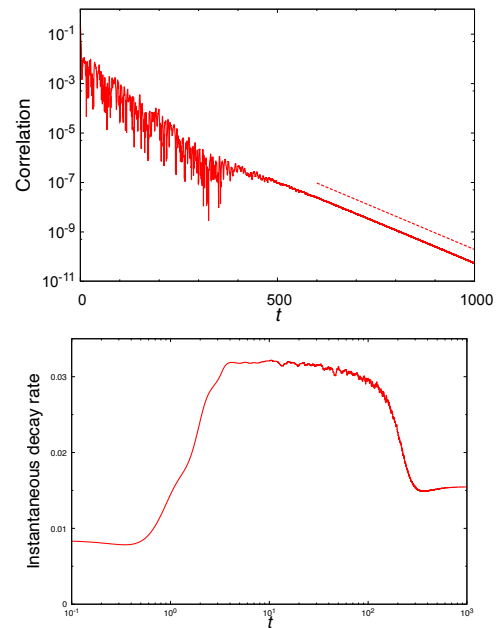


Figure 1: (Upper) Dynamics of the autocorrelation function. The dotted line indicate the decay at the rate of the Liouviilan gap (Bottom) Dynamics of the instantaneous decay rate.

# References

[1] T. Mori and T. Shirai, Phys. Rev. Lett. **130**, 230404 (2023).

[2] T. Shirai and T. Mori, arXiv:2309.03485.

# Analysis of Ising model in statistical-mechanical informatics

Yuya SEKI

*Graduate School of Science and Technology, Keio University, Kanagawa 223-8522*

We have studied properties of factorization machine with annealing (FMA) [1], which is an optimization method based on the simulated/quantum annealing method cooperated with factorization machine (FM), a machine learning model whose model equation is in the quadratic form. FMA is mainly used for discrete black-box optimization problems including integer-variable optimization problems [2]. Since a Hamiltonian is not given analytically in black-box optimization problems, we need to estimate the Hamiltonian whose ground state can be obtained by the simulated/quantum annealing method. In FMA, the Hamiltonian is estimated with training of FM. Since the model equation of FM is in the quadratic form, which is equivalent to the Ising model, the simulated/quantum annealing method can be applied to find its ground state.

This year we focused on interaction graph structure of FM and, we found that FMA with a restricted interaction graph works for certain range of optimization problems via parallel computing on the supercomputer. Since some actual annealing machines including D-Wave machines have limited structure of interaction between spins, Hamiltonian estimated by FM cannot be dealt with actual annealing machines directly. Minor embedding is commonly used to solve the problem. However, the minor embedding method requires ancilla spins to represent fully connected Ising model with a model with sparse interactions used in actual devices. The overhead of ancilla spins is problematic especially for large size systems, because the number of required spins increase quadratically with the number of spins in the original model. To overcome this problem, we proposed FMA with a restricted interaction graph structure. In our method, the interaction graph structure is constructed from the interaction structure of actual annealing devices. Since the interaction graph structures of FM and actual devices are same, no ancilla spins are necessary. We performed parallel computing with various problem instances and parameters in the proposed method. As a result, we found that our method can minimize the Hamiltonian which is generated with an assumption that the model has a sparse interaction whose degree is independent of the system size.

# References

[1] K. Kitai *et al.*: Phys. Rev. Research **2** (2020) 013319.

[2] Y. Seki *et al.*: arXiv:2209.01016 (2022).

# Molecular Dynamics of Stretched Polymer Chains

Koichi MAYUMI, Kosuke AOMURA

*Institute for Solid State Physics,*

*The University of Tokyo, Kashiwa-no-ha, Kashiwa, Chiba 277-8581*

The segmental dynamics of polymer chains is the molecular origin of the entropic elasticity of polymeric materials [1]. When polymer chains are stretched, the molecular dynamics of polymer chains is restricted, and chain tension is increased with stretching. In this study, we have performed full-atomistic molecular dynamics simulations of stretched polymer chains in water.

A polyethylene glycol (PEG) chain consisting of 42 monomers was placed in a simulation box filled with 68,000 water molecules. The MD simulations were performed with GROMACS version 2021.1. The PEG chain was stretched at 0, 5, 10, 30, 70, 100, and 210 kJ/(mol nm). Fig.1 shows the intermediate scattering functions of PEG in the unstretched and stretched states (0 and 10 kj/(mol nm)). The segmental motion of the stretched chain becomes slow in the stretching direction (z-direction), while the chain dynamics in the directions perpendicular to stretching (x and y directions) is accelerated by

stretching. This simulation result is consistent with our quasi-elastic neutron scattering results on the segmental motion of polymer chains in stretched PEG gels [1].
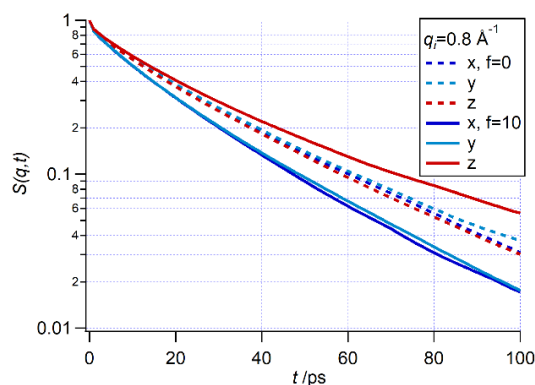


Fig. 1: Simulated intermediate scattering function of unstretched and stretched single PEG chain in water.

## References

[1] M. Rubinstein, R. H. Colby, "Polymer physics", Oxford university press (2003).

[2] K. Aomura, Y. Yasuda, T. Yamada, T. Sakai, K. Mayumi, Soft Matter, **19**, 147 (2023).

# Consideration on the microscopic mechanism of the friction by the frictional force caused by magnetic structures

Hisato Komatsu

*Data Science and AI Innovation Research Promotion Center, Shiga-university*
*Banba, Hikone, Shiga 522-8522, Japan*

Microscopic mechanisms of the friction has not been understood completely, although this phenomenon itself has been known from early ages. Magnetic friction, the frictional force generated from the magnetic interaction between spin variables, has been studied to reveal this mechanism, and many types of theoretical models have been proposed[1, 2].

In the last academic year, we investigated a simplified model of the magnetic friction and consider its finite-size effect[3]. Specifically, we introduced a model composed of $N$ Ising spin variables $\{\sigma_i\}$ interacting with each other by the following Hamiltonian:

$$H = -\frac{J(x)}{N}\sum_{i,j}\sigma_i\sigma_j = -NJ(x)m^2, \quad (1)$$

and considered the time development of the lattice shift $x$ under following overdamped Langevin equation:

$$\gamma N\frac{dx}{dt} = F_{\text{ex}} - \frac{\partial H}{\partial x} + \sqrt{2\gamma NT}R(t). \quad (2)$$

Here, $F_{\text{ex}}$ is the external force, and we let the spin variables obey the Glauber dynamics. The coupling constant $J(x)$ is the periodic function of $x$. Numerical simulations using ISSP Supercomputer revealed that this system shows two different behaviors depending on the damping constant $\gamma$. When $\gamma$ is small, the stick and slip states are separated as the metastable states, and the friction-velocity relation is determined by the probability that each state appears. When $\gamma$ is large, on the other hand, such separation does not appear and the velocity of the magnetic body is determined by the thermal activation process. We also considered the difference of the friction-velocity relation from the Dieterich-Ruina law[4, 5], a well-known empirical law of the usual solid surfaces. However, whether such behavior is observed in the case that the magnetic body is pulled by a certain velocity was not investigated.

In this academic year, we consider the case that the magnetic body is pulled by a chain composed of $n_S$ Voigt units, instead of the fixed external force, and investigated the relation between the frictional force and velocity of the other edge of the chain, $v$. The Langevin equation of $x$ in this case is expressed as follows:

$$\begin{aligned}\gamma N\frac{dx}{dt} &= kN(vt + x_C - x) + \gamma Nv - n_S\frac{\partial H}{\partial x} \\ &\quad + \sqrt{2\gamma Nn_S T}R(t), \quad (3)\end{aligned}$$

where $k$ and $\gamma$ mean the spring and damping constants of Voigt units, and $x_C$ is the position of the other edge of the chain at the initial time $t = 0$. As the result of the numerical simulations using ISSP Supercomputer, the histogram of the magnetization $m$ and the lattice shift $x$ show that the value of $m$ in the slip state largely changes depending on $k$, like Fig. 1. The effect of this difference on the friction-velocity relation should be considered in future works.

[5] J. H. Dieterich, Tectonophysics **144**, 127 (1987)
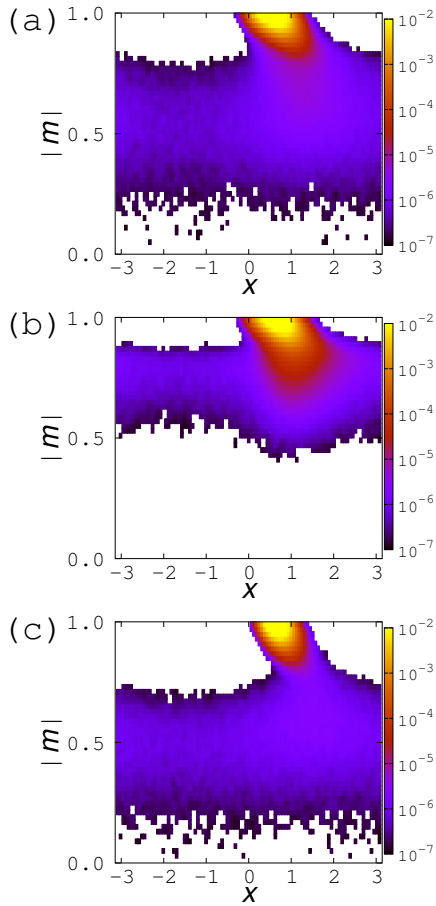


Figure 1: Examples of histograms of the magnetization $m$ and shift of the lattice $x$ under (a) small $k$ and (b) large $k$. Graph (c) is a histogram under a fixed external force which gives the similar velocity to these two graphs.

# References

[1] D. Kadau, A. Hucht, and D. E. Wolf, Phys. Rev. Lett. **101**, 137205 (2008).

[2] M. P. Magiera, L. Brendel, D. E. Wolf, and U. Nowak, Europhys. Lett. **87**, 26002 (2009).

[3] H. Komatsu, Phys. Rev. E. **108**, 034803 (2023)

[4] A. Ruina, J. Geophys. Res. **88**, 10359 (1983)

# Materials informatics researches based on PHYSBO

Ryo TAMURA

*International Center for Materials Nanoarchitectonics,*
*National Institute for Materials Science,*
*1-1 Namiki, Tsukuba, Ibaraki, 305-0044*

PHYSBO is a Python library for fast and scalable Bayesian optimization, which was developed in "Project for advancement of software usability in materials science" by The Institute for Solid State Physics, The University of Tokyo.[?] Using PHYSBO, we performed some materials informatics researches. In this report, two examples are introduced.

First example is the optimization of structures of core-shell nanoparticles (CSNPs)[?]. To perform it, a new black-box optimization technique was developed. In this method, the structure of the CSNPs is optimized using FMQA algorithm[?] and their constituent materials are selected using Bayesian optimization with the optical properties of the materials as the "descriptors". Here, PHYSBO package is used to perform Bayesian optimization. Aiming for applications to i-line photolithography, we searched for CSNPs that are transparent to ultraviolet light of wavelength 355–375 nm and opaque to visible light of wavelength 400–830 nm by our proposed method. The transmittance spectra of the nanoparticles were obtained using a Mie theory calculator[?]. The optimized nanoparticles with the best optical properties have a multilayered structure with a radius of approximately 40 nm and an outer shell are either Mg or Pb.

Second example is a material optimization for electrocatalyst for water electrolyzers[?]. To perform it, we developed a new material search algorithm that accurately predicts materials properties by evolving the prediction method according to the number of data.

In detail, Bayesian optimization based on PHYSBO and binary classification based on random forest classifier are combined. The random forest classification can select active materials for electrocatalyst. By our algorithm with experiments performed by human, a new material suitable for electrocatalytic materials for water electrolyzers was discovered in only one month from about 3,000 candidates. The discovered electrocatalytic material does not use any elements of platinum group and is expected to be an inexpensive electrocatalytic material to produce a large scale water electrolyzers.

# References

[1] Y. Motoyama, R. Tamura, K. Yoshimi, K. Terayama, T. Ueno, and K. Tsuda, Comput. Phys. Commun. **278**, 108405 (2022).

[2] M. Urushihara, M. Karube, K. Yamaguchi, and R. Tamura, Adv. Photon. Res. **4**, 23002 (2023).

[3] K. Kitai, J. Guo, S. Ju, S. Tanaka, K. Tsuda, J. Shiomi, and R. Tamura, Phys. Rev. Res. **2**, 013319 (2020).

[4] O. Peña and U. Pal, Comput. Phys. Commun. **180**, 2348 (2009).

[5] K. Sakaushi, W. Hoisang, and R. Tamura, ACS Cent. Sci. **9**, 2216 (2023).

# Theoretical study for absorption and fluorescence of firefly bioluminescence substrate analogs

Miyabi HIYAMA

*Gunma University*

*Tenjin-cho, Kiryu, Gunma 376-8515*

Firefly luciferin is a substrate for firefly bioluminescence reaction. In this year, we studied core excitation of firefly luciferin in Carbon (C) K-edge X-ray absorption spectra [1] and the free energy for the firefly luciferin analogs named "seMpai" [2] using the density functional theory (DFT) and time-dependent (TD) DFT calculations. All calculations using the computational chemistry software package, Gaussian09 [3], were performed on system B of Super Computer Center in ISSP.

C K-edge X-ray absorption spectra for firefly luciferin in aqueous solutions at pH 5, 7, and pH 10 were measured using a soft X-ray spectroscopy measurement system [1]. It was found that the C K-edge spectra for firefly luciferin have four characteristic peaks. The peak energies for pH 5 were the same as those for pH 7.

To assign these spectra, the TDDFT calculations for the core excitations of firefly luciferin anion and dianion were carried out, because the most abundant chemical species at pH 5 and 7 is knows as a firefly luciferin anion and that at pH 10 is a firefly luciferin dianion [4]. The structure of firefly luciferin dianion is deprotonated one from the hydroxy group of firefly luciferin anion.

From the assignments of C K-edge X-ray absorption spectra for firefly luciferin, it was found that the effect of deprotonation of the hydroxy group appears in the energy difference of the first and second peaks of these spectra. These results indicated that the deprotonation of the hydroxy group can be distinguished based on the soft X-ray absorption spectra.

"seMpai", is one of the firefly luciferin analogs and produces red luminescence with firefly luciferase [2]. To obtain free energies for the ground states of seMpai and its conjugate acids and bases expected to be main component in the aqueous solutions, the vibrational analysis for these chemical species were carried out. It was found that the calculations for vibrational analysis using Gaussian09 with the bases set, cc-pVTZ, were converged, but those with the larger basis set, aug-cc-pVTZ were not.

# References

[1] Y. Kudo, F. Kumaki, M. Nagasaka, J-i. Adachi, Y. Noguchi, N. Koga, H. Itabashi, and M. Hiyama: J. Phys. Chem. A **128**, 611 (2024).

[2] R. Saito, T. Kuchimaru, S. Higashi, S. W. Lu, M. Kiyama, S. Iwano, R. Obata, T. Hirano, S. Kizaka-Kondoh, and S. A. Maki: Bull. Chem. Soc. Jpn. **92**, 608 (2019).

[3] Gaussian09 Revision D.01, M. J. Frisch et al.

[4] Y. Ando and H. Akiyama: J. J. App. Phys. **49**, 117002 (2010).

# Application of Symbolic Regression with Alpha Zero to Find Analytical Methods in Physics

Yoshihiro MICHISHITA

*Center for Emergent Matter Science (CEMS),*

*RIKEN, HIrosawa, Wako, Saitama 351-0198*

We have studied an application of the symbolic regression with Alpha Zero[1] to find the analytical methods in physics, especially about periodically-driven systems using massive parallel computer simulations.

We proposed a framework for deriving theoretical analysis methods in physics using symbolic regression with the Alpha Zero algorithm.

In all previous studies using symbolic regression in physics, the goal was to identify the equations of unknown nonlinear dynamics, whereas in this study, the goal was to search for a basis that would facilitate theoretical analysis of the dynamics, assuming that the equations of dynamics are known.

In addition, existing studies have used genetic algorithms, Monte Carlo tree search, and regression neural networks, but Alpha Zero overcomes their weak points.

In this study [2], focusing on period-driven systems in particular, Alpha Zero "derives" the Floquet-Magnus expansion by setting "the smallness of the time dependence of the Hamiltonian after time-dependent unitary transformation" as a "measure of convenience for theoretical analysis. We have shown that Alpha Zero "derives" the Floquet-Magnus expansion. This is derived by symbolic regression, so it literally derives a table expression.

We also found that the Alpha Zero algorithm performs better than other reinforcement learning methods such as epsilon-greedy and Actor-Critic (PPO).

============================
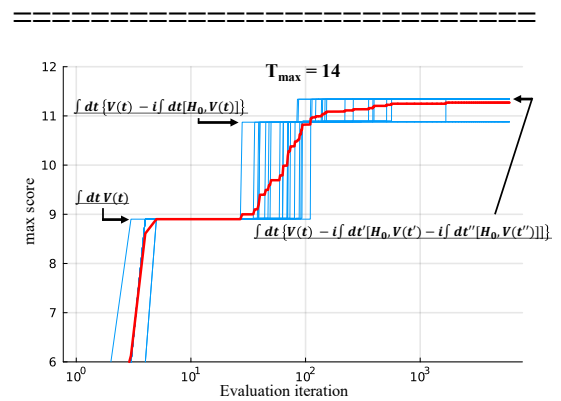


FIG: Searching dynamics by Alpha Zero for Physics.

============================

# References

[1] D. Silver, et al,Science. **362**, 1140 (2018).

[2] YM, J. Phys. Soc. Jpn. **accepted**(2024).

# Development of integrated interface of eigensolvers Rokko and application to quantum spin systems

Tatsuya Sakashita

*Center for Quantum Information and Quantum Biology, Osaka University*
*1-2 Machikaneyamachō, Toyonaka, Osaka 560-0043*

To establish universal exact diagonalization package for quantum lattice models including the Heisenberg-Kitaev model, we focused on developing integrated interfaces for eigensolvers, "Rokko"[1].

In Rokko, we implemented the integrated interfaces for the following types:

- Serial solvers for dense matrices (Eigen3, LAPACK)

- MPI parallelized solvers for dense matrices (EigenExa[2], ELPA[3], Elemental[4], ScaLAPACK)

- MPI parallelized solvers for sparse matrices (Anasazi in Trilinos[5], SLEPc[6]) to cover matrix representations below:

  - CRS (Compressed Row Storage)
  - Matrix-free method (the method to give matrix-vector product routines to solvers)

Rokko has the following features:

- Integrated interfaces for eigensolvers and matrices, independent of individual eigensolver libraries

- Rokko's interfaces are implemented by utilizing factory. It enables the user to dynamically select a solver.

- C, Fortran, and Python bindings of Rokko

- Automatically detecting libraries by using CMake in building Rokko

- Unit and integrated test programs by GoogleTest

- Install scripts of eigensolvers for various architectures

We prepare a paper to report design policy, software structure, and usage examples of Rokko.

# References

[1] T. Sakashita, R. Igarashi, Y. Motoyama, T. Okubo, and S. Todo. Repository of Rokko. `https://github.com/t-sakashita/rokko.git`, 2012.

[2] T. Imamura, T. Hirota, and T. Fukaya. EigenExa web page. `https://www.r-ccs.riken.jp/labs/lpnctrt/projects/eigenexa/`, 2021.

[3] ELPA Consortium. ELPA (Eigenvalue soLvers for Petaflop Applications web page). `http://elpa.rzg.mpg.de`, 2013.

[4] J. Poulson. Distributed-memory dense linear algebra Elemental web page. `https://github.com/elemental/Elemental`, 2013.

[5] M. A. Heroux, R. A. Bartlett, and V. E. Howle. Trilinos Project web page. `https://trilinos.github.io`, 2003.

[6] V. Hernandez, J. E. Roman, and V. Vidal. SLEPc web page. `http://slepc.upv.es`, 2002.

# Finite temperature calculations of quantum spin systems

Katsuhiro MORITA

*Department of Physics and Astronomy, Faculty of Science and Technology,*
*Tokyo University of Science, Noda, Chiba 278-8510*

We conducted calculations on the finite-temperature magnetization curves for the $J_1 - J_2$ kagome lattice, with a particular focus on the 1/3 magnetization plateau [1]. For $J_2 = \pm 0.3$, the 1/3 plateau begins to melt almost symmetrically as the temperature increases. However, at $J_2 = 0$, the magnetization deviates from 1/3 starting from the left side of the plateau, displaying asymmetric melting. This confirms that asymmetric melting occurs only around $J_2 = 0$. Instead of a plateau, a slope appears at $M/M_{sat} = 1/3$, which differs on either side, suggesting a difference in the density of states.

Therefure, we calculated low-energy excitation spectra for $N = 36$ at $J_2 = 0$ and $J_2 = -0.3$ to investigate the causes of the asymmetric melting of the 1/3 plateau at $J_2 = 0$ and the symmetric melting at $J_2 = -0.3$. At $J_2 = 0$, all excitation energies for $S_{tot}^z = 7$ are greater than 0.1, whereas for $S_{tot}^z = 5$, there are 76 states with $\Delta E \leq 0.06$ as shown in Fig. 1(a). This indicates the cause of asymmetric melting. In contrast, at $J_2 = -0.3$, similar energy spectra are observed for $S_{tot}^z = 5, 6$, and 7, with excitation energies above 0.2, excluding very low excited states as shown in Fig. 1(b). These spectra differ from those at $J_2 = 0$ and indicate the symmetric melting of the 1/3 plateau.
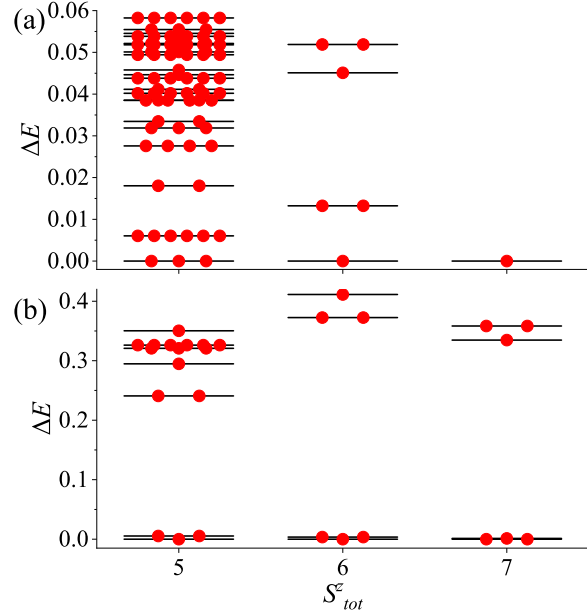


Figure 1: Low-energy excitation spectra of the $J_1 - J_2$ kagome lattice with $N = 36$ for the states with $S_{tot}^z = 5, 6$, and 7 at (a) $J_2 = 0$ and (b) $J_2 = -0.3$. The horizontal bars indicate the energy gap $\Delta E$. The number of filled red circles represents the degeneracy. [1]

# References

[1] K. Morita: Phys. Rev. B **108**, 184405 (2023).

# Multiple-Q orders in two-dimensional Hubbard Models

Takashi UCHIDA

*Hokkaido University of Science*

*4-1, 7-15, Maeda, Teine-ku, Sapporo 006-8585*

In the last decade, multiple-Q orders in magnetic systems have attracted attention because they sometimes reveal nontrivial magnetic structures such as magnetic skyrmions. Typically, these structures are realized in the Dzyaloshinskii-Moriya (DM) interaction driven systems under magnetic field. The nontrivial multiple-Q orders can also be realized in inversion-symmetric systems where the DM interaction is absent [1, 2].

The purpose of the present research is to investigate the nature of the multiple-Q orders in inversion-symmetric itinerant systems. We have explored the magnetic and electronic structures of the triangular-lattice single-band Hubbard model by means of the molecular spin dynamics (MSD) method [3]. The present formulation of the MSD adopts the static approximation to the functional integral method and the isothermal molecular dynamics technique, and reduces to the generalized Hartree-Fock approximation at the ground state.

In the present work, we have performed the MSD calculation with use of the global charge neutrality condition instead of using the local charge neutrality condition [3]. This has the advantage that the charge transfer among the atoms is allowed in the magnetic structure formation. In the numerical calculations the most time-consuming process is the magnetic force calculation at each time step, where the local electronic structures are calculated in real space by means of the recursion method. We have adopted the MPI parallel calculation

scheme and found it effective in saving both computing time and CPU resources.

We have performed magnetic structure calculations on a hexagonal supercell with 972 lattice points, which is embedded in a large cluster consisting of 6 such supercells, each of which are connected by the periodic boundary condition. Under zero magnetic field and the fixed value of the temperature $T/t = 0.0005$, we have explored the magnetic structures changing the Coulomb interaction strength $U/t$ and the electron number $n$ along the antiferromagnetic-ferromagnetic boundary. We have found that the 3Q magnetic orders are realized for $U/t < 4.0$ and $n = 1.45 \sim 1.53$ accompanying the 3Q charge density waves (CDW) with the same Q vectors as the magnetic ones. For $U/t = 4.0 \sim 4.3$ and $n \sim 1.4$, 2Q+2Q+2Q states were found to appear, which do not accompany CDWs. In both cases, the electronic density of states shows a dip at the Fermi energy, which suppress the formation of spontaneous magnetization and stabilize the multiple-Q orders.

# References

[1] T. Okubo, S. Chung, and H. Kawamura: Phys. Rev. Lett. **108** (2012) 017206

[2] Y. Kakehashi: J. Phys. Soc. Jpn. **89** (2020) 094710.

[3] Y. Kakehashi, S. Akbar, and N. Kimura: Phys. Rev. B**57** (1998) 8354.

# Molecular Dynamics Simulation of Graphene-nanosapcer Stacking Structure

Mingda Ding, Taiki Inoue, Yoshihiro Kobayashi

*Department of Applied Physics, Osaka University, Yamadaoka, Suita, Osaka 565-0871*

In this year, we studied the microstructure of graphene (Gr) and nanospacer stacking structure using molecular dynamics simulation [1].

By controlling the interlayer distance and altering interlayer interactions, it is possible to modulate the properties of multilayer Gr and induce novel physical phenomena. However, the energetically favorable AB stacking structure in multilayer Gr indicates a parabolic dispersion band structure with strong interlayer coupling. To address this issue, we introduce nanomaterials between Gr layers as nanospacers to manipulate the microstructure. The Gr stacking structures with carbon nanotube (CNT) and nanodiamond (ND) as spacers are fabricated experimentally. Raman spectroscopy confirms a decrease in interlayer interaction, while atomic force microscopy (AFM) reveals an expansion of the interlayer distance. The AFM observation finds two distinct morphologies, upper Gr suspension and interlayer adhesion, which are determined by the density of spacers. To systematically elucidate the regularities and mechanisms of nanospacer's influence on the interlayer distance of the stacking structure, MD simulation was conducted.

The MD simulation is conducted using the open-source software, LAMMPS (Large-scale Atomic/Molecular Massively Parallel Simulator). The number of atoms is 10,000~770,000, which depends on the size of the Gr layers. The AIREBO potential is used to describe the short-range interaction and the LJ interaction is used for long-range interaction between Gr layers. The dynamic relaxation is conducted to find the energy-stable structure using the velocity-Verlet method. The cases of Gr-ND with more atoms are mainly simulated in System B (Ohtaka) with 2~4 nodes and a computational time of 16~48 h. The systems of Gr-CNT are simulated in System C (Kugui) with 1 node and a computational time of 5~18 h.

We simulated stacked structures of double-layer Gr with both CNTs and NDs spacers (Fig. 1). By applying periodic boundary conditions around the structure edges, the systems with different sizes of Gr can simulate different areal densities of CNTs and NDs. Additionally, we constructed stacked structures with CNTs and NDs of varying diameters for simulation. As the size of Gr increased, i.e., a decrease in spacer areal density, there was a transition from

upper Gr suspension to interlayer adhesion. This transition is comparable with the two distinct morphologies observed experimentally. Furthermore, with an increase in nanospacer diameter, the critical areal density for the transition also increased.

The appearance of two different configurations is induced by the difference in potential energy. The configurations with minimum energy are obtained in MD simulations with the two dominant components of deformation energy and adhesion energy. The flat-suspended upper Gr results in lower deformation energy and increased adhesion energy. The significant deformation of adhered Gr increases the deformation energy, while the adhesion energy decreases to a minimum. When the inter-spacer distance is small, the sum of the energy components is lower with upper Gr suspension. The difference in adhesion energy between the two configurations increases with the size of the Gr i.e., inter-spacer distance. When the inter-spacer distance exceeds a critical value, the transition from suspension to interlayer adhesion appears.

Our study of the nanospacer insertion effect

contributes to the enhanced and novel properties of multilayer Gr to facilitate functional enhancement for wider applications.
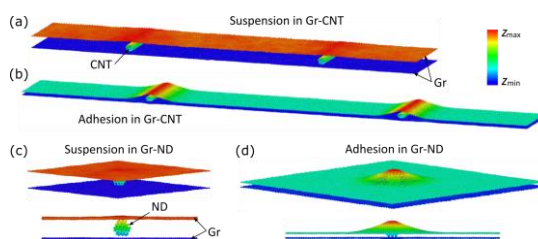


Figure 1: Deformed configuration obtained by MD simulation of graphene (Gr) and nanospacer stacking structure. (a) The Gr and carbon nanotube (CNT) stacking structure (Gr-CNT) with upper Gr suspension of larger interlayer distance. (b) The Gr-CNT with larger inter-CNT distance and interlayer adhesion. (c, d) The suspension and interlayer adhesion of Gr and nanodiamond (ND) stacking structure (Gr-ND).

## References

[1] M. Ding, T. Inoue, J. I. Enriquez, H. H. Handoko, Y. Ogawa, Y. Taniyasu, Y. Hamamoto, Y. Morikawa, Y. Kobayashi, J. Phys. Chem. C **127**, 23768‑23777 (2023).

# Classification of slow and fast earthquakes based on fluid pressure and porosity

Takehito SUZUKI

*Department of Physical Sciences, Aoyama Gakuin University*
*5-10-1, Fuchinobe, Chuo-ku, Sagamihara, Kanagawa 252-5258*

Two qualitatively different behaviors of earthquakes have been known. One is the fast earthquake, which we feel naturally. The other one is slow earthquakes, which generate negligible seismic waves. Although the slow earthquakes are not disastrous, they are considered to sometimes change to the fast earthquakes after several repetitions. Whether this transition occurs or not is a fatal problem to the human society, and we should clarify the condition for the transition to occur.

We employ the spring-block model and the interaction among the slip, heat, fluid pressure, and porosity. The former is widely known to generate the stick-slip behavior, which can be considered to model the earthquake cycle. The latter is also known to affect the dynamic earthquake slip behavior. First, note that the heat and pore-generation effects are related with the fluid-pressure change on the slip surface. If the heat effect is dominant, the fluid pressure increases, whereas if the pore-generation effect is dominant, the fluid pressure decreases. Moreover, if the fluid pressure on the slip surface increases, the slip is enhanced, whereas if it decreases, the slip is inhibited.

For this model, it should be emphasized that we have found that the function

$$F(u_f) = \frac{1}{2}k_p u_f^2 + \mu_{\text{stat}}(\sigma_n^0 + p_0)u_f$$

$$-\mu_{\text{slid}}\left[\frac{1}{\gamma}\left(\sigma_n^0 + p_0 - \frac{M_0'\alpha_0}{\frac{\alpha_0}{\phi_\infty} - \gamma}\right)(1 - e^{-\gamma u_f})\right.$$

$$\left. + \frac{M_0'\phi_\infty}{\frac{\alpha_0}{\phi_\infty} - \gamma}(1 - e^{-\alpha_0 u_f/\phi_\infty})\right] \quad (1)$$

governs whether the slow and fast earthquakes occur (the variables are summarized in [1]). If the equation $F(u_f) = 0$ has three positive solutions, the slow earthquakes emerge, whereas if the equation has a single positive solution, the fast earthquakes emerge [1].

We obtain the phase diagram of the small and large slippages, i.e., the phase diagram of the foreshocks and mainshock, in the $p_0 - \phi_0$ plane, as follows, where $p_0$ and $\phi_0$ describe the value of the fluid pressure and porosity at the onset of each slippage, respectively. By definition, $dF(u_f)/du_f|_{u_f=u_2} = 0$ must be satisfied, where $F(u_2)$ is the local maximum. From Eq. (1), equation $dF(u_f)/du_f = 0$ yields

$$e^{-\gamma' u_2} = \frac{k_p u_2}{\mu_{\text{slid}}AS} + \frac{\mu_{\text{stat}}(\sigma_n^0 + p_0)}{\mu_{\text{slid}}A}$$

$$-\frac{\sigma_n^0 + p_0 - A}{A}e^{-\gamma u_2}. \quad (2)$$

Therefore, using Eqs. (1) and (2), we obtain

$$\frac{1}{2}k_p u_2^2 + \left(\mu_{\text{stat}}(\sigma_n^0 + p_0)S + \frac{k_p}{\gamma'}\right)u_2$$

$$-\frac{\mu_{\text{slid}}}{\gamma}(\sigma_n^0 + p_0 - A)S - \frac{\mu_{\text{slid}}}{\gamma'}AS$$

$$+\frac{\mu_{\text{stat}}}{\gamma'}(\sigma_n^0 + p_0)S$$

$$+\mu_{\text{slid}}(\sigma_n^0 + p_0 - A)S\left(\frac{1}{\gamma} - \frac{1}{\gamma'}\right)e^{-\gamma u_2} = 0. \quad (3)$$

When the magnitude of $\gamma u_2$ is greater than the order of unity, we can neglect the $\exp(-\gamma u_2)$ term. Thus, we have a quadratic

equation, which gives the relation among $u_2$, $p_0$, and $\phi_0$. By substituting the solution of this quadratic equation into Eq. (1), we obtain $p_0$ and $\phi_0$, which are critical for inducing the phase transition, yielding

$$
\begin{aligned}
F(u_2) & = -\frac{k_p}{\gamma'}u_2 - \frac{\mu_{\text{stat}}}{\gamma'}(\sigma_n^0 + p_0)S \\
& \quad + \frac{\mu_{\text{slid}}}{\gamma'}e^{-\gamma' u_2}AS \\
& \equiv G(p_0, \phi_0) = 0.
\end{aligned} \tag{4}
$$

The phase diagram thus obtained is shown in Figure 1, exhibiting the numerical results obtained using several sets of $(p_0, \phi_0)$ for $\phi_\infty = 0.1$. The green line shows the phase boundary, $G(p_0, \phi_0) = 0$, and the red and blue symbols show that $(p_0, \phi_0)$ cause fast and slow earthquakes, respectively. The analytical results coincide well with the numerical ones for $\phi_\infty = 0.1$, and we can conclude that the approximation above is valid for this case. For the calculations, ISSP Supercomputer was useful.
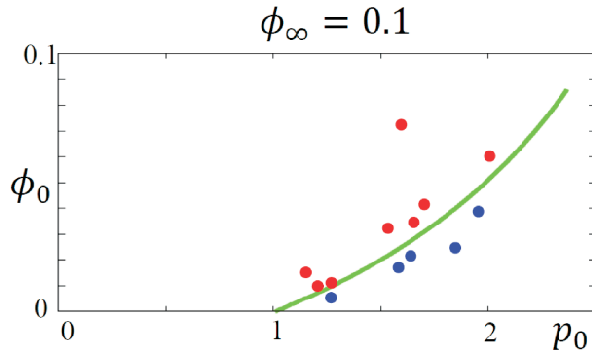


Figure 1: Boundary between the slow and fast earthquakes, denoted by the green line in the $p_0 - \phi_0$ plane obtained from Eq. (4). The value of $\phi_\infty$ is 0.1. The red and blue symbols show that $(p_0, \phi_0)$ cause fast and slow earthquakes, respectively.

## References

[1] T. Suzuki, and H. Matsukawa, submitted to Rhys. Rev. E.